

# Image Analysis for Cosmology: Results from the GREAT10 Galaxy Challenge

T. D. Kitching<sup>1,\*</sup>, S. T. Balan<sup>2</sup>, S. Bridle<sup>3</sup>, N. Cantale<sup>4</sup>, F. Courbin<sup>4</sup>, M. Gentile<sup>4</sup>,  
M. S. S. Gill<sup>5,6,7</sup>, S. Harmeling<sup>8</sup>, C. Heymans<sup>1</sup>, M. Hirsch<sup>3,8</sup>, T. Kacprzak<sup>3</sup>,  
D. Kirkby<sup>9</sup>, D. Margala<sup>9</sup>, R. J. Massey<sup>10</sup>, P. Melchior<sup>7</sup>, G. Nurbaeva<sup>4</sup>,  
K. Patton<sup>7</sup>, J. Rhodes<sup>11,12</sup>, B. T. P. Rowe<sup>3,11,12</sup>, A. N. Taylor<sup>1</sup>, M. Tewes<sup>4</sup>,  
M. Viola<sup>1</sup>, D. Witherick<sup>3</sup>, L. Voigt<sup>3</sup>, J. Young<sup>7</sup>, J. Zuntz<sup>3,13,14</sup>

<sup>1</sup>*SUPA, Institute for Astronomy, University of Edinburgh, Royal Observatory, Blackford Hill, Edinburgh, EH9 3HJ, U.K.*

<sup>2</sup>*Astrophysics Group, Cavendish Laboratory, JJ Thomson Avenue, Cambridge, CB3 0HE, U.K.*

<sup>3</sup>*Department of Physics and Astronomy, University College London, Gower Street, London, WC1E 6BT, U.K.*

<sup>4</sup>*Laboratoire d'Astrophysique, Ecole Polytechnique Fédérale de Lausanne (EPFL), Switzerland*

<sup>5</sup>*Kavli Institute for Particle Astrophysics & Cosmology, Stanford, USA*

<sup>6</sup>*Centro Brasileiro de Pesquisas Físicas, Rio de Janeiro, RJ, Brazil*

<sup>7</sup>*Center for Cosmology and AstroParticle Physics Physics Dept, The Ohio State University, USA*

<sup>8</sup>*Department of Empirical Inference, Max Planck Institute for Intelligent Systems, Tübingen, Germany*

<sup>9</sup>*Department of Physics and Astronomy, UC Irvine, 4129 Frederick Reines Hall, Irvine, CA 92697-4575, USA*

<sup>10</sup>*Institute for Computational Cosmology, Durham University, South Road, Durham, DH1 3LE, U.K.*

<sup>11</sup>*Jet Propulsion Laboratory, California Institute of Technology, 4800 Oak Grove Drive, Pasadena, CA 91109, USA*

<sup>12</sup>*California Institute of Technology, 1200 East California Boulevard, Pasadena, CA 91106, USA*

<sup>13</sup>*Astrophysics Group, University of Oxford, Denys Wilkinson Building, Keble Road, Oxford OX1 3RH, U.K.*

<sup>14</sup>*Oxford Martin School, University of Oxford, Old Indian Institute, 34 Broad Street, Oxford OX1 3BD, U.K.*

24 February 2012

## ABSTRACT

In this paper we present results from the weak lensing shape measurement GRavitational lEnsing Accuracy Testing 2010 (GREAT10) Galaxy Challenge. This marks an order of magnitude step change in the level of scrutiny employed in weak lensing shape measurement analysis. We provide descriptions of each method tested and include 10 evaluation metrics over 24 simulation branches.

GREAT10 was the first shape measurement challenge to include variable fields; both the shear field and the Point Spread Function (PSF) vary across the images in a realistic manner. The variable fields enable a variety of metrics that are inaccessible to constant shear simulations including a direct measure of the impact of shape measurement inaccuracies, and the impact of PSF size and ellipticity, on the shear power spectrum. To assess the impact of shape measurement bias for cosmic shear we present a general pseudo-Cl formalism, that propagates spatially varying systematics in cosmic shear through to power spectrum estimates. We also show how one-point estimators of bias can be extracted from variable shear simulations.

The GREAT10 Galaxy Challenge received 95 submissions and saw a factor of 3 improvement in the accuracy achieved by shape measurement methods. The best methods achieve sub-percent average biases. We find a strong dependence on accuracy as a function of signal-to-noise, and indications of a weak dependence on galaxy type and size. Some requirements for the most ambitious cosmic shear experiments are met above a signal-to-noise ratio of 20. These results have the caveat that the simulated PSF was a ground-based PSF. Our results are a snapshot of the accuracy of current shape measurement methods and are a benchmark upon which improvement can continue. This provides a foundation for a better understanding of the strengths and limitations of shape measurement methods.

**Key words:** Cosmology: observations, gravitational lensing: weak, methods: statistical, techniques: image processing

\*tdk@roe.ac.uk

## 1 INTRODUCTION

In this paper we present the results from the GRavitational lEnsing Accuracy Testing 2010 (GREAT10) Galaxy Challenge. GREAT10 was an image analysis challenge for cosmology that focused on the task of measuring the weak lensing signal from galaxies. Weak lensing is the effect whereby the image of a source galaxy is distorted by intervening massive structure along the line-of-sight. In the weak field limit this distortion is a change in the observed ellipticity of the object, and this change in ellipticity is called shear. Weak lensing is particularly important for understanding the nature of dark energy and dark matter, because it can be used to measure the cosmic growth of structure and the expansion history of the Universe (see reviews by e.g. Albrecht et al., 2001; Massey, Kitching, Richards, 2010; Hoekstra & Jain, 2008; Bartelmann & Schneider, 2001; Weinberg et al., 2012). In general, by measuring the ellipticities of distant galaxies – hereafter denoted “shape measurement” – we can make statistical statements about the nature of the intervening matter. The full process through which photons propagate from galaxies to detectors is described in a previous companion paper, the GREAT10 Handbook (Kitching et al., 2011).

There are a number of features, in the physical processes and optical systems, through which the photons we ultimately use for weak lensing pass. These features must be accounted for when designing shape measurement algorithms. These are primarily the convolution effects of the atmosphere and the telescope optics, pixelisation effects of the detectors used and the presence of noise in the images. The simulations in GREAT10 aimed to address each of these complicating factors. GREAT10 consisted of two concurrent challenges as described in Kitching et al. (2011): the Galaxy Challenge, where entrants were provided with 50 million simulated galaxies and asked to measure their shapes and spatial variation of the shear field with a known Point Spread Function (PSF) and the Star Challenge wherein entrants were provided with an unknown PSF, sampled by stars, and asked to reconstruct the spatial variation of the PSF across the field.

In this paper we present the results of the GREAT10 Galaxy Challenge. The challenge provided a controlled simulation development environment in which shape measurement methods could be tested, and was run as a blind competition for 9 months from December 2010 to September 2011. Blind analysis of shape measurement algorithms began with the Shear TESting Programme (STEP; Heymans et al., 2006; Massey et al., 2007) and GREAT08 (Bridle et al., 2009, 2010). The blindness of these competitions is critical in testing methods under circumstances that will be similar to those encountered in real astronomical data. This is because for weak lensing, unlike photometric redshifts for example, we cannot observe a training set from which we know the shear distribution (we can however observe a subset of galaxies at high signal-to-noise to train upon, which is something we address in this paper).

The GREAT10 Galaxy Challenge is the first shape measurement analysis that includes *variable fields*. Both the shear field and the PSF vary across the

images in a realistic manner. This enables a variety of metrics that are inaccessible to constant shear simulations (where the fields are a single constant value across the images), including a direct measure of the impact of shape measurement inaccuracies on the inferred shear power spectrum and a measure of the correlations between shape measurement inaccuracies and the size and ellipticity of the PSF.

We present a general pseudo-Cl formalism for a flat-sky shear field in Appendix A, which we use to show how to propagate general spatially varying shear measurement biases through to the shear power spectrum. This has a more general application in cosmic shear studies.

This paper summarises the results of the GREAT10 Galaxy Challenge. We refer the reader to a companion paper that discusses the GREAT10 Star challenge (Kitching et al., in prep). Here we summarise the results that we show, distilled from the wealth of information that we present in this paper:

- (i) Signal-to-noise: We find a strong dependence of the metrics below  $S/N = 10$ . However we find methods that meet requirements for the most ambitious experiments when  $S/N > 20$ . We note that methods tested here have been optimised for use on ground based data in this regime.
- (ii) Galaxy type: We find marginal evidence that model fitting methods have a relatively low dependence on galaxy type compared to model-independent methods.
- (iii) PSF dependence: We find contributions to biases from PSF size, but less so from PSF ellipticity.
- (iv) Galaxy Size: For large galaxies well sampled by the PSF, with scale radii  $\gtrsim 2$  times the mean PSF size we find that methods meet requirements on bias parameters for the most ambitious experiments. However if galaxies are unresolved, with radii  $\lesssim 1$  times the mean PSF size, biases become significant.
- (v) Training: We find that calibration on a high signal-to-noise sample can significantly improve a method’s average biases.
- (vi) Averaging Methods: We find that averaging ellipticities over several methods is clearly beneficial, but that the weight assigned to each method will need to be correctly determined.

In Section 2 we describe the Galaxy Challenge structure, in Section 3 we describe the simulations. Results are summarised in Section 4 and we present conclusions in Sections 5 and 6. We make extensive use of Appendices that contain technical information on the metrics and a more detailed breakdown of individual shape measurement method’s performance.

## 2 DESCRIPTION OF THE COMPETITION

The GREAT10 Galaxy Challenge was run as an open competition for 9 months between 3<sup>rd</sup> December 2010 and 2<sup>nd</sup> September 2011<sup>1</sup>. The challenge was open for

<sup>1</sup> Between 2<sup>nd</sup> September 2011 and 8<sup>th</sup> September 2011 we extended the challenge to allow submissions from those

participation from anyone, the website<sup>2</sup> served as the portal for participants, and data could be freely downloaded.

The challenge was to reconstruct the shear power spectrum from subsampled images of sheared galaxies (Kitching et al. 2011). All shape measurement methods to date do this by measuring the ellipticity from each galaxy in an image, although scope for alternative approaches was allowed. Participants in the challenge were asked to submit either

- (i) *Ellipticity catalogues* that contained an estimate of the ellipticity for each object in each image, or
- (ii) *Shear power spectra*, that consisted of an estimate of the shear power spectrum for each simulation set.

Participants were required to access 1 TB of imaging data in the form of FITS images. Each image contained 10,000 galaxies arranged on a 100x100 grid. Each galaxy was captured in a single postage stamp of 48x48 pixels (to incorporate the largest galaxies in the simulation with no truncation), and the grid was arranged so that each neighbouring postage stamp was positioned contiguously i.e. there were no gaps between postage stamps and no overlaps. Therefore each image was 4800x4800 pixels in size. The simulations were divided into 24 sets (see Section 3.1) and each set contained 200 images. For each galaxy in each image participants were provided with a functional description of the PSF (described in Section 6) and an image showing a pixelised realisation of the PSF. In addition a suite of development code was provided to help read in the data and perform a simple analysis<sup>3</sup>.

## 2.1 Summary of metrics

The metric with which the live leaderboard was scored during the challenge was a Quality factor  $Q$ , defined as

$$Q \equiv 1000 \frac{5 \times 10^{-6}}{\int d\ln \ell |\tilde{C}_\ell^{EE} - C_\ell^{EE, \gamma\gamma}| \ell^2}, \quad (1)$$

averaged over all sets, a quantity that relates the reconstructed shear power spectrum  $\tilde{C}_\ell^{EE}$  with the true shear power spectrum  $C_\ell^{EE, \gamma\gamma}$ . We describe this metric in more detail in Appendices A and B. By evaluating this metric for each submission, results were posted to a live leaderboard that ranked methods based on the value of  $Q$ . We will also investigate a variety of alternative metrics extending the STEP  $m$  and  $c$  bias formalism to variable fields.

The measured ellipticity of an object at position  $\theta$  can be related to the true ellipticity and shear,

$$\begin{aligned} e_{\text{measure}}(\theta) &= \gamma(\theta) + e_{\text{intrinsic}}(\theta) \\ &+ c(\theta) + m(\theta)[\gamma(\theta) + e_{\text{intrinsic}}(\theta)] + \\ &+ q(\theta)[\gamma(\theta) + e_{\text{intrinsic}}(\theta)][\gamma(\theta) + e_{\text{intrinsic}}(\theta)] \\ &+ e_n(\theta), \end{aligned} \quad (2)$$

with a multiplicative bias  $m(\theta)$ , an offset  $c(\theta)$ , and a quadratic term  $q(\theta)$  (this is  $\gamma|\gamma|$ , not  $\gamma^2$ , since we may expect divergent behaviour to more positive and more negative shear values for each domain respectively), that in general are functions of position due to PSF and galaxy properties.  $e_n(\theta)$  is a potential stochastic noise contribution. For spatially variable shear fields, biases between measured and true shear can vary as a function of position, mixing angular modes and power between E and B-modes. In Appendix A, we present a general formalism that allows for the propagation of biases into shear power spectra using a pseudo-CL methodology; this approach has applications beyond the treatment of shear systematics. The full set of metrics are described in detail in Appendix B and are summarised in Table 1.

The metric with which the live leaderboard was scored was the  $Q$  value, and the same metric was used for ellipticity catalogue submissions and power spectrum submissions. However in this paper we will introduce and focus on  $Q_{\text{dn}}$  (see Table 1) that for ellipticity catalogue submissions removes any residual pixel-noise error (nominally associated with biases caused by finite signal-to-noise or inherent shape measurement method noise). For details see Appendix B. Note that this is not a correction for ellipticity (shape) noise which is removed in GREAT10 through the implementation of a B-mode only intrinsic ellipticity field.

The metric  $Q$  takes into account scatter between the estimated shear and the true shear due to stochasticity in a method or spatially varying quantities, such that a small  $m(\theta)$  and  $c(\theta)$  do not necessarily correspond to a large  $Q$  value (see Appendix B). This is discussed within the context of previous challenges in Kitching et al. (2008). Spatial variation is important because the shear and PSF fields vary, so that there may be scale-dependent correlations between them, and stochasticity is important because we wish methods to be accurate (such that errors do not dilute cosmological or astrophysical constraints) as well as being unbiased.

For variable fields we can complement the linear biases,  $m(\theta)$  and  $c(\theta)$ , with a component that can be correlated with any spatially varying quantity  $X(\theta)$ , for example PSF ellipticity or size;

$$m(\theta) = m_0 + \alpha X(\theta), \quad c(\theta) = c_0 + \beta X(\theta), \quad (3)$$

with spatially constant terms  $m_0$  and  $c_0$  and correlation coefficients  $\alpha$  and  $\beta$ . Only ellipticity catalogue submissions can have  $m_0$ ,  $c_0$ ,  $\alpha$  and  $\beta$  values calculated because these parameters require individual galaxy ellipticity estimates (in order to calculate the required mixing matrices, see Appendices A and B). Throughout we will refer to  $m$  and  $c$  as the one-point estimators of bias and make the distinction between spatially constant terms  $m_0$  and  $c_0$  and correlations  $\alpha$  and  $\beta$  only where clearly stated. Finally we also include a non-linear shear response (see Table 1), we do not include a discussion of this in the main results, because  $q\gamma|\gamma| \approx 0$  for most methods, but show the results in Appendix E.

To measure biases at the power spectrum level we define constant linear bias parameters (see Appendix A equation 23)

$$\tilde{C}_\ell^{EE} = C_\ell^{EE, \gamma\gamma} + \bar{\mathcal{A}} + \bar{\mathcal{M}} C_\ell^{EE, \gamma\gamma}, \quad (4)$$

participants who had not met the deadline; those submissions will be labelled in Section 4.

<sup>2</sup> <http://www.greatchallenges.info>

<sup>3</sup> <http://great.roe.ac.uk/data/code/>

Metric	Definition	Features
$m, c, q$	$\hat{\gamma} = (1 + m)\gamma^t + c + q\gamma^t \gamma^t $	One-point estimators of bias. Links to STEP
$Q$	$1000 \frac{5 \times 10^{-6}}{\int d\ln \ell  \tilde{C}_\ell^{EE} - C_\ell^{EE, \gamma\gamma}  \ell^2}$	Numerator relates to bias on $w_0$
$Q_{\text{dn}}$	$1000 \frac{5 \times 10^{-6}}{\int d\ln \ell  C_\ell^{EE} - C_\ell^{EE, \gamma\gamma} - \frac{\langle \sigma_n^2 \rangle}{N_{\text{realisation}} N_{\text{object}}}  \ell^2}$	Corrects Q for pixel noise
$\mathcal{M} \simeq m^2 + 2m, \mathcal{A} \propto \sigma(c)^2$	$\tilde{C}_\ell^{EE} = C_\ell^{EE, \gamma\gamma} + \tilde{\mathcal{A}} + \tilde{\mathcal{M}} C_\ell^{EE, \gamma\gamma}$	Power spectrum relations.
$\alpha_X$	$m(\boldsymbol{\theta}) = m_0 + \alpha X(\boldsymbol{\theta})$	Variation of $m$ with PSF ellipticity/size
$\beta_X$	$c(\boldsymbol{\theta}) = c_0 + \beta X(\boldsymbol{\theta})$	Variation $c$ with PSF ellipticity/size

**Table 1.** A summary of the metrics used to evaluate shape measurement methods for GREAT10. These are defined in detail in Appendices A and B. We refer to  $m$  and  $c$  as the one-point estimators of bias, and make the distinction between these and spatially constant terms ( $m_0, c_0$ ) and correlations ( $\alpha, \beta$ ) only where clearly stated.

that relate the measured power spectrum to the true power spectrum. These are approximately related to one-point shear bias  $m$ , and the variance of  $c$ , by  $\mathcal{M}/2 \simeq m$  for values of  $m \ll 1$  and  $\sqrt{\mathcal{A}} \simeq \sigma(c)(2\pi/\ell_{\text{max}})^{1/2}$ . These parameters can be calculated for both ellipticity and power spectrum submissions.

### 3 DESCRIPTION OF THE SIMULATIONS

In this Section we describe the overall structure of the simulations. For details on the local modelling of the galaxy and star profiles and the spatial variation of the PSF and shear fields we refer to Appendix C.

#### 3.1 Simulation structure

The structure of the simulations was engineered such that, in the final analysis, the various aspects of performance for a given shape measurement method could be gauged. The competition was split into sets of images, where one set was a ‘fiducial’ set and the remaining sets represented perturbations about the parameters in that set. Each set consisted of 200 images. This number was justified by calculating the expected pixel-noise effect on shape measurement methods (see Appendix B) such that when averaging over all 200 images this effect should be suppressed (however, see also Section 4 where we investigate this noise term further).

Participants were provided with a functional description and a pixelated realisation of the PSF at each galaxy position. The task of estimating the PSF itself was set a separate ‘Star Challenge’ that is described in a companion paper (Kitching et al. in prep).

The variable shear field was constant in each of the images within a set, but the PSF field and intrinsic ellipticity could vary such that there were three kinds of set

- **Type 1**, ‘Single Epoch’, fixed  $C_\ell^{EE}$ , variable PSF, variable intrinsic ellipticity.
- **Type 2**, ‘Multi-Epoch’, Fixed  $C_\ell^{EE}$ , variable PSF, fixed intrinsic ellipticity.
- **Type 3**, ‘Stable Single Epoch’, Fixed  $C_\ell^{EE}$ , fixed PSF, variable intrinsic ellipticity.

The default, fiducial, type being one in which both PSF and intrinsic ellipticity vary between images in a set. This was designed in part to test the ability of any method which took advantage of stacking procedures, where galaxy images are averaged over some population, by testing whether stacking worked when either the galaxy or PSF were fixed across images within a set or not. Stacking methods achieved high scores in GREAT08, Bridle et al. (2010), but in actuality were not submitted for GREAT10. For each type of set the PSF and intrinsic ellipticity fields are *always spatially varying* but this variation did not change *within a set*; when we refer to a quantity being ‘fixed’ this means that its spatial variation does not vary between images within a set.

Type 1 (variable PSF and intrinsic field) sets test the ability of a method to reconstruct the shear field in the presence of both a variable PSF field and variable intrinsic ellipticity between images. This nominally represents a sequence of observations of different patches of sky but with the same underlying shear power spectrum. Type 2 sets (variable PSF and fixed intrinsic field) represent an observing strategy where the PSF is different in each exposure of the same patch of sky (a typical ground based observation); so called ‘multi-epoch’ data. Type 3 sets (fixed PSF) represent ‘single-epoch’ observations with a highly stable PSF. These were only simple approximations to reality because, for example, properties in the individual exposures for the ‘multi-epoch’ sets were not correlated (as they may be in real data), and the signal-to-noise was constant in all images for the single and multi-epoch sets. Participants were aware of the PSF variation from image to image within a set but not of the intrinsic galaxy properties or shear. Thus the conclusions drawn from these tests will be conservative with regard to the testing between the different set types, relative to real data; where in fact this kind of observation is known to the observer *ab initio*. In subsequent challenges this hidden layer of complexity could be removed.

In Appendix D we list in detail the parameter values that define each set, and the parameters themselves are described in the sections below. In Table 2 we summarise each set by listing its distinguishing feature and parameter value. There were two additional

Set Number	Set Name	Fixed PSF/Intrinsic Field	Distinguishing Parameter
1	Fiducial	–	–
2	Fiducial	PSF	–
3	Fiducial	Int	–
4	Low S/N	–	S/N= 10
5	Low S/N	PSF	S/N= 10
6	Low S/N	Int	S/N= 10
7	High S/N <b>Training Data</b>	–	S/N= 40
8	High S/N	PSF	S/N= 40
9	High S/N	Int	S/N= 40
10	Smooth S/N	–	S/N distribution Rayleigh
11	Smooth S/N	PSF	S/N distribution Rayleigh
12	Smooth S/N	Int	S/N distribution Rayleigh
13	Small Galaxy	–	$r_b = 1.8$ $r_d = 2.6$
14	Small Galaxy	PSF	$r_b = 1.8$ $r_d = 2.6$
15	Large Galaxy	–	$r_b = 3.4$ $r_d = 10.0$
16	Large Galaxy	PSF	$r_b = 3.4$ $r_d = 10.0$
17	Smooth Galaxy	–	Size distribution Rayleigh
18	Smooth Galaxy	PSF	Size distribution Rayleigh
19	Kolmogorov	–	Kolmogorov PSF
20	Kolmogorov	PSF	Kolmogorov PSF
21	Uniform b/d	–	b/d fraction [0.3, 0.95]
22	Uniform b/d	PSF	b/d fraction [0.3, 0.95]
23	Offset b/d	–	b-d offset variance 0.5
24	Offset b/d	PSF	b-d offset variance 0.5

**Table 2.** A summary of the simulations sets with the parameter or function that distinguishes each set from the fiducial one. In the third column we list whether either the PSF or intrinsic ellipticity field (Int) were kept fixed between images within a set.  $r_b$  and  $r_d$  are the scale radii of the bulge and disk components of the galaxy models in pixels,  $b/d$  is the ratio between the integrated flux in the bulge to disk components of the galaxy models. See Appendix C and D for more details.

sets that used a pseudo-Airy PSF which we do not include in this paper because of technical reasons (see Appendix F).

Training data was provided in the form of a set with exactly the same size and form as the other sets. In fact the training set was a copy of Set 7, a set which contained high signal-to-noise galaxies. In this way the structure was set up to enable an assessment of whether training on high signal to noise data is useful when extrapolating to other domains, in particular low galaxy signal-to-noise regime. This is similar to being able to observe a region of sky with deeper exposures than a main survey.

### 3.2 Variable shear and intrinsic ellipticity fields

In the GREAT10 simulations the key and unique aspect was that the shear field was a variable quantity and not a static scalar value (as for all previous shape measurement simulations; STEP1, STEP2, GREAT08). To make a variable shear field we generated a spin-2 Gaussian random field from a  $\Lambda$ CDM weak lensing power spectrum (Hu, 1999)

$$C_\ell^{\gamma\gamma} = \int_0^{r_H} dr W_{ii}^{\text{GG}}(r) P_{\delta\delta}\left(\frac{\ell}{r}; r\right), \quad (5)$$

where  $P_{\delta\delta}$  is the matter power spectrum, and the lensing weight can be expressed as

$$W_{ii}^{\text{GG}}(r) = \frac{q_i(r)q_i(r)}{r^2}, \quad (6)$$

where the kernel is

$$q_i(r) = \frac{3H_0^2\Omega_m r}{2a(r)} \int_r^{r_H} dr' p_i(r') \frac{(r' - r)}{r'}. \quad (7)$$

We have assumed a flat Euclidean geometry throughout and  $r_H$  is the horizon size.  $p_i(r)$  refers to the redshift distribution of the lensed sources in redshift bin  $i$ ; this expression can be generalised to an arbitrary number (even a continuous set) of redshift bins (see Kitching, Heavens & Miller, 2011). For these simulations we have a single redshift bin with a median redshift of  $z_m = 1.0$  and a delta-function probability distribution  $p_i(r') = \delta^D(r - r_i)$ . We assume an Eisenstein & Hu (1999) linear matter power spectrum with a Smith et al. (2003) non-linear correction. The cosmological parameter values used were  $\Omega_m = 0.25$ ,  $h = H_0/100 = 0.75$ ,  $n_s = 0.95$  and  $\sigma_8 = 0.78$ . In order to add a random component to the shear power spectrum, so that participants could not guess the functional form, we added a series of Legendre polynomials  $P_n(x)$  up to 5<sup>th</sup> order, such that

$$C_\ell^{EE,\gamma\gamma} \rightarrow C_\ell^{EE,\gamma\gamma} + 2 \times 10^{-9} \sum_{n=1}^5 c_n P_n(x_L) \quad (8)$$

where the variable  $x_L = -1 + 2(\ell - 1)/(\ell_{\text{max}} - 1)$  is contained within the range  $[-1, 1]$  as  $\ell$  varies from  $\ell_{\text{min}}$  to  $\ell_{\text{max}}$ . The shear field generated has an E-mode power spectrum only. The size of the shear field was  $\theta_{\text{image}} = 2\pi/\ell_{\text{min}}$  and to generate the shear field we set  $\theta_{\text{image}} = 10$  degrees, such that the range in  $\ell$  we used to generate the power was  $\ell = [36, 3600]$  from the fundamental mode to the grid separation cut-off.

The shear field is generated on a grid of 100x100, which is then converted into an image of galaxy ob-

jects via an image generation code<sup>4</sup> with galaxy properties described in Appendix C. When postage stamps of objects are generated they point-sample the shear field at each position, and a postage stamp is generated. The postage stamps are then combined to form an image.

Throughout, the intrinsic ellipticity field had a variation that contained B-mode power only, as described in the GREAT10 Handbook. This meant that the contribution from intrinsic ellipticity correlations, as well from intrinsic shape noise, to the lensing shear power spectra was zero.

## 4 RESULTS

In total the challenge received 95 submissions from 9 separate teams and 12 different methods in total, these were

- 82 submissions before the deadline,
- 13 submissions in the post challenge period,

split into

- 85 ellipticity catalogue submissions,
- 10 power spectra submissions.

We summarise the methods that analysed the GREAT10 Galaxy Challenge in detail in Appendix E. The method that won the challenge, with the highest  $Q$  value at the end of the challenge period, was ‘fit2unfold’ submitted by the *DeepZot* team, authors D. Kirkby and D. Margala.

During the challenge a number of aspects of the simulations were corrected (we list these in Appendix F). Several methods generated low scores due to misunderstanding of simulation details, and in this paper we summarise only those results for which these errata did not occur. In the following we choose the best performing entry for each of the 12 shape measurement method entries.

### 4.1 One-point estimators of bias: $m$ and $c$ values

In Appendix B we describe how the estimators for shear biases on a galaxy-by-galaxy basis in the simulations – what we refer to as ‘one-point estimators’ of biases – can be derived, and how these relate to the STEP  $m$  and  $c$  parameters (Heymans et al. 2006). In Figure 1 and in Table 3 we show the  $m$  and  $c$  biases for the best performing entries for each method (those with the highest quality factors). In Appendix E we show how the  $m$  and  $c$  parameters, and the difference of the measured and true shear  $\hat{\gamma} - \gamma^t$ , vary for each method as a function of several quantities: PSF ellipticity, PSF size, galaxy size, galaxy bulge to

disk fraction and galaxy bulge to disk angle offset. We show in Appendix E that some methods have a strong  $m$  dependence on PSF ellipticity and size (e.g. TVNN and method04). Model fitting methods (gfit, im3shape) tend to have fewer model-dependent biases, whereas the KSB-like methods (DEIMOS, KSB f90) have the smallest average biases.

### 4.2 Variable shear

In the lefthand panel of Figure 2 we show the values of the linear power spectrum parameters  $\mathcal{M}$  and  $\mathcal{A}$  for each method for each set, and display by color code the Quality factor  $Q_{\text{dn}}$ . In Table 3 we show the mean values of these parameters averaged over all sets. We find a clear anti-correlation between  $\mathcal{M}$  and  $\mathcal{A}$  and  $Q_{\text{dn}}$ , with higher Quality factors corresponding to smaller  $\mathcal{M}$  and  $\mathcal{A}$  values. We will explore this further in the subsequent sections. We refer the reader to Appendix B where we show how the  $\mathcal{M}$ ,  $\mathcal{A}$  and  $Q_{\text{dn}}$  parameters are expected to be related in an ideal case. In the righthand panel of Figure 2 we also show the  $\mathcal{M}$ ,  $\mathcal{A}$  and  $Q_{\text{dn}}$  values for each method averaged over all sets.

In the lefthand panel of Figure 3 we show the effect that the pixel noise denoising step has on the Quality factor,  $Q$ . Note that the way that the denoising step is implemented here uses the variance of the true shear values (but not the true shear values themselves). This is a method that was not available to power spectrum submissions and indeed part of the challenge was to find optimal ways to account for this in power spectrum submissions. The final layer used to generate the ‘fit2-unfold’ submission performed power-spectrum estimation and used the model-fit errors themselves to determine and subtract the variance due to shape measurement errors, including pixel noise. We find as expected that  $Q$  in general increases for all methods when pixel noise is removed, by a factor of  $\lesssim 1.5$ , such that a method that has  $Q \simeq 100$  has a  $Q_{\text{dn}} \simeq 150$ . When this correction is applied the method ‘fit2-unfold’ still obtains the highest Quality factor, and the ranking of the top five methods is unaffected.

#### 4.2.1 Training

Several of the methods used the training data to help debug and test code. For example, and in particular, ‘fit2-unfold’ used the data to help build the galaxy models used and to set initial parameter values and ranges in the maximum likelihood fits. This meant that ‘fit2-unfold’ performed particularly well in sets similar to the training data (sets 7, 8, and 9) at high signal-to-noise; for details see Appendix D Figure 23, where ‘fit2-unfold’ has smaller combined  $\mathcal{M}$  and  $\mathcal{A}$  values than any other method for some sets.

To investigate whether using high signal-to-noise training data is useful for methods we investigate a scenario that training on the power spectra had been used for all methods. This modification was potentially available to all participants if they chose to implement it. To do this we measure the  $\mathcal{M}$  and  $\mathcal{A}$  values from the high signal-to-noise Set 7 (see Table 2) and apply the transformation to the power spectra, which is to first order equivalent to an  $m$  and  $c$  correction,

<sup>4</sup> To generate the image simulations we used a Monte Carlo code that simulates the galaxy model and PSF stages at a photon level; this code is a modified version of that used for the GREAT08 simulations (Bridle et al., 2010). The modified code is available here [http://great.roe.ac.uk/data/code/image\\_code](http://great.roe.ac.uk/data/code/image_code), the original code is by Konrad Kuijken, modified by SB and SBr for GREAT08, and modified by TDK for GREAT10.

Method	$Q$	$Q_{\text{dn}}$	$Q_{\text{dn}} \& \text{trained}$	$m$	$c/10^{-4}$	$\mathcal{M}/2$	$\sqrt{A}/10^{-4}$
<sup>†</sup> ARES 50/50	125.42	215.09	314.97	-0.026483	0.35	-0.035748	0.46
<sup>†</sup> cat7unfold2 (ps)	190.22		188.06			-0.013722	0.44
DEIMOS C6	67.71	149.88	315.59	0.006554	0.08	0.012131	0.39
fit2-unfold (ps)	288.77		304.11			-0.046022	0.40
gfit den cs	124.65	253.99	242.55	0.007611	0.29	0.010557	0.36
KSB	119.48	174.16	220.48	-0.059520	0.86	-0.062690	0.57
*KSB f90	58.29	148.83	265.33	-0.008352	0.19	0.001187	0.50
*im3shape NBC0	99.71	146.57	236.93	-0.049982	0.12	-0.080900	0.61
<sup>†</sup> MegaLUTsim2.1 b20	90.72	99.79	166.34	-0.265354	-0.55	-0.233981	0.87
method 4	106.85	119.85	158.73	-0.174896	-0.12	-0.120779	0.64
<sup>†</sup> NN23 func	104.76	70.46	11.43	-0.239057	0.47	-0.029440	0.61
shapefit	47.00	88.75	192.46	0.108292	0.17	-0.028606	0.52

**Table 3.** The Quality factors,  $Q$ , with denoising and training, and the  $m$  and  $c$  values for each method (not available for power spectrum submissions) that we explore in detail in this paper, in alphabetical order of the methods name. A “(ps)” indicates a power spectrum submission, in these cases  $Q_{\text{dn}} \& \text{trained} = Q_{\text{trained}}$ , all others were ellipticity catalogue submissions. An \* indicates that this team had knowledge of the internal parameters of the simulations, and access to the image simulation code. A <sup>†</sup> indicates that this submission was made in the post-challenge time period.

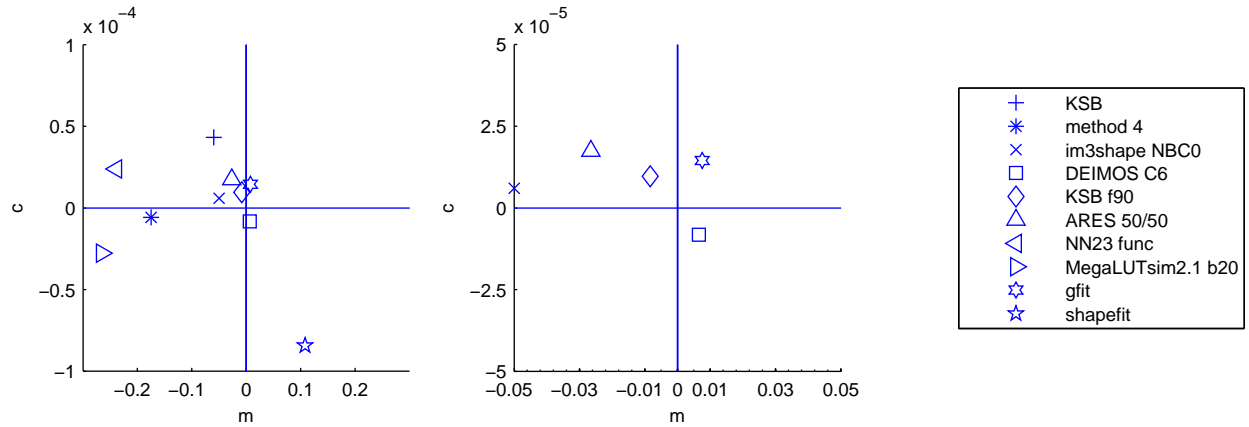


**Figure 1.** In the lefthand panel we show the multiplicative  $m$  and additive  $c$  biases for each ellipticity catalogues method, for which one-point estimators can be calculated, see Appendix B. The symbols indicate the method with a legend in the righthand panel. The central panel expands the x- and y-axes to show the best performing methods.

$$C_\ell \rightarrow \frac{C_\ell - \mathcal{A}_{\text{set}=7}}{1 + \mathcal{M}_{\text{set}=7}} \quad (9)$$

to calibrate the method using the training data. In Figure 3 we show the resulting Quality factors where we apply both a denoising step and a training step and when we apply a training step only. When both steps are applied we find that Quality factor improves by a factor  $\gtrsim 2$  and some methods perform as well as the ‘fit2-unfold’ method (if not better). In particular ‘DEIMOS C6’ achieves an average Quality factor of 316 (see Table 3). We find that the increase in the quality factor is uniform over all sets, including the low signal-to-noise sets.

We conclude that it was a combination of model calibration on the data, and using a denoised power spectrum, that enabled ‘fit2-unfold’ to win the challenge. We also conclude that calibration of measurements on high signal-to-noise samples, i.e. those that could be observed using a deep survey within a wide/deep survey strategy, is an approach that can improve shape measurement accuracy by about a factor of two. Note that using this approach is not doing shear calibration as it is practiced historically because

the true shear is not known. This holds as long as the deep survey is a representative sample and the PSF of the deep data has similar properties to the PSF in the shallower survey.

#### 4.2.2 Multi-epoch data

In Figure 3 we show how  $Q_{\text{dn}}$  varies for each submission averaged over all those sets that had a fixed intrinsic ellipticity field (Type 2) or a fixed PSF (Type 3), described in Section 3.1. Despite the simplicity of this implementation we find that for the majority of methods, this variation, corresponding to multi-epoch data, results in an improvement of approximately 1.1 to 1.3 in  $Q_{\text{dn}}$ , although there is large scatter in the relation. In GREAT10 the coordination team made a decision to keep the labelling of the sets private, so that participants were not explicitly aware that these particular sets had the same PSF (although the functional PSFs were available) or the same intrinsic ellipticity field. These were designed to test stacking methods, however no such methods were submitted. The approach of including this kind of subset can form a basis for

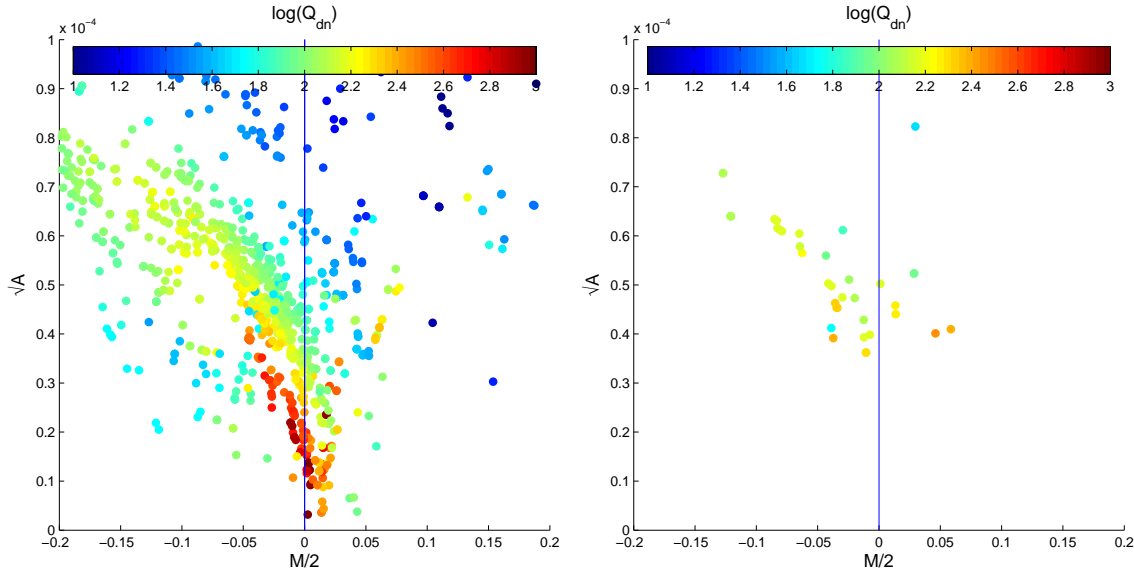


**Figure 2.** In the lefthand panel we show  $\mathcal{M}$  and  $\mathcal{A}$  for each method for each set. The colour scale represents the logarithm of the quality factor  $Q_{\text{dn}}$ . In the righthand panel we show the metrics  $\mathcal{M}$ ,  $\mathcal{A}$  and  $Q_{\text{dn}}$  for each method averaged over all sets. For a breakdown of these into dependence on set type see Figure 4.

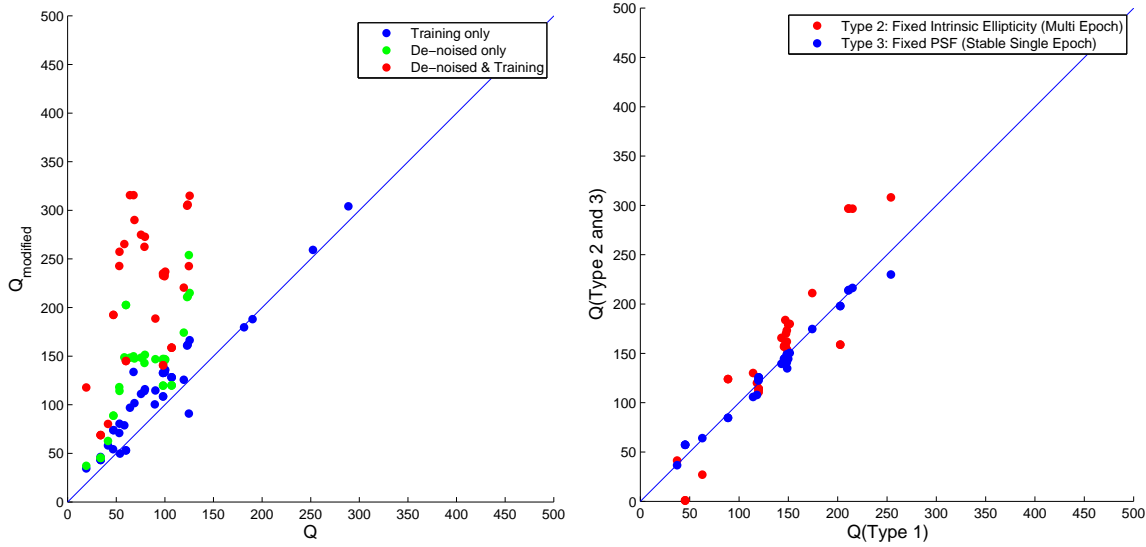


**Figure 3.** In the lefthand panel we show the un-modified quality factor  $Q$  (equation 1) and how this relates to the quality factor with pixel (shape measurement) noise removed  $Q_{\text{dn}}$  and the quality factor obtained when high signal to noise training is applied to each submission (equation 9). Methods that submitted power spectra could not be modified to remove the denoising in this way, so only show the training values are shown. The righthand panel shows the  $Q_{\text{dn}}$  for those sets with fixed intrinsic ellipticities (‘multi-epoch’; Type 2) or a fixed PSF (‘stable single epoch’; Type 3) over all images compared to the quality factor in the variable PSF and intrinsic ellipticity case (‘single epoch’; Type 1).

further investigations.

As a summary we show in Figure 4 how the population of  $\mathcal{M}$ ,  $\mathcal{A}$  and  $Q_{\text{dn}}$  parameters for each of the quantities that were varied between the sets, for all methods (averaging over all the other properties of the sets that are kept constant between these variations). In the following Sections we will analyse each behaviour in detail.

#### 4.2.3 Galaxy signal-to-noise

In the top row of Figure 5 we show how the metrics for each method change as a function of the galaxy signal-to-noise. We find a clear trend for all methods to achieve better measurements on higher signal-to-noise galaxies; with higher  $Q$  values and a smaller multiplicative and additive biases  $\mathcal{M}$  and  $\mathcal{A}$ . In particular ‘fit2-unfold’, ‘cat2-unfold’, ‘shapefit’ and ‘KSB f90’ have a close to zero multiplicative bias for  $S/N > 20$ . Because signal-to-noise has a particularly strong impact we tabulate the  $\mathcal{M}$  and  $\mathcal{A}$  values in Table 4. We also show in the lower row of Figure 5 the breakdown of the multiplicative and additive biases into the com-



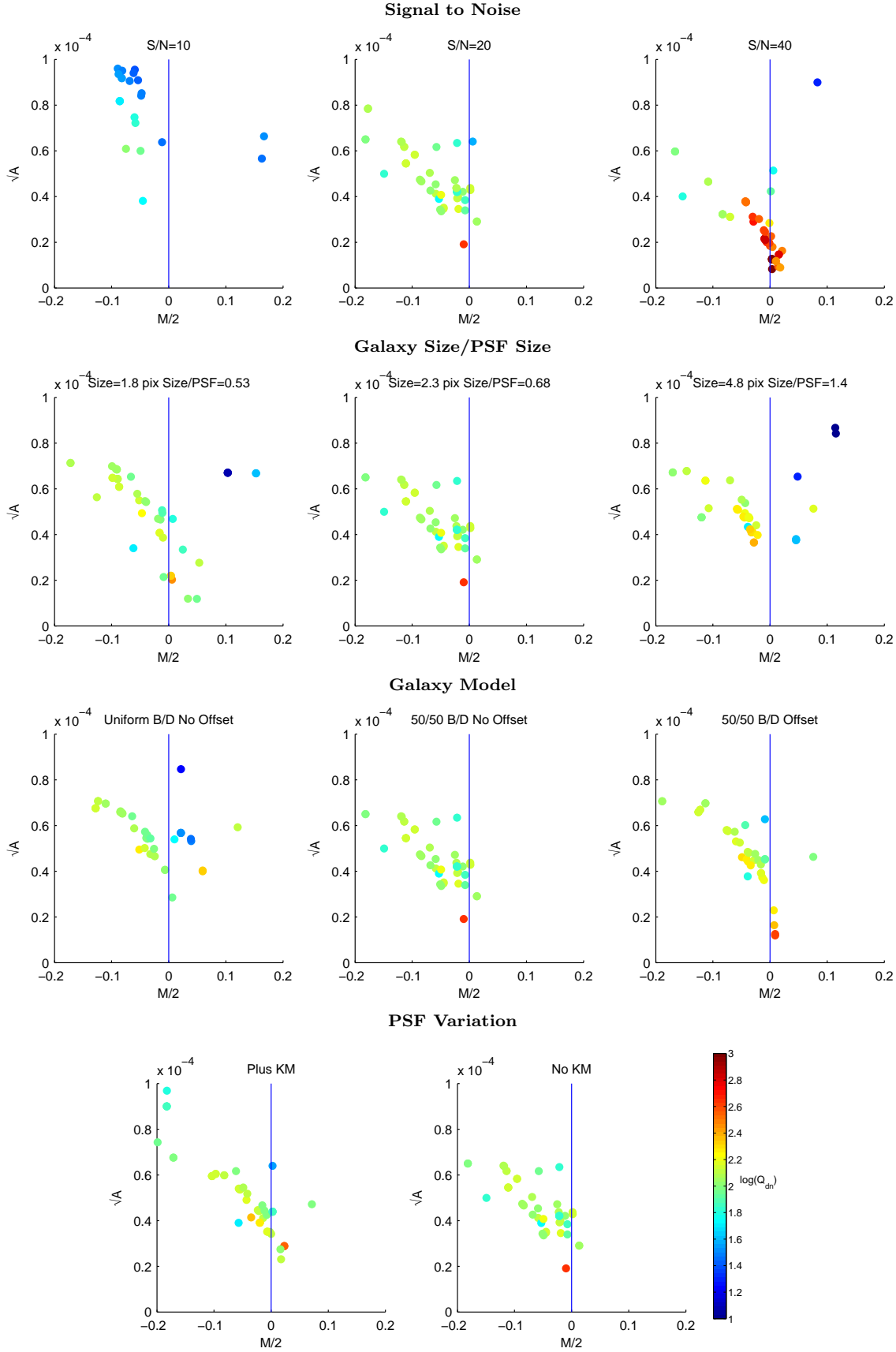


**Figure 4.** In each panel we show the metrics,  $\mathcal{M}$ ,  $\mathcal{A}$  and  $Q_{\text{dn}}$ , for each of the parameter variations between sets, for each submission; the colour scale labels the logarithm of  $Q_{\text{dn}}$  as show in the lower right. The first row shows the signal-to-noise variation, the second row shows the galaxy size variation, the third row shows the galaxy model variation (the galaxy models are: uniform bulge-to-disk fractions where each galaxy has a b/d ratio randomly sampled from the range  $b/d = [0.3, 0.95]$  with no offset (Uniform B/D No Offset), a 50% bulge-to-disk fraction  $b/d = 0.5$  with no offset (50/50 B/D No Offset) and a 50% bulge-to-disk fraction  $b/d = 0.5$  with a bulge/disk centroid offset (50/50 B/D Offset)), the fourth row shows PSF variation with and without Kolmogorov (KM) PSF variation.

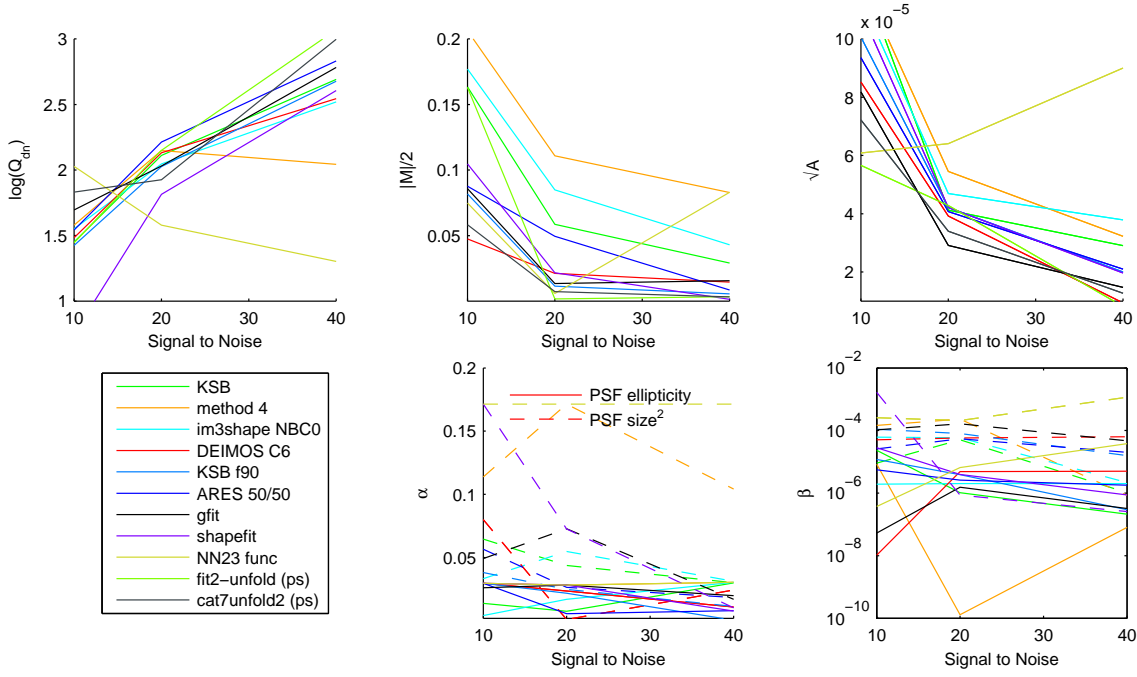


**Figure 5.** In the top panels we show how the metrics,  $\mathcal{M}$ ,  $\mathcal{A}$  and  $Q_{\text{dn}}$  for submissions change as the signal-to-noise increases; the colour scale labels the logarithm of  $Q_{\text{dn}}$ . In the lower panels we show the PSF size and ellipticity contributions  $\alpha$  and  $\beta$ . In the bottom-lefthand panel we show the key that labels each method.

	S/N=10		S/N=20		S/N=40	
Method	$\mathcal{M}/2$	$\sqrt{\mathcal{A}}/10^{-4}$	$\mathcal{M}/2$	$\sqrt{\mathcal{A}}/10^{-4}$	$\mathcal{M}/2$	$\sqrt{\mathcal{A}}/10^{-4}$
<sup>†</sup> ARES 50/50	0.087731	0.935697	0.049419	0.407512	0.008458	0.209666
<sup>†</sup> cat7unfold2 (ps)	0.058300	0.722149	0.007312	0.339832	-0.003201	0.126659
DEIMOS C6	0.047518	0.852336	0.021164	0.392274	-0.014486	0.094460
fit2-unfold (ps)	-0.162941	0.565951	-0.001792	0.428405	-0.003452	0.082378
gfit	0.085774	0.817820	-0.013417	0.290786	-0.015567	0.146713
KSB	0.163389	1.225922	0.058562	0.412507	0.029040	0.290177
*KSB f90	0.081783	1.007300	0.011454	0.421214	0.005595	0.199879
*im3shape NBC0	0.177015	1.141387	0.084891	0.469249	0.042984	0.378769
<sup>†</sup> MegaLUTsim2.1 b20	0.527131	1.591224	0.177168	0.785525	0.203427	0.758546
method 4	0.206427	1.205432	0.110811	0.545012	0.082873	0.322588
<sup>†</sup> NN23 func	0.074866	0.608485	-0.005973	0.640604	-0.083064	0.899982
shapefit	-0.104730	1.095732	0.021622	0.421100	0.001374	0.196678

**Table 4.** The metrics  $\mathcal{M}/2 \simeq m$  and  $\sqrt{\mathcal{A}} \simeq \sigma(c)$  for each of the signal-to-noise values used in the simulations.

ponents that are correlated with the PSF size and ellipticity (see Table 1). We find that for the methods with the smallest biases at high signal-to-noise (e.g. ‘DEIMOS’, ‘KSB f90’, ‘ARES’) the contribution from the PSF size is also small. For all methods we find that the contribution from PSF ellipticity correlations is subdominant.

#### 4.2.4 Galaxy size

In Figure 6 we show how the metrics of each method change as a function of the galaxy size – the mean PSF size was  $\simeq 3.4$  pixels. Note that the PSF size is statistically the same in each set, such that a larger galaxy size corresponds to either a case where the galaxies are larger in a given survey or where observations are

taken where the pixel size and PSF size are relatively smaller for the same galaxies.

We find that the majority of methods have a weak dependency on the galaxy size, but that at scales of  $\lesssim 2$  pixels, or size/mean PSF size  $\simeq 0.6$ , the accuracy decreases (larger  $\mathcal{M}$  and  $\mathcal{A}$  and smaller  $Q_{\text{dn}}$ ). This weak dependence is partly due to the small (but realistic) dynamical range in size, compared to a larger dynamical range in signal-to-noise. The exceptions are ‘cat7unfold2’, ‘fit2unfold’ and ‘shapefit’ that appear to perform very well on the fiducial galaxy size and less well on the small and large galaxies – this is consistent with the model calibration approach of these methods, which was done on Set 7 that used the fiducial galaxy type. The PSF size appears to have a small contribution at large galaxy sizes, as one should ex-

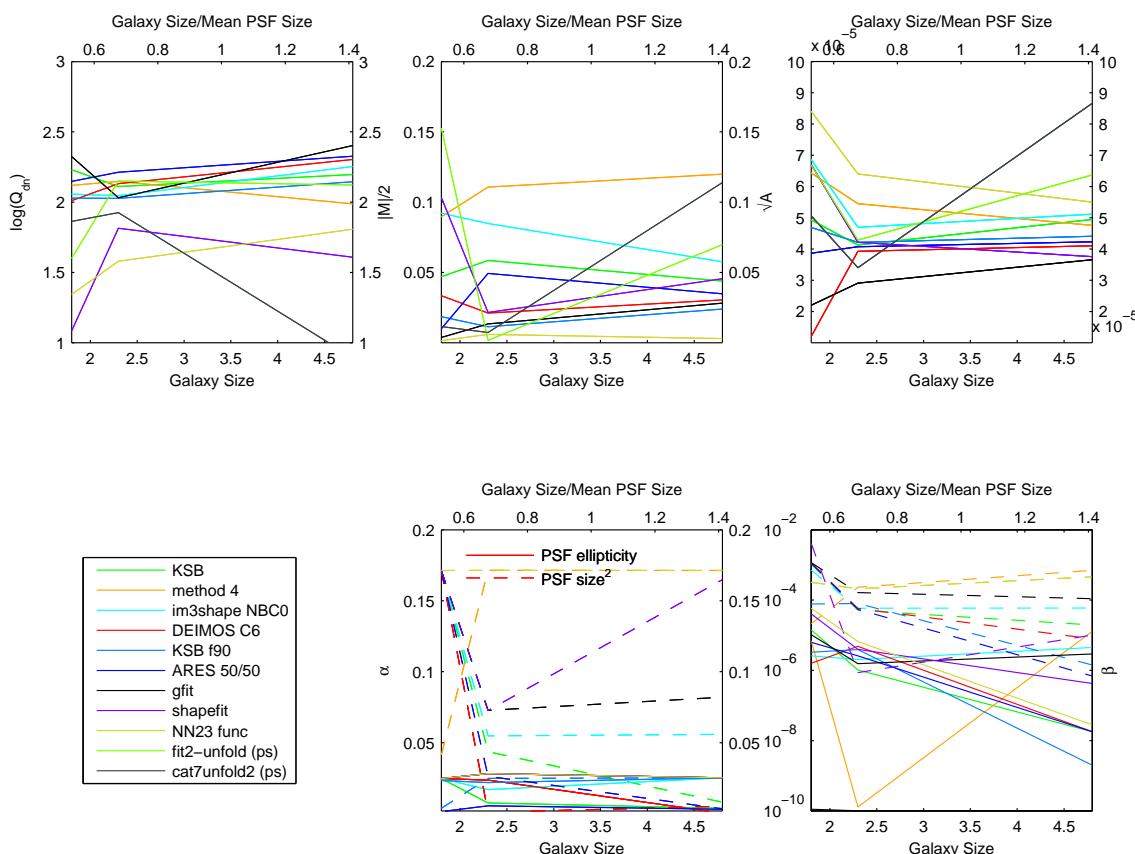


**Figure 6.** In the top panels we show how the metrics,  $M$ ,  $A$  and  $Q_{\text{dn}}$  for submissions change as the galaxy size increases; the colour scale labels the logarithm of  $Q_{\text{dn}}$ . In the lower panels we show the PSF size and ellipticity contributions  $\alpha$  and  $\beta$ . In the bottom-left panel we show the key that labels each method. The mean PSF is the mean within an image not between all sets.

pect, but a large contribution to the biases at scales smaller than the mean PSF size. We find that the methods with largest biases have a strong PSF size contribution. Again the PSF ellipticity has a subdominant contribution to the biases for all galaxy sizes.

#### 4.2.5 Galaxy model

In Figure 7 we show how each method’s metrics change as a function of the galaxy type. The majority of methods have a weak dependency on the galaxy model. The exceptions, similar to the galaxy size dependence, are ‘cat7unfold2’, ‘fit2unfold’ and ‘shapefit’ that appear to perform very well on the fiducial galaxy model and less so on the small and large galaxies – this again is consistent with model calibration approach of these methods. Again the contribution from the PSF size dependence is dominant over the PSF ellipticity dependence, and is consistent with no model dependency for the majority of methods, except those highlighted here. We refer to Section 4.4 and Appendix E for a breakdown of  $m$  and  $c$  behaviour as a function of galaxy model for each method.

#### 4.2.6 PSF model

In Figure 8 we show the impact of changing the PSF spatial variation on the metrics for each method. We

show results for the fiducial PSF, which does not include a Kolmogorov (turbulent atmosphere) power spectrum, and one which includes a Kolmogorov power spectrum in PSF ellipticity. We find that the majority of methods have a weak dependence on the inclusion of the Kolmogorov power. But it should be noted that participants knew the local PSF model exactly in all cases.

For the Kolmogorov power the PSF size dependence has a similar order of magnitude to the PSF ellipticity dependence for the additive bias  $A$ . This is different to the other set-dependencies. This can be explained by the fact that the spatial ellipticity variation in the other sets is lower than in the Kolmogorov sets.

#### 4.3 Averaging methods

In order to reduce shape measurement biases one may also wish to average together a number of shape measurement methods. In this way any random component, and any biases, in the ellipticity estimates may be reduced. In fact the ‘ARES’ method (see Appendix E) averaged catalogues from DEIMOS and KSB and attained better quality metrics. Doing this exploited the fact that DEIMOS had in some sets a strong response to the ellipticity whereas KSB had a weak response.

To test this we averaged the ellipticity catalogues

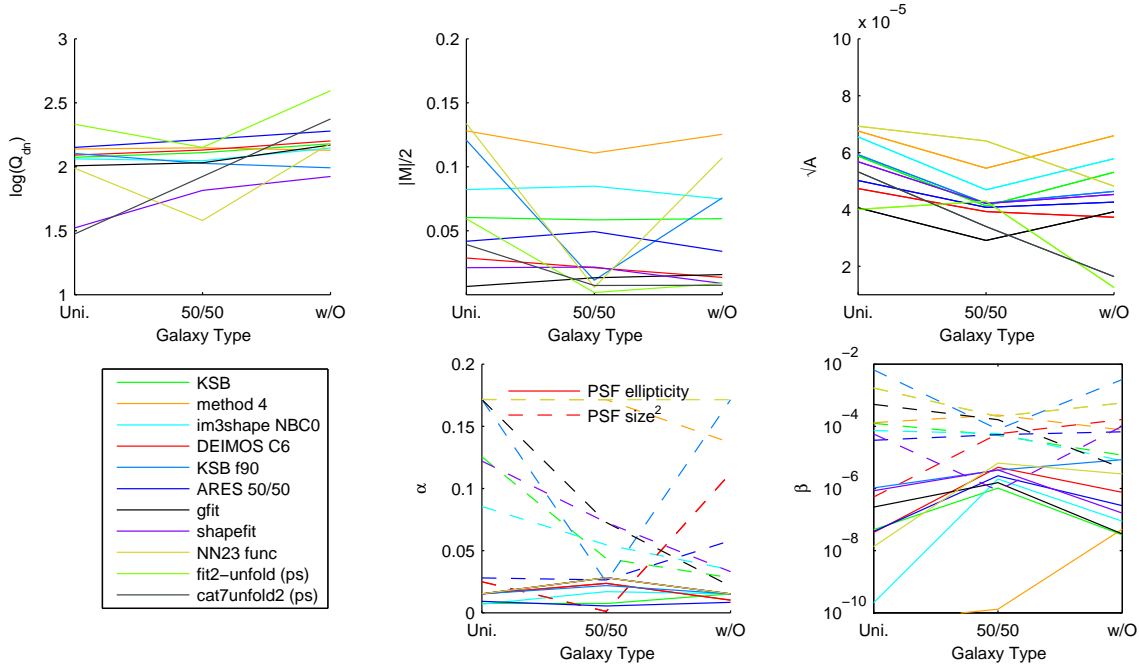


**Figure 7.** In the top panels we show how the metrics,  $\mathcal{M}$ ,  $\mathcal{A}$  and  $Q_{\text{dn}}$  for submissions change as the galaxy model changes; the colour scale labels the logarithm of  $Q_{\text{dn}}$ , the galaxy models are: uniform bulge-to-disk fractions each galaxy has a  $b/d$  ratio randomly sampled from the range  $b/d = [0.3, 0.95]$  with no offset (Uni.), a 50% bulge-to-disk fraction  $b/d = 0.5$  with no offset (50/50.) and a 50% bulge-to-disk fraction  $b/d = 0.5$  with a bulge/disk centroid offset (w/O). In the lower panels we show the PSF size and ellipticity contributions  $\alpha$  and  $\beta$ . In the bottom-lefthand panel we show the key that labels each method.

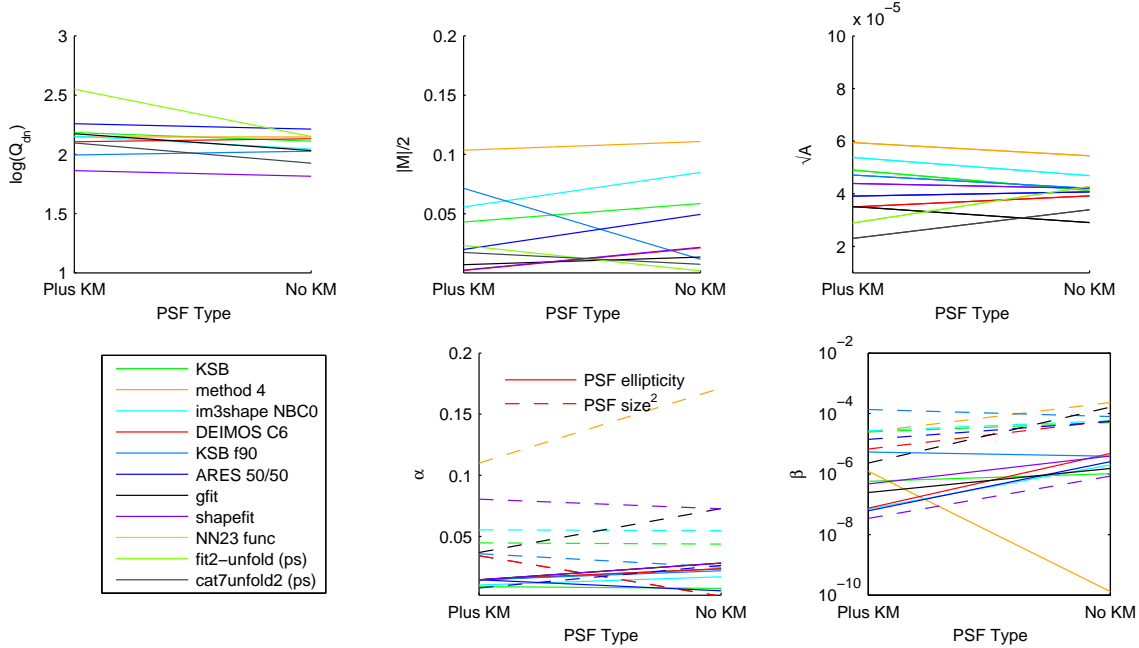


**Figure 8.** In the top panels we show how the metrics,  $\mathcal{M}$ ,  $\mathcal{A}$  and  $Q_{\text{dn}}$  for submissions change as the PSF model changes; the colour scale labels the logarithm of  $Q_{\text{dn}}$ , the PSF models are the fiducial PSF, and the same PSF except with a Kolmogorov power spectrum in ellipticity added. In the lower panels we show the PSF size and ellipticity contributions  $\alpha$  and  $\beta$ . In the bottom-lefthand panel we show the key that labels each method.

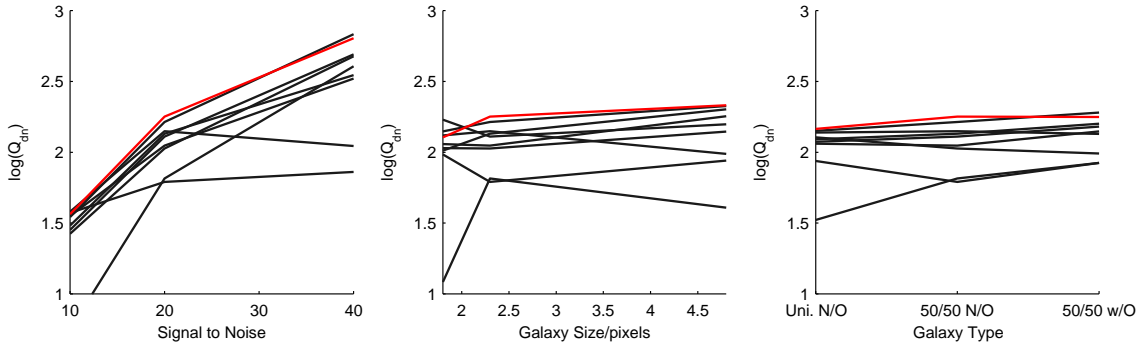


**Figure 9.** The Quality factor as a function of signal-to-noise (left panel), galaxy size (middle panel) and galaxy type (right panel) for an averaged ellipticity catalogue submission (red, using the averaging described in Section 4.3); compared to the methods used to average (black).

from the entries with the best metrics for each method that submitted an ellipticity catalogue (ARES 50/50, DEIMOS C6, gfit, im3shape NBC0, KSB, KSB f90, MegaLUTsim2.1 b20, method 4, shapefit) as so:

$$\langle e_i \rangle = \frac{\sum_{\text{methods}} e_{m,i} w_{m,i}}{\sum_{\text{methods}} w_{m,i}} \quad (10)$$

where  $i$  labels each galaxy and in general  $w_{m,i}$  is some weight that depends on the method, galaxy and PSF properties. We wish to weight methods that perform better, and so choose the Quality factor from the high signal-to-noise training set (set 7) as the weight  $w_{m,i} = Q_{\text{dn},m}(\text{set 7})$  applied over all other sets. This is close to an inverse variance weight on the noise induced on the shear power spectrum ( $\propto 1/\sigma_{\text{sys}}^2$ ). We leave the determination of optimal weights for future investigation.

We find that the average Quality factors over all sets for this approach are  $Q = 131$  and  $Q_{\text{dn}} = 210$ , which are slightly smaller on average than some of the individual methods. However we find that for the fiducial signal-to-noise and large galaxy size the Quality factor increases, see Figure 9. This suggests that such an averaging approach can improve the accuracy of an ellipticity catalogue but that a weight function should be optimised to be a function of signal-to-noise, galaxy size and type; however averaging many methods with a similar over or under estimation of the shear would not improve in the combination. If we take the highest quality factors in each set, as an optimistic case that a weight function had been found that could identify the best shape measurement in each regime we find an average  $Q_{\text{dn}} = 393$ .

#### 4.4 Overall performance

We now list some observations of method accuracy for each method by commenting on the behaviour of the metrics and dependencies shown in Section 4 and Appendix E. Words such as ‘relative’ are with respect to the other methods analysed here. This is a snapshot of methods performance as submitted for GREAT10 blind analysis.

- **KSB:** has low PSF ellipticity correlations, and a small galaxy morphology dependence, however it has a relatively large absolute  $m$  bias value.

- **KSB f90:** has small relative  $m$  and  $c$  biases on average, but a relatively strong PSF size and galaxy morphology dependence, in particular on the galaxy bulge fraction.

- **DEIMOS:** has small  $m$  and  $c$  biases on average, but a relatively strong dependence on galaxy morphology again in particular on the bulge fraction, similar to KSB f90. Dependence on galaxy size is low except for small galaxies with size smaller than the mean PSF.

- **im3shape:** has a relatively large PSF ellipticity and size correlation, a small galaxy size dependence for  $m$  and  $c$  but a stronger bulge fraction dependence.

- **gfit:** has relatively small average  $m$  and  $c$  biases, and a small galaxy morphology dependence, there is a relatively large correlation with PSF ellipticity. This was the only method to employ a denoising step at the image level, suggesting that this may be partly responsible for the small biases.

- **method 4:** has relatively strong PSF ellipticity, size and galaxy type dependence.

- **fit2unfold:** has strong model dependence, but relatively small  $m$  and  $c$  biases for the fiducial model type, and also a relatively low PSF ellipticity correlation.

- **cat2unfold:** has strong model dependence in particular on galaxy size, but relatively small  $m$  and  $c$  biases for the fiducial model type, and also a relatively low PSF ellipticity correlation.

- **shapefit:** has a relatively low quality factor, and a strong dependence on model types and size that are not the fiducial values, but small  $m$  and  $c$  biases for the fiducial model type.

To make some general conclusions, we find that

(i) Signal-to-noise: We find a strong dependence of the metrics below  $S/N = 10$ , however we find methods that meet requirements for the most ambitious experiments when  $S/N > 20$ .

(ii) Galaxy type: We find marginal evidence that model fitting methods have a relatively low dependence on galaxy type compared to KSB-like methods, but that this is only true if the model matches the underlying input model (note that GREAT10 used simple models). We find evidence that if one trains on a particular model then biases are small for this subset of galaxies.

(iii) PSF dependence: Despite the PSF being known exactly we find contributions to biases from

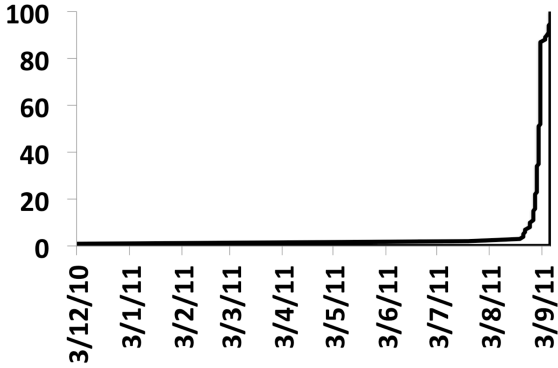


**Figure 10.** The cumulative submission number as a function of the challenge time, which started on 3<sup>rd</sup> December 2010 and ran for 9 months.

PSF size, but less so from PSF ellipticity. The methods with the largest biases have a strong PSF size correlation.

(iv) Galaxy Size: For large galaxies well sampled by the PSF, with scale radii  $\gtrsim 2$  times the mean PSF size we find that methods meet requirements on bias parameters for the most ambitious experiments. However if galaxies are unresolved with radii  $\lesssim 1$  time the PSF size biases become significant.

(v) Training: We find that calibration on a high signal-to-noise sample can significantly improve a method’s average biases. This is true whether training is a model calibration, or a more direct form of training on the ellipticity values of power spectra themselves.

(vi) Averaging Methods: We find that averaging methods is clearly beneficial, but that the weight assigned to each method will need to be correctly determined. An individual entry (ARES) found that this was the case, and we find similar conclusions when averaging over all methods.

## 5 ASTROCROWDSOURCING

The GREAT10 Galaxy Challenge was an example of ‘crowdsourcing’ astronomical algorithm development (‘astrocrowdsourcing’). This was part of a wider effort during this time period, that included the GREAT10 Star Challenge and the sister project Mapping Dark Matter<sup>5</sup> (see companion papers for these challenges). In this Section we discuss this aspect of the challenge and list some observations

GREAT10 was a major success in its effort to generate new ideas and attract new people into the field. For example, the winners of the challenge (authors D. Kirkby and D. Margala), were new to the field of gravitational lensing. A variety of entirely new methods have also been attempted for the first time on blind data, including the Look Up Table (MegaLUT) approach, an auto-correlation approach (method 4 and TVNN), and the use of training data. Furthermore the TVNN method is a real pixel-level deconvolution

method, which is the first time a genuine deconvolution of the data has been used in shape measurement.

The limiting factor in designing the scope of the GREAT10 Galaxy Challenge was the size of the simulations, that was kept below 1TB for ease of distribution; a larger challenge could have addressed even more observational regimes. In the future executables could be distributed that locally generate the data. However in this case participants may still need to store the data. Another approach might be to host challenges on a remote server where participants can upload and run algorithms. Care should be taken however to retain the integrity of the blindness of a challenge, without which results become largely meaningless as methods could be tuned to the parameters or functions of specific solutions if those solutions are known *a priori*. We require algorithms to be of high fidelity and to be useful on large amounts of data, which requires them to be fast: an algorithm that takes a second per galaxy needs  $\simeq 50$  CPU years to run on  $1.5 \times 10^9$  galaxies (the number observable by the most ambitious lensing experiments e.g. Euclid<sup>6</sup>, Laureijs et. al., 2011), a large simulation generates innovation in this direction.

In Figure 10 we show the cumulative submission of the GREAT10 Galaxy Challenge as a function of time, from the beginning of the challenge to the end and in the post-challenge submission period. All submissions (except one made by the GREAT10 coordination team) were made in the last 3 weeks of the 9 month period. For future challenges intra-challenge milestones could be used to encourage early submissions. This submission profile also reflects the size and complexity of the challenge; it took time for participants to understand the challenge and to run algorithms over the data to generate a submission. For future challenges submissions on smaller subsets of the data could be enabled, with submission over the entire data set being optional.

We note that the winning team (Kirkby and Margala) made 18 submissions during the challenge, compared to the mean submission number of 9. The winners also recognised from the information provided that the submission procedure was open to power spectrum and ellipticity catalogue submissions. The leaderboard was designed such that accuracy was reported in a manner that was indicative of performance, but such that this information could not be trivially used to directly calibrate methods (for example if  $m$  and  $c$  were provided a simple ellipticity catalogue correction could have been made).

Many of these issues were overcome in the sister Mapping Dark Matter challenge (see the Mapping Dark Matter results paper, Kitching et al., in prep) that received over 700 entries, over 2000 downloads of the data and a constant rate of submission. It also used an alternative model for leaderboard feedback where the simulated data was split into public and private sets, and useful feedback only provided for the public sets.

<sup>5</sup> Run in conjunction with Kaggle <http://www.kaggle.com/c/mdm>

<sup>6</sup> <http://www.euclid-ec.org>



## 6 CONCLUSIONS

The GREAT10 Galaxy Challenge was the first weak lensing shear simulation to include variable fields: both the PSF and the shear field varied as a function of position. It was also the largest shear simulation to date, consisting of over 50 million simulated galaxies, and a total of 1TB of data. The challenge ran for 9 months from December 2010 to September 2011, and during that time approximately 100 submissions were made.

In this paper we define a general pseudo-CL methodology for propagating shape measurement biases into cosmic shear power spectra and use this to derive a series of metrics that we use to investigate methods. We present a quality factor  $Q$  that relates the inaccuracy in shape measurement methods to the shear power spectrum itself. A  $Q = 1000$  denotes a method that could measure the dark energy equation of state parameter  $w_0$  with a bias less than or equal to the predicted statistical error from the most ambitious planned weak lensing experiments (for a more general expression we refer to Massey et al., in prep). We show how one can correct such a metric to account for pixel noise in a shape measurement method. During the challenge, submissions were publicly ranked on a live leaderboard and ranked by this metric  $Q$ .

We show how a variable shear simulation can be used to determine  $m$  and  $c$  parameters (Heymans et al., 2006) that are a measure of bias between the measured and true shear (those parameters used in constant shear simulations: STEP and GREAT08) on an object by object basis. We link the quality factor to linear power spectrum biases including a multiplicative  $\mathcal{M} \approx 2m$  and additive bias  $\mathcal{A} \propto \sigma(c)^2$  that are approximately related to the STEP one-point estimators of shape measurement bias. The equality is only approximate because in general  $\mathcal{M}$  and  $\mathcal{A}$  are a measure of spatially varying method biases. We introduce further metrics that allow an assessment of the contribution to the multiplicative and additive biases from correlations between the biases and any spatially variable quantity (in this paper we focus on PSF size and ellipticity).

The simulations were divided into sets of 200 images each containing a grid of 10,000 galaxies. In each set the shear field was spatially varying but constant between images. The challenge was to reconstruct the shear *power spectrum* for each set. Participants could submit either catalogues of ellipticities one per image or power spectra one for each set, and were provided with an exact functional description of the PSF and the positions of all objects to within half a pixel.

The simulations were structured in such a way that conclusions could be made about a shape measurement method's accuracy as a function of galaxy signal-to-noise, galaxy size, galaxy model/type and the PSF type. The simulations also contained some 'multi-epoch' sets in which the shear and intrinsic ellipticities were fixed between images in a set but where the PSF varied between images, and some 'static single-epoch' sets where the PSF was fixed between images in a set but the intrinsic ellipticity field varied between images. All fields were always spatially varying. Participants were provided with true shears

for one of the high signal-to-noise sets that they could use as a training set.

Despite the simplicity of the challenge, making conclusions about which aspects of which algorithm generated accurate shape measurement is difficult due to the complexity of the algorithms themselves (see Appendix E). We leave investigations into tunable aspects of each method to future work. We can however make some statements about the regimes in which methods perform well or poorly.

The best methods submitted to GREAT10 scored an average  $Q \simeq 300$  with  $m \simeq 7 \times 10^{-3}$  and  $c \simeq 10^{-5}$ , this is approximately a factor 3 improvement over previous performance on blind simulations (the best performing non-stacking method at a signal-to-noise 20, using the GREAT10 definition, in GREAT08 was CH which had an  $m = 0.0095 \pm 0.003$  and  $c \simeq 8 \times 10^{-4}$ ). The methods that won the challenge (scoring the highest  $Q$  on the leaderboard) employed a maximum likelihood model-fitting method. Several methods used the training data to test code, and we find that by directly training on a high signal-to-noise set the majority of methods achieve a factor of 2 increase in the average value of  $Q$ . We find some evidence that shape measurement inaccuracies can be reduced by averaging methods together, but conclude that for such a method to be usable an optimal weight for each method as a function of signal-to-noise and galaxy properties would have to be found.

For a signal-to-noise of 40 the best methods achieved a  $Q \gtrsim 1000$ ,  $m < 1 \times 10^{-3}$  and  $c < 1 \times 10^{-5}$ ; the majority of methods have an accuracy that is strongly dependent on signal-to-noise with  $Q \simeq 100$  and  $\simeq 50$  for signal-to-noise of 20 and 10 respectively. However the dependence on galaxy model (bulge-to-disk ratio or bulge-to-disk offset) and size is not strong. There is a contribution to the multiplicative bias  $m$  from PSF size correlations for the majority of methods over all sets, but a smaller contribution from PSF ellipticity dependence (as expected from theoretical calculations, e.g. Massey et al., in prep).

The testing of shape measurement methods by GREAT10 suggests methods now exist that can be used for cosmic shear surveys covering up to a few thousand square degrees ( $\lesssim 3000$  square degrees, that require  $m \lesssim 6 \times 10^{-3}$ ; Kitching et al., 2008<sup>7</sup>) to measure cosmological parameters in an unbiased fashion. We find that on the additive bias  $c$  methods already meet requirements for even the most ambitious surveys ( $c < 1 \times 10^{-3}$ ) over all simulated conditions, and that in the high signal-to-noise regime ( $\gtrsim 40$ ) methods already meet the most ambitious requirements on the multiplicative bias ( $m < 2 \times 10^{-3}$ ; Kitching et al., 2008) suggesting that such accuracy is possible for, or can at least be extrapolated down to, lower signal-to-noise, in principle. However we note that the requirements are on all galaxies in a survey and that the demonstration here is averaged over a simulation with particular properties, in particular the fiducial

<sup>7</sup> The scaling formula from this paper can be rewritten for the maximum applicable area of a survey for a given bias  $m$  as  $A_{\max} \lesssim 20,000[(0.001/m)^{2.4}/0.17/10^\beta]^{1/1.5}$  square degrees, assuming that the redshift behaviour is  $m \propto (1+z)^\beta$ .

signal-to-noise is 20. Therefore these conclusions have a caveat that the GREAT10 simulations were intentionally simplistic in some respects, so that clear statements about methods could be made, but they provide a foundation for shape measurement development to continue increasing in realism and complexity.

*Acknowledgements:* We thank the GREAT10 Advisory team for discussions before and after the challenge. TDK is supported by a Royal Society University Research Fellowship, and was supported by a Royal Astronomical Society 2010 Fellowship for the majority of this work. This work was funded by a EU FP7 PASCAL 2 Challenge Grant. Workshops for the GREAT10 challenge were funded by the eScience STFC Theme, PASCAL 2 and by JPL, run under a contract for NASA by Caltech, and hosted at the eScience Institute Edinburgh, by UCL and by IPAC at Caltech. We thank Bob Mann, Francesca Ziolkowska, Harry Teplitz and Helene Seibly for local organisation of the workshops. We thank Mark Holliman for system administrator tasks for the GREAT10 web server. We thank Whitney Clavin for assistance on the NASA press release for GREAT10. We thank Lance Miller comments on a first draft and throughout the challenge. We also thank Alan Heavens, Alina Keissling, Benjamin Joachimi, Marina Shmakova, Gary Bernstein, Konrad Kuijken, Yannick Mellier, Mark Cropper, Malin Velander, Elisabetta Semboloni, Henk Hoekstra, Karim Benabed for useful discussions. CH acknowledges support from the ERC under grant EC FP7 240185. SBr, MH, TKa, BR, JZ acknowledge support from ERC Starting Grant with number 240672. BR acknowledges support from the NASA WFIRST Project Office. DK and DM acknowledge the support of the US DOE. RM acknowledges support from a Royal Society University Research Fellowship.

*Contributions:* All authors contributed to the development of this paper. TDK was PI of GREAT10, created the simulations, and wrote this paper. CH, MG, RM, BR were active members of the GREAT10 coordination board during the challenge (12/2010 to 10/2011). SBr, FC, MG, SH, CH, MH, TK, DK, DM, LM, PM, GN, KP, BR, MT, LV, MV, JY, JZ submitted entries to the GREAT10 galaxy challenge. JR hosted and ran the GREAT10 challenge final workshop, TDK, CH, SBr, MH, TKa, RM, BR, LV, JZ were on the LOC for the mid-challenge workshops. SBa and SBr created the image simulation code for GREAT08 that was extended by TDK for the GREAT10 challenge. AT contributed to the a code on which the spatially varying field code was based, and provided consultation with regard to the pseudo-Cl formalism. DW maintained the GREAT10 leaderboard and processed submissions with TDK during the challenge.

## REFERENCES

- Albrecht, A. et al., 2006, eprint arXiv:astro-ph/0609591  
 Bartelmann, M., & Schneider, P. 2001, Phys REP, 340, 291  
 Bernstein, G. M., & Jarvis, M. 2002, AJ, 123, 583  
 Bertin, E. & Arnouts, S. 1996: SExtractor: Software for source extraction, *Astronomy & Astrophysics Supplement* 317, 393  
 Bridle, S., et al. 2009, *Annals of Applied Statistics*, 3, 6  
 Bridle, S., et al. 2010, MNRAS, 405, 2044  
 Brown, M. L., Castro, P. G., & Taylor, A. N. 2005, MNRAS, 360, 1262  
 Crittenden, R. G., Natarajan, P., Pen, U.-L., & Theuns, T. 2001, ApJ, 559, 552  
 Eisenstein, D. J., & Hu, W. 1999, ApJ, 511, 5  
 Heymans, C., Brown, M. L., Barden, M., et al. 2005, MNRAS, 361, 160  
 Heymans, C., Gray, M. E., Peng, C. Y., et al. 2008, MNRAS, 385, 1431  
 Heymans, C., Van Waerbeke, L., Bacon, D., et al. 2006, MNRAS, 368, 1323  
 Heymans, C., Rowe, B., Hoekstra, H., et al. 2011, arXiv:1110.4913  
 Hoekstra, H., Franx, M., Kuijken, K., & Squires, G. 1998, NAR, 42, 137  
 Hoekstra, H., & Jain, B. 2008, *Annual Review of Nuclear and Particle Science*, 58, 99  
 Hopfield J. J., 1982, PNAS April 1, 1982 vol. 79 no. 8 2554-2558  
 Hu, W. 1999, ApJ, 522, L21  
 Jarvis, M., Schechter, P., & Jain, B. 2008, arXiv:0810.0027  
 Kaiser, N., Squires, G., & Broadhurst, T. 1995, ApJ, 449, 460  
 Kitching, T. D., Amara, A., Abdalla, F. B., Joachimi, B., & Refregier, A. 2009, MNRAS, 399, 2107  
 Kitching, T. D., Heavens, A. F., & Miller, L. 2011, MNRAS, 413, 2923  
 Kitching, T. D., Miller, L., Heymans, C. E., van Waerbeke, L., & Heavens, A. F. 2008, MNRAS, 390, 149  
 Kitching et al., 2011, *Annals of Applied Statistics* 2011, Vol. 5, No. 3, 2231-2263  
 Kitching et al., 2012b, in prep  
 Kuijken, K. 2006, arXiv:astro-ph/0610606  
 Laureijs, R., et al. 2011, arXiv:1110.3193  
 Linder, E. V. 2003, arXiv:astro-ph/0311403  
 Luppino, G. A., & Kaiser, N. 1997, ApJ, 475, 20  
 Massey, R., et al. 2007, MNRAS, 376, 13  
 Massey, R., Kitching, T., & Richard, J. 2010, *Reports on Progress in Physics*, 73, 086901  
 Massey et al., (2012), in prep  
 Melchior, P., Viola, M., Schäfer, B. M., & Bartelmann, M. 2011, MNRAS, 412, 1552  
 emari, Y., 2010, PhD Thesis, Edinburgh University  
 Miralda-Escude, J. 1991, ApJ, 380, 1  
 Nurbaeva, G., Courbin, F., Gentile, M., & Meylan, G. 2011, AAP, 531, A144  
 Paulin-Henriksson, S., Amara, A., Voigt, L., Refregier, A., & Bridle, S. L. 2008, AAP, 484, 67  
 Rowe, B. 2010, MNRAS, 404, 350  
 Schneider, P., Eifler, T., & Krause, E. 2010, AAP, 520, A116  
 Smith, R. E., Peacock, J. A., Jenkins, A., et al. 2003, MNRAS, 341, 1311  
 Rudin L., I., 1992, *Physica D*, Volume 60, Issues 14, 1 November 1992, Pages 259268  
 van Waerbeke, L. 1998, AAP, 334, 1  
 Viola, M., Melchior, P., & Bartelmann, M. 2012, MNRAS, 419, 2215  
 Weinberg, D. H., Mortonson, M. J., Eisenstein, D. J., et al. 2012, arXiv:1201.2434



## APPENDIX A: PSEUDO-CL ESTIMATORS FOR WEAK LENSING

In this Section we describe a general formalism for the evaluation of variable shear systematics in weak lensing. We note that this has a more general application to that described here, such that any mask in general could be accounted for in weak lensing power spectrum estimation. This closely follows the pseudo-Cl formalism described in Memari (2010) and Brown et al. (2005) that has been applied in CMB studies, for survey masks.

We start by defining a generalised shear systematic response where

$$e_{\text{measure}}(\boldsymbol{\theta}) = \gamma(\boldsymbol{\theta}) + e_{\text{intrinsic}}(\boldsymbol{\theta}) + c(\boldsymbol{\theta}) + m(\boldsymbol{\theta})[\gamma(\boldsymbol{\theta}) + e_{\text{intrinsic}}(\boldsymbol{\theta})] + q(\boldsymbol{\theta})[\gamma(\boldsymbol{\theta}) + e_{\text{intrinsic}}(\boldsymbol{\theta})]|\gamma(\boldsymbol{\theta}) + e_{\text{intrinsic}}(\boldsymbol{\theta})| \quad (11)$$

where all variables are a function of position on the sky, and all are complex quantities (e.g.  $\gamma(\boldsymbol{\theta}) = \gamma_1(\boldsymbol{\theta}) + i\gamma_2(\boldsymbol{\theta})$ ). We expect that  $m(\boldsymbol{\theta})$  will in general depend on spatially varying quantities including PSF ellipticity and size or galaxy properties such as signal-to-noise, so that one could write  $m(\boldsymbol{\theta}) \rightarrow m(\text{PSF}(\boldsymbol{\theta}), \text{Galaxy}(\boldsymbol{\theta}))$  or  $m(e_{\text{PSF}}(\boldsymbol{\theta}), r_{\text{PSF}}(\boldsymbol{\theta}), \text{S/N}(\boldsymbol{\theta}), \dots)$  for example, but this does not qualitatively change the following treatment. We note also that in general the systematic terms can also be complex  $m(\boldsymbol{\theta}) = |m(\boldsymbol{\theta})|e^{i\phi[\boldsymbol{\theta}]}$ , here we assume a scalar spatially varying quantity, and will investigate further generalisation in future work.

The E and B mode decomposition of the spin-2 field  $e_{\text{measure}}(\boldsymbol{\theta})$  can be written in general as a rotation in Fourier space (see GREAT10 handbook) such that

$$\begin{aligned} E(\boldsymbol{\ell}) \pm iB(\boldsymbol{\ell}) &= \ell^* |\ell|^{-2} [e_{1,\text{measure}}(\boldsymbol{\ell}) + ie_{2,\text{measure}}(\boldsymbol{\ell})] \\ E(\boldsymbol{\ell}) \pm iB(\boldsymbol{\ell}) &= e^{\mp 2i\phi_{\boldsymbol{\ell}}} [e_{1,\text{measure}}(\boldsymbol{\ell}) + ie_{2,\text{measure}}(\boldsymbol{\ell})] \end{aligned} \quad (12)$$

where  $e_{\text{measure}}(\boldsymbol{\ell})$  is the Fourier transform of  $e_{\text{measure}}(\boldsymbol{\theta})$ .

When creating a power spectrum the auto-correlations of the first three terms of equation (11) have a simple interpretation, but the fourth term has an effective weight map as a function of position such that (only focusing on the contribution from the fourth term) we have that the estimated E and B-mode terms are

$$\tilde{E}(\boldsymbol{\ell}) \pm i\tilde{B}(\boldsymbol{\ell}) = \int \frac{d^2\ell'}{(2\pi)^2} e^{\mp 2i\phi_{\boldsymbol{\ell}}} W_m(\boldsymbol{\ell} - \boldsymbol{\ell}') [E(\boldsymbol{\ell}') \pm iB(\boldsymbol{\ell}')], \quad (13)$$

where  $W_m$  is 2D Fourier transform of the  $m(\boldsymbol{\theta})$  field. Equivalently for the E-mode part only we have

$$\tilde{E}(\boldsymbol{\ell}) = \int \frac{d^2\ell'}{(2\pi)^2} W_m(\boldsymbol{\ell} - \boldsymbol{\ell}') [\cos(2(\phi_{\boldsymbol{\ell}} - \phi_{\boldsymbol{\ell}'}))E(\boldsymbol{\ell}') - \sin(2(\phi_{\boldsymbol{\ell}} - \phi_{\boldsymbol{\ell}'}))B(\boldsymbol{\ell}')], \quad (14)$$

where this equation has the interpretation of a rotation of E and B to ellipticity in Fourier space, a convolution with the window/weight function and then a rotation back to E and B. We now wish to compute the effect that the weight map has on the E-mode power. In Fourier space the auto and cross power are defined as

$$\langle X_i(\boldsymbol{\ell}) X_j^*(\boldsymbol{\ell}') \rangle = (2\pi)^2 C_{\ell}^{X_i X_j} \delta^D(\boldsymbol{\ell} - \boldsymbol{\ell}') \quad (15)$$

where isotropy of the field is assumed. This means that an unbiased estimator can be written in the flat sky limit as an average over angle in  $\ell$ -space

$$\langle C_{\ell}^{X_i X_j} \rangle = \int \frac{d\phi_{\ell}}{(2\pi)} \langle X_i(\boldsymbol{\ell}) X_j^*(\boldsymbol{\ell}') \rangle. \quad (16)$$

Hence by taking the correlation function of equation (14) we can calculate the estimated power spectrum in the presence of a systematic weight map. This follows the calculations of Memari (2010), the resulting expressions for the EE power and BB power are below, and we include the EB expression for completeness (however in the flat sky limit there is no EE, BB and EB mixing; there is between EE and BB though)

$$\begin{aligned} \langle \tilde{C}_{\ell}^{EE} \rangle &= \int \frac{d^2\ell'}{(2\pi)^2} \left\{ \int dL L \frac{W_{mm}(L)}{\ell\ell' \sin \eta} ([1 + \cos 4\eta] \langle C_{\ell'}^{EE} \rangle + [1 - \cos 4\eta] \langle C_{\ell'}^{BB} \rangle) \right\} \\ \langle \tilde{C}_{\ell}^{EB} \rangle &= \int \frac{d^2\ell'}{(2\pi)^2} \left\{ \int dL L \frac{W_{mm}(L)}{\ell\ell' \sin \eta} 2 \cos 4\eta \langle C_{\ell'}^{EB} \rangle \right\} \\ \langle \tilde{C}_{\ell}^{EE} \rangle &= \int \frac{d^2\ell'}{(2\pi)^2} \left\{ \int dL L \frac{W_{mm}(L)}{\ell\ell' \sin \eta} ([1 - \cos 4\eta] \langle C_{\ell'}^{EE} \rangle + [1 + \cos 4\eta] \langle C_{\ell'}^{BB} \rangle) \right\}, \end{aligned} \quad (17)$$

where the additional  $L$ -mode forms a triangle with  $\ell$  and  $\ell'$ , ( $|\ell - \ell'| < L < \ell + \ell'$ ), with  $\cos \eta = (\ell^2 + \ell'^2 - L^2)/2\ell\ell'$  and similarly for  $\sin \eta$  and  $W_{mm}$  is the angle-average of the modulus squared of the weight function

$$W_{mm}(L) \equiv \int \frac{d\phi_{\ell}}{(2\pi)} |W_m(\boldsymbol{L})|^2. \quad (18)$$

In the discrete case we can write equations (17) in a compact form using *mixing matrices* such that

$$\begin{pmatrix} \langle \tilde{C}_{\ell}^{EE} \rangle \\ \langle \tilde{C}_{\ell}^{BB} \rangle \end{pmatrix} = \sum_{\ell'} \begin{pmatrix} M_{\ell\ell'}^{EE,mm} & M_{\ell\ell'}^{BB,mm} \\ M_{\ell\ell'}^{EB,mm} & M_{\ell\ell'}^{EB,mm} \end{pmatrix} \begin{pmatrix} \langle C_{\ell'}^{EE} \rangle \\ \langle C_{\ell'}^{BB} \rangle \end{pmatrix}, \quad (19)$$

where

$$M_{\ell\ell'}^{EE,mm} \equiv \frac{\Delta\ell'\ell'}{(2\pi)^2} \sum_L \Delta L L W_{mm}(L) \frac{1 + \cos 4\eta}{\ell\ell' \sin \eta}$$

$$M_{\ell\ell'}^{BB,mm} \equiv \frac{\Delta\ell'\ell'}{(2\pi)^2} \sum_L \Delta LLW_{mm}(L) \frac{1 - \cos 4\eta}{\ell\ell' \sin \eta}, \quad (20)$$

and similarly for the EB power. These expressions assume that the systematic fields are uncorrelated with the shear and intrinsic ellipticity fields. This may not be the case in real data (e.g. selection effects over galaxy populations may have particular biases), but for GREAT10 selection effects are not investigated and the biases are quoted as averages over populations. We leave a generalisation of this formalism to correlated systematic-ellipticity fields for future work.

Using this we can write a power spectrum estimate of the quantities in equation (11) (we drop the angle brackets over  $\phi_\ell$  for clarity from here) including the  $\gamma$ I cross term

$$\begin{aligned} \tilde{C}_\ell^{EE} &= (1 + 2m_\ell)[C_\ell^{EE,\gamma\gamma} + C_\ell^{EE,II} + C_\ell^{EE,\gamma I}] + \mathcal{A}_\ell^{EE} \\ &+ \sum_{\ell'} (M_{\ell\ell'}^{EE,mm}[C_{\ell'}^{EE,\gamma\gamma} + C_{\ell'}^{EE,II} + C_{\ell'}^{EE,\gamma I}] + M_{\ell\ell'}^{BB,mm}[C_{\ell'}^{BB,\gamma\gamma} + C_{\ell'}^{BB,II} + C_{\ell'}^{BB,\gamma I}]) \end{aligned} \quad (21)$$

where  $\mathcal{A}_\ell$  is the angle averaged power spectrum of the  $c(\theta)$  variation; here, through isotropy, is it assumed that that the power contains all relevant information. This could be generalised to include non-isotropic variation in all terms i.e. not taking the angle averages.  $m_\ell$  is the angle averaged Fourier transform of  $m(\theta)$ . Our notation, for example  $C_\ell^{EE,AB}$ , refers to the  $EE$  power corresponding to correlations between quantities  $A$  and  $B$  as a function of  $\ell$ . We do not include terms from the quadratic  $q(\theta)$  contribution. For GREAT10 the  $\gamma$  field is E-mode only and the intrinsic ellipticity field is B-mode only, with no  $\gamma$ I term, so we have a simpler expression

$$\tilde{C}_\ell^{EE} = (1 + 2m_\ell)C_\ell^{EE,\gamma\gamma} + \mathcal{A}_\ell^{EE} + \sum_{\ell'} (M_{\ell\ell'}^{EE,mm}C_{\ell'}^{EE,\gamma\gamma} + M_{\ell\ell'}^{BB,mm}C_{\ell'}^{BB,II}). \quad (22)$$

These expressions are general for any shape measurement biases, and are trivially extendable to include cross-terms that may appear in real data (e.g.  $\langle cm \rangle$  cross terms) if required.

Equation (22) represents the general impact that shape measurement inaccuracies in GREAT10 can propagate through to the shear power spectrum. In the case that the weight-map is constant ( $m(\theta) = \text{constant} = m_0$ ) (i.e. non-isotropic) the Fourier transform becomes a delta-function and the mixing matrices become  $M_{\ell\ell}^{EE,mm} = I_{N_\ell} \times m_0^2 = \mathcal{M}(\ell)$  and  $M_{\ell\ell'}^{BB,mm} = 0$ . This leads to

$$\tilde{C}_\ell^{EE} = C_\ell^{EE,\gamma\gamma} + \bar{\mathcal{A}} + \bar{\mathcal{M}}C_\ell^{EE,\gamma\gamma} \quad (23)$$

where  $\mathcal{M} = 2m_0 + m_0^2$  and where we take a mean value of  $\mathcal{A} = (2\pi/\ell_{\max})\sigma(c)^2$  over  $\ell$ . In general the mixing matrices are not only dependent on a single  $\ell$  (i.e. diagonal  $M_{\ell\ell}$ ) except in the case that the systematic is isotropic or constant. Unfortunately this is likely not to be the case in weak lensing where for example PSF ellipticity and size is often coherent but not constant across a field of view. Massey et al (in prep) will discuss requirements on these parameters  $\mathcal{M}$  and  $\mathcal{A}$ , and how they relate to uncertainty in PSF parameters.

We note that this formalism means that we only need to recover the statistical properties of the varying  $m(\theta)$  field (the power spectrum and mixing matrix) in order to propagate its impact through to the shear power spectrum. In addition, as shown in Appendix B, this formalism can also be used to generate expressions for correlation coefficients between the systematic  $m(\theta)$  and  $c(\theta)$  fields and any spatially varying quantity. Given these definitions and formalism we can now proceed to outline the metrics used in this paper, taking into account some practicalities such as pixel noise removal.

## APPENDIX B: DESCRIPTION OF THE EVALUATION METRICS

The variable shear nature of the simulations enables a variety of metrics to be calculated, each of which allow us to infer different properties of the shape measurement method under scrutiny. In this paper we define a variety of metrics that we explain in detail in this Section.

### B1. Quality factor

In general for a variable field we define the power spectrum as the Fourier transform of the correlation function as described in Appendix A. We wish to compare the power reconstructed from the submissions against the true shear power spectrum and so define a baseline evaluation metric, the quality factor (Q), as

$$Q = 1000 \frac{5 \times 10^{-6}}{\int d\ln \ell |\tilde{C}_\ell^{EE} - C_\ell^{EE,\gamma\gamma}| \ell^2}. \quad (24)$$

The numerator  $5 \times 10^{-6}$  is calculated by generating Monte Carlo realisations of a mock submitted power spectra and calculating the bias in the dark energy equation of state parameter  $w_0$  (Linder, 2003) which would occur if such an observation were made (using the functional form filling formalism described in Kitching et al., 2008) over a survey of 20,000 square degrees using the same redshift distribution as described in Section 3.2. In Figure 11 we show the result of this procedure for GREAT10 (where the numerator in equation 24 is labelled as  $\sigma_{\text{sys}}^2$ ), where we take a threshold value of bias-to-error ratio of 1. This is in fact conservative as shown in Massey et al.,

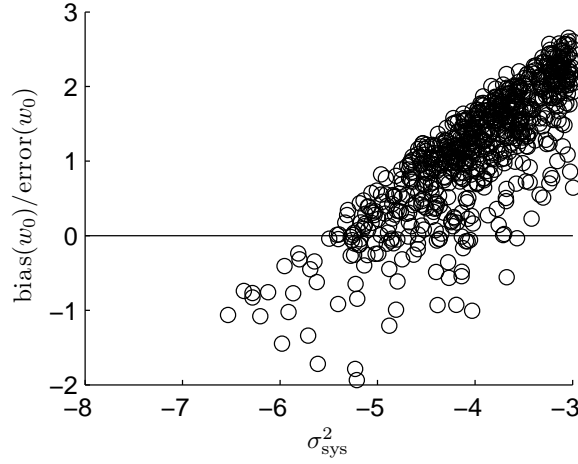


**Figure 11.** Monte Carlo realisations of submitted shear power spectrum where  $\sigma_{\text{sys}}^2$  is the denominator in equation (24), and the calculated bias in dark energy parameter with respect to its error.

(2012, in prep). The factor of 1000 normalises the metric such that a good method should achieve  $Q \simeq 1000$ . A factor  $(1/2\pi)$  could be included in the denominator, but we absorb this into the factor  $5 \times 10^{-6}$ . This was the quality factor used in the online leaderboard during the challenge.

## B2. Pixel noise corrected quality factor

In general we can express the measured total ellipticity by including a noise term in equation (11), where  $e_n$  is some inaccuracy in this estimator due to stochastic terms in shape measurement method, or due to pixel noise in the images (finite signal-to-noise). In the simulations, for ellipticity catalogue submissions, we averaged over  $N_{\text{realisation}}$  realisations of the noise. In this averaging the mean of the noise contribution is assumed to be zero  $\langle e_n \rangle = 0$  over realisations, but where there is an error on this mean that remains. By propagating this through to the power spectrum we recover

$$\tilde{C}_\ell^{EE} \rightarrow \tilde{C}_\ell^{EE} + \frac{\sigma_n^2}{N_{\text{realisation}} N_{\text{object}}} \quad (25)$$

where the noise term is white noise (constant over all scales) with a variance  $\sigma_n^2$ , which is a sum of the  $e_1$  and  $e_2$  components. The noise term is now averaged over the number of realisations and the number of objects. For values of  $N_{\text{realisation}} = 200$  and  $N_{\text{object}} = 10^4$  the expected fractional contribution to the measured power  $\sigma_n^2 / (N_{\text{realisation}} N_{\text{object}} \langle C_{\ell, \text{estimated}} \rangle) \approx (\sigma/0.05)^2$ .

The measured power spectra inferred from the ellipticity catalogue submissions and used in the quality factor ( $Q$ ) defined in equation (24), therefore includes this noise term. However for an error induced by noise on ellipticity estimates of  $\sigma \lesssim 0.05$  the impact on the metric should be subdominant. It is commonly assumed that such noise terms could be removed in real data (this is trivial for correlation functions, but is more complex for power spectrum estimates; that require an estimate of  $\sigma_n$  from data – the full covariance of the shear estimators, see also e.g. Schneider et al. 2010), and some power spectrum submissions (see Section 6) did employ techniques to remove this term from the submitted power spectrum. Hence we here introduce a quality factor that accounts for this noise term

$$Q_{\text{dn}} = 1000 \frac{5 \times 10^{-6}}{\int d \ln l |\tilde{C}_\ell^{EE} - C_\ell^{EE, \gamma\gamma} - \frac{\langle \sigma_n^2 \rangle}{N_{\text{realisation}} N_{\text{object}}}| l^2} \quad (26)$$

where  $\langle \sigma_n^2 \rangle$  is an estimated value of the pixel noise term from the ellipticity catalogue submissions.

To estimate the value of  $\langle \sigma_n^2 \rangle$  from the simulations we have to separate the E-mode shear field from the B-mode only intrinsic ellipticity field, otherwise the variance of the ellipticities from a submitted entry will be dominated by the variance of the intrinsic ellipticities. This is done using the rotations described in Appendix A, here we describe this pedagogically (we also use explicit Cartesian coordinates  $\boldsymbol{\theta} = (x, y)$  and  $\boldsymbol{\ell} = (\ell_x, \ell_y)$  for clarity). We make a 2D discrete Fourier transform of the submitted ellipticity values such that

$$\epsilon_{\text{measure}}(\ell_x, \ell_y) = \text{FT}[e_{\text{measure}}(x, y)] \quad (27)$$

where here the measured ellipticity is averaged over all noise realisations before transformation. We then rotate this field such that

$$\epsilon_{\text{rot,measure}}(\ell_x, \ell_y) = (\ell^* \ell^* / |\ell|^2) \epsilon_{\text{measure}}(\ell_x, \ell_y) \quad (28)$$

and then inverse Fourier transform to real space

$$\kappa(x, y) + i\beta(x, y) = \text{iFT}[\epsilon_{\text{rot,measure}}(\ell_x, \ell_y)] \quad (29)$$

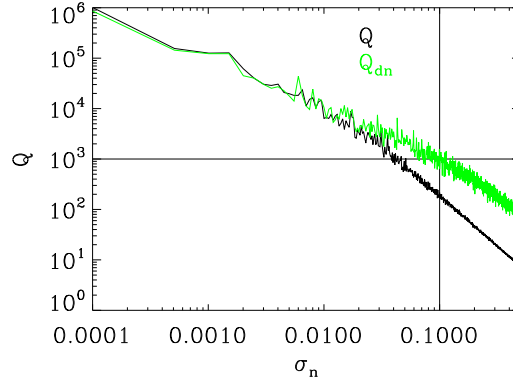


**Figure 12.** A simulation of the effect on  $Q$  (black line) and  $Q_{\text{dn}}$  (green line) as the noise in a mock submission (containing only noise and the true shear values) increases. Lines at  $Q = 1000$  and  $\sigma_n = 0.1$  are to guide the reader.

where we now have a  $\kappa(x, y)$  field which contains E-mode power only and a  $\beta(x, y)$  field that contains B-mode power only. The simulations have been set up such that the intrinsic ellipticity field has B-mode power only, such that we can now take the  $\kappa(x, y)$  map and generate an E-mode only ellipticity catalogue that should only contain the estimated shear values and the noise term only

$$\kappa(x, y) \rightarrow e_{\text{E,measure}}(x, y) \approx \hat{\gamma}(x, y) + e_n(x, y), \quad (30)$$

where  $\hat{\gamma}$  is the estimate shear for each position (object) in field. We do this by following the inverse steps of transformations from equations (27) to (29), and assume noise is equally distributed between E and B modes. The expression is only approximate because of position dependent biases (see Appendix A and next Section), that can mix E and B modes, but for the majority of methods presented in this paper this affect seems to be subdominant. By taking the normal variance of  $e_{\text{E,measure}}(x, y)$  we find that

$$\sigma_{\text{E,measure}}^2 = \sigma_\gamma^2 + \sigma_n^2 \quad (31)$$

and so our estimate of the noise variance is

$$\sigma_n^2 = \sigma_{\text{E,measure}}^2 - \sigma_\gamma^2. \quad (32)$$

To calculate this we use the true shear values to find  $\sigma_\gamma^2$  (but note that the true individual shear values are not used directly).

To test that such a correction works we simulated a submission by taking the true shear values and adding random normally distributed numbers to each of the  $10,000 \times 200 \times 24$  shear values. We show results in Figure 12. We find as expected that as the noise increases the value of  $Q$  (equation 24) decreases, but that including the noise correction (equation 26) increases the value. Note that due to the finite size of the simulations any estimation of  $\sigma_n^2$  is itself noisy which means the corrected value of  $Q_{\text{dn}} < \infty$  even in this ideal case.

### B3. One-point estimator shear relations

As well as metrics that integrate over the measured power spectra we can also investigate a number of metrics that encapsulate a relation between the measured and true shears for individual objects. This ties the quality factor metrics to the STEP (Heymans et al., 2006)  $m$  and  $c$  values where

$$\hat{\gamma}_i = (1 + m_{ij})\gamma_j^t + c_i \quad (33)$$

where  $\gamma_i^t$  is the true shear and  $\hat{\gamma}_i$  is the measured shear for each component, this is a simplification of equation (11), and that used for all constant shear simulations (with no position dependence). We also add a quadratic non-linear term to this relation ( $q_{ij}^{1/2}\gamma_j|\gamma|q_{ki}^{1/2}$ )

$$\hat{\gamma}_i = (1 + m_{ij})\gamma_j^t + c_i + q_{ij}^{1/2}\gamma_j|\gamma|q_{ki}^{1/2} \quad (34)$$

that contains  $\gamma|\gamma|$ , not  $\gamma^2$ , since we may expect divergent behaviour to more positive and more negative shear values for each domain respectively. In general  $m_{ij}$  and  $q_{ij}$  could be non-diagonal matrices, however in this paper we assume that they are diagonal and take an average over the two shear components to give

$$\hat{\gamma} = (1 + m)\gamma^t + c + q\gamma|\gamma| \quad (35)$$

where all quantities are averaged over  $\gamma_1$  and  $\gamma_2$ .

In a variable shear simulation calculating  $m$ ,  $c$  and  $q$  by regressing  $e_{\text{measure}}$  and  $(\gamma + e_{\text{intrinsic}})$  would result in a noisy estimator dominated by intrinsic ellipticity noise. However we can calculate  $m$ ,  $c$  and  $q$  directly by finding the estimated shear for each galaxy individually, removing the intrinsic ellipticity contribution (equation

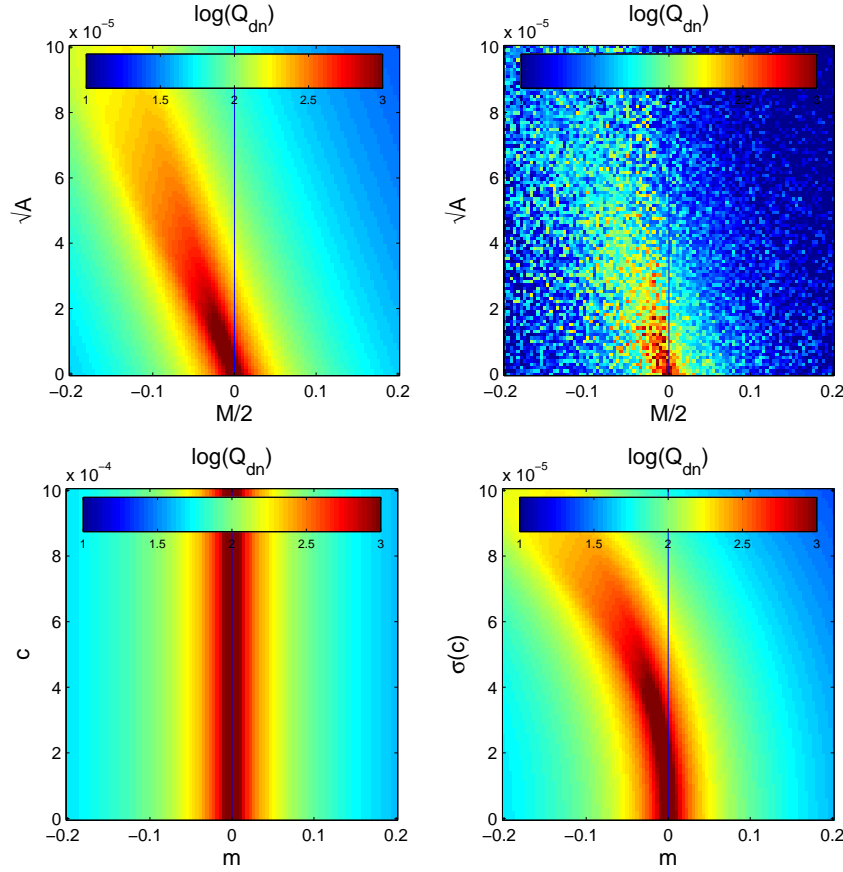


**Figure 13.** An exploration of the  $(\mathcal{M}, \mathcal{A})$ ,  $(m, c)$  and  $(m, \sigma(c))$  planes, where at each point the quality factor is calculated using a noise free fiducial power spectrum. The colour scale shows the logarithm of the quality factor. This can be compared to Figure 2.

30). This is for every galaxy a noisy estimate of the shear, we then average these estimates over bins in  $\gamma^t$ . This enables the  $m$ ,  $c$  and  $q$  parameters to be recovered, and in fact the variable field simulations allows for a flexible binning as a function of any other spatially varying quantity (see Appendix E), and an exact removal of shape noise (through the B-mode intrinsic power). This method of calculating the  $m$ ,  $c$  and  $q$  parameters is a one-point estimate of the shape measurement biases and makes no assumption about spatially correlated effects.

#### B4. Power spectrum relations

As described in Appendix A we can write an expression for the estimated power using two linear parameters  $\bar{\mathcal{M}}$  and  $\bar{\mathcal{A}}$ , taking into account the pixel noise removal we have a similar expression

$$\left[ C_\ell^{EE} - C_\ell^{EE, \gamma\gamma} - \frac{\langle \sigma_n^2 \rangle}{N_{\text{realisation}} N_{\text{object}}} \right] = \bar{\mathcal{M}} C_\ell^{EE, \gamma\gamma} + \bar{\mathcal{A}}. \quad (36)$$

This can be related to the  $m$  and  $c$  parameters

$$\begin{aligned} \bar{\mathcal{M}} &\simeq m^2 + 2m \approx 2m \\ \bar{\mathcal{A}} &\simeq \sigma(c)^2 \end{aligned} \quad (37)$$

where  $\sigma(c)$  is the variance of the  $c$  parameter, but only approximately because of the assumption of some form of spatial variation (constant in this case).

In Figure 13 we show how the  $Q_{\text{dn}}$ ,  $\mathcal{M}$ ,  $\mathcal{A}$  and the point estimators  $m$  and  $c$  are related. To create this we explore the  $(\mathcal{M}, \mathcal{A})$  plane and using the fiducial power spectrum calculate  $Q_{\text{dn}}$  for each value. We also show a realisation where random components have been added,  $\mathcal{M}(1 + R)$  where  $R$  is a uniform random number and similarly for  $\mathcal{A}$ , at each point in parameter space to simulate a more realistic submission. We find that there is degenerate line in  $Q_{\text{dn}}$  where an offset  $\mathcal{A}$  can be partially cancelled by a negative  $\mathcal{M}$  yielding the same  $Q_{\text{dn}}$ , and a more straightforward relation for  $\mathcal{M} \geq 0$ . As expected the  $c$  parameter does not impact the quality factor but the variance of  $c$  does. There is a similar degeneracy between  $m$ ,  $\sigma(c)$  and  $Q_{\text{dn}}$  as with the linear power spectrum parameters, this is as expected as in equation (37), except that for large negative  $m$  the quadratic  $m^2$  term begins to become important.

### B5. Correlations with spatially varying quantities

To relax the assumption of constant  $m$  and  $c$  in power spectrum analysis we can assume that each of these is correlated with some spatially varying parameter  $X(\boldsymbol{\theta})$

$$\begin{aligned} m(\boldsymbol{\theta}) &= m_0 + \alpha X(\boldsymbol{\theta}) \\ c(\boldsymbol{\theta}) &= c_0 + \beta X(\boldsymbol{\theta}) \end{aligned} \quad (38)$$

with correlation coefficients  $\alpha$  and  $\beta$ . This is a simple relation and could be made significantly more complex.

We explain in a correlation function notation how these propagate through, for pedagogical purposes, but for the full treatment one should refer to the pseudo-Cl methodology that we present in Appendix A. A simple correlation function approximation of the measured shear can be written

$$\begin{aligned} \langle \langle e_{\text{measure}} \rangle_n \langle e_{\text{measure}} \rangle_n^* \rangle &= \alpha^2 \langle XX^* \rangle [\langle \gamma \gamma^* \rangle + \langle \langle e_{\text{intrinsic}} \rangle_n \langle e_{\text{intrinsic}} \rangle_n^* \rangle] \\ &+ (2(1 + m_0)\alpha \langle X \rangle + (1 + m_0)^2) [\langle \gamma \gamma^* \rangle + \langle \langle e_{\text{intrinsic}} \rangle_n \langle e_{\text{intrinsic}} \rangle_n^* \rangle] + \beta^2 \langle XX^* \rangle \end{aligned} \quad (39)$$

not including the pixel noise term. We can also take the cross correlation between the measured ellipticity and these quantities

$$\begin{aligned} \langle \langle e_{\text{measure}} \rangle_n X^* \rangle &= \langle ((1 + m_0 + \alpha X)(\gamma + \langle e_{\text{intrinsic}} \rangle_n) + c_0 + \beta X) X^* \rangle \\ &= (1 + m_0) \langle (\gamma + \langle e_{\text{intrinsic}} \rangle_n) X^* \rangle + \alpha \langle X(\gamma + \langle e_{\text{intrinsic}} \rangle_n) X^* \rangle + \beta \langle XX^* \rangle + c_0 \langle X^* \rangle \\ &\approx (1 + m_0) \langle (\gamma + \langle e_{\text{intrinsic}} \rangle_n) X^* \rangle + \beta \langle XX^* \rangle + c_0 \langle X^* \rangle \end{aligned} \quad (40)$$

which results in an expression that is not dependent on  $\alpha$  and assuming that third order correlations and noise- $X$  correlations are zero.

The corresponding full expressions for the pseudo-Cl power spectrum, including the noise correction term (which we assume is uncorrelated with all other terms) are

$$\begin{aligned} \left[ \tilde{C}_\ell^{EE} - C_\ell^{EE, \gamma\gamma} - \frac{\langle \sigma_n^2 \rangle}{N_{\text{realisation}} N_{\text{object}}} \right] &= (m_\ell^2 + 2m_\ell) C_\ell^{EE, \gamma\gamma} + \alpha^2 \sum_{\ell'} [M_{\ell\ell'}^{EE, XX} C_{\ell'}^{EE, \gamma\gamma} + M_{\ell\ell'}^{BB, XX} C_{\ell'}^{BB, II}] \\ &+ \alpha(1 + m_\ell) \langle X \rangle C_\ell^{EE, \gamma\gamma} + \beta^2 C_\ell^{XX} \\ [\tilde{C}_\ell^{EX} - C_\ell^{\gamma X} - C_\ell^{IX}] &= m_\ell (C_\ell^{\gamma X} + C_\ell^{IX}) + \beta C_\ell^{XX} + c_0 \langle X_\ell \rangle. \end{aligned} \quad (41)$$

The second expression has cross-power spectra on the both sides. The matrices  $M^{XX}$  are the mixing matrices for the spatially varying quantity  $X$ . In general the variation of  $X$  is not isotropic – PSF ellipticity for example can have a preferred direction in an image – however here we make the assumption of isotropy in defining the power  $C_\ell^{XX}$ .

To calculate these from the simulations we find the best fitting  $\alpha$  and  $\beta$  values (using a minimum least squares estimator over the  $\ell$  range defined in Section 6) for  $X = \text{PSF size squared}$  and  $\text{PSF ellipticity}$ . Because this calculation is done on sets that are averaged over noise realisations this can only be calculated for those sets in which the PSF is fixed for a set (for the PSF correlations).

The relation to the linear power relations  $\mathcal{M}$  and  $\mathcal{A}$  is not straightforward because of the non-diagonal mixing matrix in general. Therefore in the results Sections (Section 4) we will quote values for these correlation coefficients  $\alpha_e$ ,  $\alpha_{R^2}$ ,  $\beta_e$ ,  $\beta_{R^2}$  for ellipticity and PSF size squared (the square of the size is the most relevant quantity for propagated PSF-shear behaviour, see Massey et al. 2012, in prep and Paulin-Henriksson et al. 2008). Note that  $\alpha$  and  $\beta$  have scaled units of  $[\langle X \rangle]^{-1}$ , for PSF size correlations this means units of  $(1/3.4)\text{pixel}^{-1}$  and for ellipticity correlations the quantities are unitless.

## APPENDIX C : SIMULATION MODELLING

In this Section we provide some further details of the variable shear and PSF field, as well as the local modelling of the galaxies and stars.

### C1. Scaling of the shear field

We note that in performing the process of sampling the shear field discretely and then generating a postage stamp for each sampling the inter-postage stamp separation in the final image has a distance of  $\theta_{\text{image}}/100$  but this is not necessarily related to the pixel scale of the postage stamps i.e.  $\theta_{\text{pixel}} \times 48 \times 100 \neq \theta_{\text{image}}$  in general. As a result the number density of the galaxies can be scaled as

$$\frac{n_0}{\text{square arcmin}} = \frac{10^4}{3600\theta_{\text{image}}^2} = \frac{2.77}{\theta_{\text{image}}^2} \quad (42)$$

and the maximum  $\ell$  set by the grid-separation of the galaxies scales as

$$\ell_{\text{max}} = 0.5 \frac{2}{\theta_{\text{image}}^2/180/100} = \frac{18,000}{\theta_{\text{image}}} \quad (43)$$

where 100 is the number of grid positions on a side. But note that the true underlying simulated shear field is always fully sampled in every case.

For the case of  $\theta_{\text{image}} = 10$  degrees this gives values of  $n_0 = 0.0277$  and  $\ell_{\text{max}} = 1800$ . The images however can be scaled to match a variety of other configurations, with the caveat that the absolute value of the shear power is constant,  $\theta_{\text{image}} = 1$  degrees gives a scaling of  $n_0 = 2.77$  and  $\ell_{\text{max}} = 18,000$ , and  $\theta_{\text{image}} = 0.5$  degrees gives a scaling of  $n_0 = 11.1$  and  $\ell_{\text{max}} = 36,000$ . In each case the absolute amplitude of the calculated shear power also needs to be scaled. It is fair to then match the simulations to either of these cases, which span a reasonable expected dynamical range in number density of objects but with a coupled increase in the maximum  $\ell$ -range.

## C2. The galaxy models

Here we describe how the individual galaxies are modelled. Each galaxy is composed of a bulge and a disk defined as radial intensity profiles with

$$I(r) = I_i \exp \left[ - \left( K \frac{r}{r_i} \right)^{1/n} \right] \quad (44)$$

where  $K = 2n - 0.331$  with  $n = 4$  for the bulge and  $n = 1$  for the disks and  $i = \{b, d\}$  for bulge and disk. Both are Sersic profiles (the second simply a exponential). The intensity is normalised to match the signal-to-noise and the scale radii for the disk and bulge,  $r_d$  and  $r_b$  respectively, are in general free parameters, fiducial values these were set to be  $r_b = 2.3$  and  $r_d = 4.8$  pixels. In Bridle et al. (2010), and for the code used for this challenge, the value of radii  $r$  are the half-light radius for both bulges and disks. The disk exponential scale length and half-light scale radii differ by that factor 1.669.

In most sets the size distribution over objects was a compact Gaussian, with a variance of  $\sigma_R = 0.01$

$$p(r) \propto \exp \left[ - \frac{(r - r_b)^2}{2\sigma_R^2} \right]. \quad (45)$$

and similarly for the disk distribution. In three sets (see Section 3.1) the galaxy size varied for each galaxy in the set, in this case the functional form for the signal-to-noise variation was a Rayleigh distribution

$$P(r) \propto \frac{r}{\sigma_R^2} \exp \left[ - \frac{(r - r_b)^2}{\sigma_R^2} \right], \quad (46)$$

where  $\sigma_R = 2.0$  for these sets, and the  $r_b$  and  $r_d$  are the fiducial values. There is a caveat that the sizes referred to here (and in the GREAT08 simulations) refer to the *pre-sheared* radii of the objects, as such there is a ellipticity-size correlation that was present in the simulations.

The bulge and disk in general can be mis-centered, however in all but two sets the bulge and disk profiles were co-centered. Object positions were centered in each postage stamp with a Gaussian error position with a standard deviation of 0.5 pixels.

The bulge-to-disk fraction was 50% for the majority of sets i.e. the flux in the bulge and disk was equal. In those sets in which this varied we used a uniform distribution of bulge-to-disk ratios over the range  $b/d = [0.3, 0.95]$ , to avoid very low and very high fractions.

The bulge and disk components of the galaxies in the simulations had different intrinsic ellipticity distributions, each described by

$$P_i(e) = e \cos \left( \frac{\pi e}{2} \right) \exp \left[ -2 \left( \frac{e}{B_i} \right)^C \right] \quad (47)$$

where  $B = 0.09$  and  $C = 0.577$  for the bulges and  $B = 0.19$  and  $C = 0.702$  for the disks (these values are taken from the APM survey, Crittenden et al. 2001). To remove any very highly elliptical galaxies from the sample we truncated this distribution at  $e = 0.8$ . This model was slightly more complex than in Bridle et al. (2010) by allowing for non-coelliptical profiles (i.e. the bulge and disk were allowed to have different ellipticities). This was done so that the ellipticity distributions in equation (47) were conserved. As an example we show the distribution of the disk and bulge angles in Figure 14.

The signal-to-noise was implemented by calculating the noise-free model flux by integrating over the galaxy model and then adding a constant Gaussian noise with a variance of unity and rescaling the galaxy model to yield the correct signal-to-noise. The signal-to-noise was scaled to match the default SExtractor (Bertin & Arnouts 1996) `flux_auto/flux_err_auto` parameter combination. The galaxy signal-to-noise distribution was a compact Gaussian in the majority of sets, with a variance of  $\sigma_S = 0.1$ , centered on  $(S/N)_i = 20$  for the fiducial set

$$p(S/N) \propto \exp \left[ - \frac{(S/N - (S/N)_i)^2}{2\sigma_S^2} \right]. \quad (48)$$

In three sets (see Section 3.1) the signal to noise varied for each galaxy in the set with a functional form for the signal-to-noise variation that was a Rayleigh distribution

$$P(S/N) \propto \frac{S/N}{\sigma_S^2} \exp \left[ - \frac{(S/N - (S/N)_i)^2}{\sigma_S^2} \right], \quad (49)$$

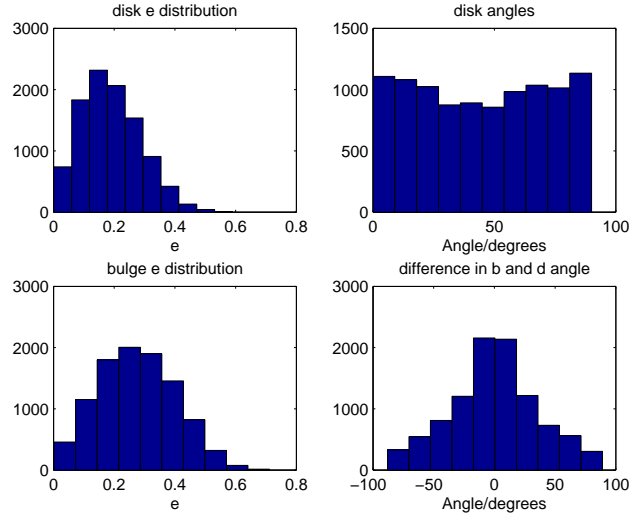


**Figure 14.** The distributions of bulge and disk ellipticities for a typical image within the fiducial set. Left panels show the distribution of ellipticities for bulge and disk. The top right panel shows the uniform distribution of disk position angles, and the bottom right panel shows the difference between the bulge and disk positions angles.

where  $(S/N)_i = 20$  and  $\sigma_S = 5.0$  for these sets.

### C3. The PSF models

The PSF model consisted of a static component that modelled the local PSF functional form and a spatially varying kernel that mapped the parameters of this local model across the image plane. The local functional form was a Moffat profile

$$I(r) = \left[ 1 + \left( \frac{r}{r_d} \right)^2 \right]^{-\beta}, \quad (50)$$

the scale radius  $r_d$  was a variable quantity across each image, related to the FWHM, the power  $\beta = 3$  for all images. After generating a circular PSF, it was made into an elliptical shape by distortion using the shear matrix given in Kitching et al. (2011) such that there were three parameters which locally describe the PSF ( $r_d, e_1, e_2$ ). Where similarly to the galaxies the size was the *pre-sheared* size of the PSF.

The PSF spatial variation consisted of three components

- **Static Component.** These were spatially constant across the image and consisted of i) a Gaussian smoothing kernel that added to the PSF size, this had a variance of 0.1 present in all images, ii) a static additive ellipticity component of 0.05 in  $e_{1,\text{PSF}}$  and  $e_{2,\text{PSF}}$  to simulate tracking error.

- **Deterministic Component.** This was to simulate the impact of the telescope on the PSF size and ellipticity. We used the Jarvis, Schecter and Jain (2008) model to simulate this with fiducial parameters ( $a_0 = 0.014$ ,  $a_1 = 0.0005$ ,  $d_0 = -0.006$ ,  $d_1 = 0.001$ ,  $c_0 = -0.010$ ), which is dominated by primary astigmatism ( $a_0$ ), primary de-focus ( $d_0$ ) and coma ( $c_0$ ).

- **Random Component.** To simulate the random turbulent effect of the atmosphere in some of the sets we additionally included a random Gaussian field in the ellipticity only with a Kolmogorov power spectrum of  $C_\ell = \ell^{-11/6}$  (see Rowe, 2010 and Heymans et al., 2012 for discussion on this kind of power spectrum PSF variation seen in optical weak lensing images).

In Figure 15 we show a typical PSF pattern for an image in a set with no random Kolmogorov variation and one in which there is a random Kolmogorov component. As described in Section 2 participants were provided with the PSF as an exact functional form, consisting of tabulated numbers for  $(r_d, e_1, e_2)$  at the position of each galaxy and as a pixelated stellar image.

## APPENDIX D : SET DESCRIPTION

In the Table below we provide the parameter values that define each set in the GREAT10 Galaxy Challenge simulations.



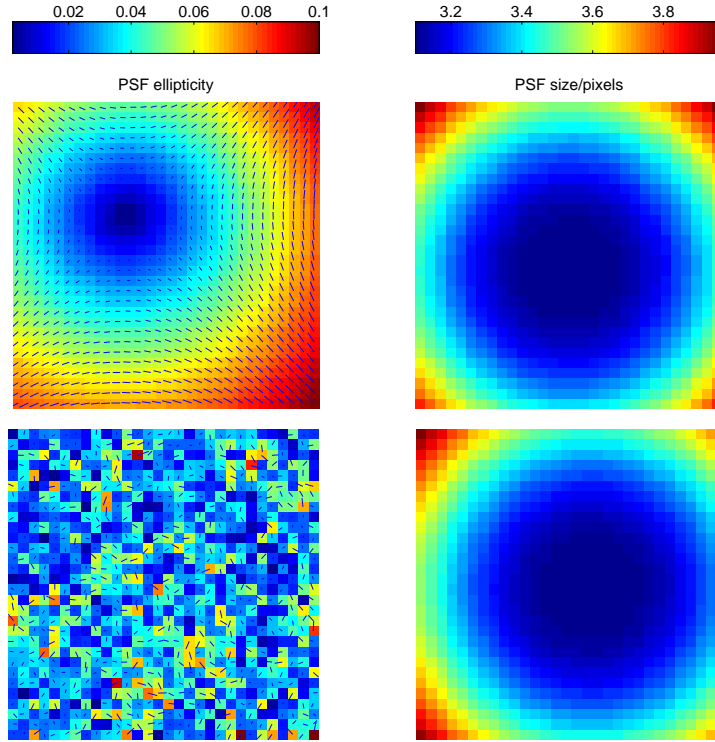


**Figure 15.** Each panel shows an entire simulated image, showing the typical PSF pattern for an image in a set (image 100 in set 1) with no random Kolmogorov component (upper panels) and for an image in a set (image 100 in set 19) with a random Kolmogorov component (lower panels). The 100x100 grid has been downsampled to 30x30 in these panels for clarity. The left panels show the amplitude of the ellipticity in the colour scale, and the orientation of the PSF denoted by the whiskers. The right hand panels show the size of the PSF in the colour scale in unit of pixels. In each image in a set these patterns changed, except in those sets where the PSF spatial variation was fixed (see Appendix D).

	Set Name	Fixed	S/N	S/N Dist.	$r_b/\text{pix.}$	$r_d/\text{pix.}$	B/D Fraction	B-D Offset/pix. <sup>2</sup>	$r$ Dist.	KM Power
1	Fiducial	–	20	Gaussian	2.3	4.8	0.5	0.0	Gaussian	None
2	Fiducial	<b>PSF</b>	20	Gaussian	2.3	4.8	0.5	0.0	Gaussian	None
3	Fiducial	<b>Int</b>	20	Gaussian	2.3	4.8	0.5	0.0	Gaussian	None
4	Low S/N	–	<b>10</b>	Gaussian	2.3	4.8	0.5	0.0	Gaussian	None
5	Low S/N	<b>PSF</b>	<b>10</b>	Gaussian	2.3	4.8	0.5	0.0	Gaussian	None
6	Low S/N	<b>Int</b>	<b>10</b>	Gaussian	2.3	4.8	0.5	0.0	Gaussian	None
7	High S/N	–	<b>40</b>	Gaussian	2.3	4.8	0.5	0.0	Gaussian	None
8	High S/N	<b>PSF</b>	<b>40</b>	Gaussian	2.3	4.8	0.5	0.0	Gaussian	None
9	High S/N	<b>Int</b>	<b>40</b>	Gaussian	2.3	4.8	0.5	0.0	Gaussian	None
10	Smooth S/N	–	20	<b>Rayleigh</b>	2.3	4.8	0.5	0.0	Gaussian	None
11	Smooth S/N	<b>PSF</b>	20	<b>Rayleigh</b>	2.3	4.8	0.5	0.0	Gaussian	None
12	Smooth S/N	<b>Int</b>	20	<b>Rayleigh</b>	2.3	4.8	0.5	0.0	Gaussian	None
13	Small Galaxy	–	20	Gaussian	<b>1.8</b>	<b>2.6</b>	0.5	0.0	Gaussian	None
14	Small Galaxy	<b>PSF</b>	20	Gaussian	<b>1.8</b>	<b>2.6</b>	0.5	0.0	Gaussian	None
15	Large Galaxy	–	20	Gaussian	<b>3.4</b>	<b>10.0</b>	0.5	0.0	Gaussian	None
16	Large Galaxy	<b>PSF</b>	20	Gaussian	<b>3.4</b>	<b>10.0</b>	0.5	0.0	Gaussian	None
17	Smooth Galaxy	–	20	Gaussian	2.3	4.8	0.5	0.0	<b>Rayleigh</b>	None
18	Smooth Galaxy	<b>PSF</b>	20	Gaussian	2.3	4.8	0.5	0.0	<b>Rayleigh</b>	None
19	Kolmogorov	–	20	Gaussian	2.3	4.8	0.5	0.0	Gaussian	<b>Yes</b>
20	Kolmogorov	<b>PSF</b>	20	Gaussian	2.3	4.8	0.5	0.0	Gaussian	<b>Yes</b>
21	Uniform b/d	–	20	Gaussian	2.3	4.8	<b>[0.3, 0.95]</b>	0.0	Gaussian	None
22	Uniform b/d	<b>PSF</b>	20	Gaussian	2.3	4.8	<b>[0.3, 0.95]</b>	0.0	Gaussian	None
23	Offset b/d	–	20	Gaussian	2.3	4.8	0.5	<b>0.5</b>	Gaussian	None
24	Offset b/d	<b>PSF</b>	20	Gaussian	2.3	4.8	0.5	<b>0.5</b>	Gaussian	None

**Table 5.** A summary of the variables that define each set in the GREAT10 Galaxy Challenge simulations. The variables in bold are those that distinguish each set from the fiducial one. The third column lists those fields that were fixed over each image in each set. Columns 4 and 9 list the distribution used for the signal-to-noise and galaxy sizes respectively. Column 8 shows the variance of the offset between the bulge and disk components in pixels squared.

## APPENDIX E : DESCRIPTION OF THE METHODS

Here we briefly summarise the methods that took part in the challenge. We encourage the reader to refer to the methods' own papers for more details.

For each method we show 3 figures these are

- (i) A reconstruction of the shear power spectrum for each set comparing the submitted power, true power and pixel noise corrected power, and the  $\mathcal{M}$ ,  $\mathcal{A}$  and  $Q_{\text{dn}}$  values for all sets.
- (ii) The measured minus true shear on an object-by-object basis as a function of the true shear  $\gamma^t$ , the PSF ellipticity and size, the bulge-to-disk angle and fraction and the bulge size; for  $\gamma^t$  the gradient and offset of this fit is  $m$  and  $c$ , in all cases we make 10 bins the variable quantity. We also show a value for  $q$ , a non-linear shear response for each metric keeping  $m$  and  $c$  fixed at their best fit values (see equation 35).
- (iii) The  $m$  and  $c$  values as a function of PSF ellipticity and size, the bulge-to-disk angle and fraction and the bulge size. In all cases we make 10 bins the variable quantity.

Because these figures contain a wealth of information for the latter two we plot the gradient and offset values for a linear fit through the points and display these values in the figures. In the top righthand corner of each of the subplots we show the difference in the reduced  $\chi^2$  between the best linear fit and the best constant fit (gradient equal to zero)  $\Delta\chi^2 = \chi^2(\text{gradient, offset}) - \chi^2(\text{offset})$ ; this can be used as an indicator of the significance of any linearly varying behaviour.

For power spectrum submissions the later two plots (concerned with individual one-point shear biases) will not be shown.

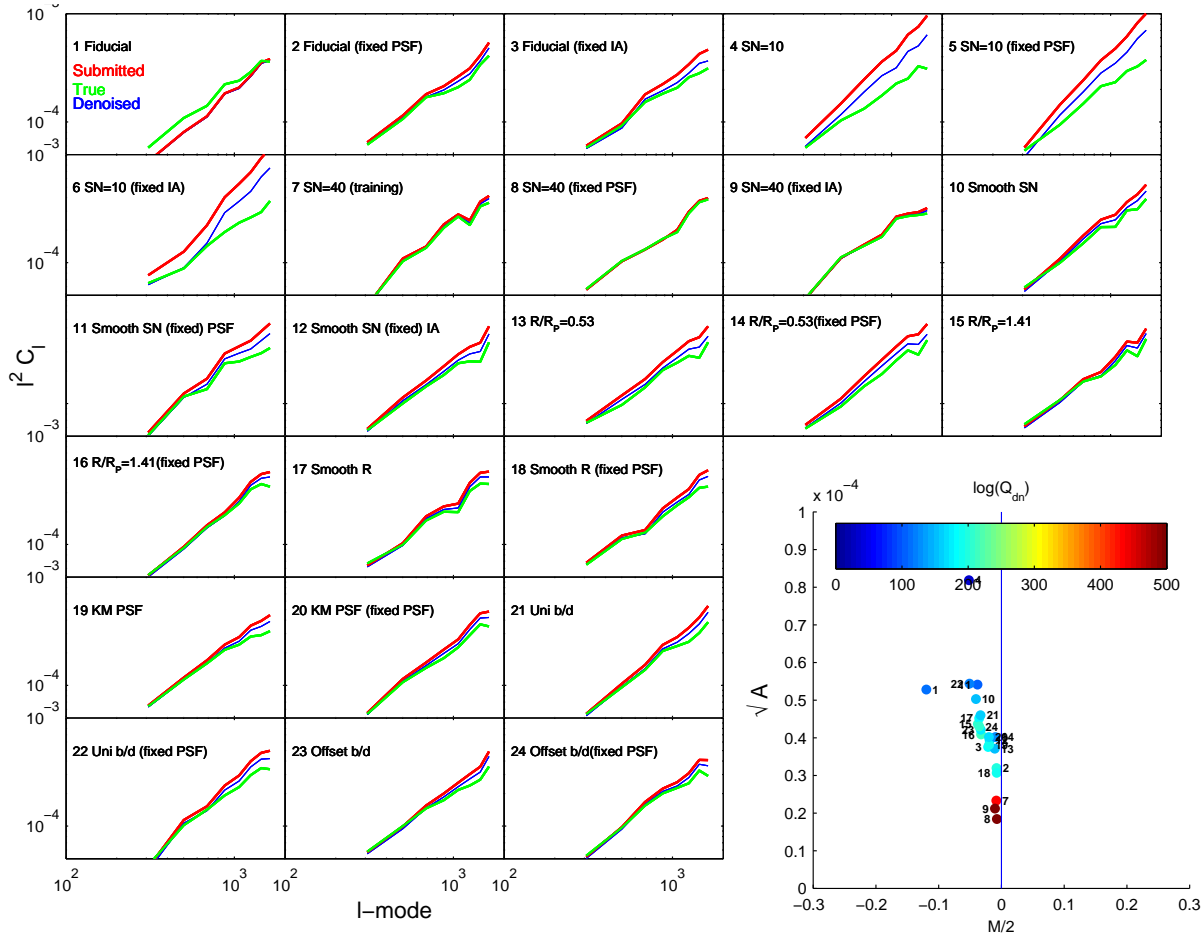


**Figure 16.** The true shear power (green) for each set and the shear power for the ‘ARES 50/50’ submission (red), we also show the ‘denoised’ power spectrum (blue) for each set (where this is indistinguishable from the raw submission a red line is only legible). The y-axes are  $C_\ell \ell^2$  and the x-axis is  $\ell$ . In the bottom righthand corner we show the  $\mathcal{M}/2$ ,  $\sqrt{A}$  and the colour scale represents the logarithm of the quality factor. The small numbers next to each point label the set number.

### E1. ARES : Peter Melchior

Comparing the results of DEIMOS and KSB, we found several sets where the ellipticities measured with either method strongly and consistently disagreed, with relative deviations of up to 25%. With additional simulations we investigated when such discrepancies between KSB and DEIMOS occur, and concluded that mainly very small, i.e. badly resolved, galaxies are responsible for large relative deviations, with KSB having a too weak and DEIMOS a too strong response to galactic ellipticities. Hence, a linear combination of the shear estimates of KSB and DEIMOS appeared advantageous. With the results of our simulations, a weighting scheme was defined that aims to minimise the mean squared error on the ellipticity of each galaxy. For GREAT10, the weight for each set was adjusted independently.

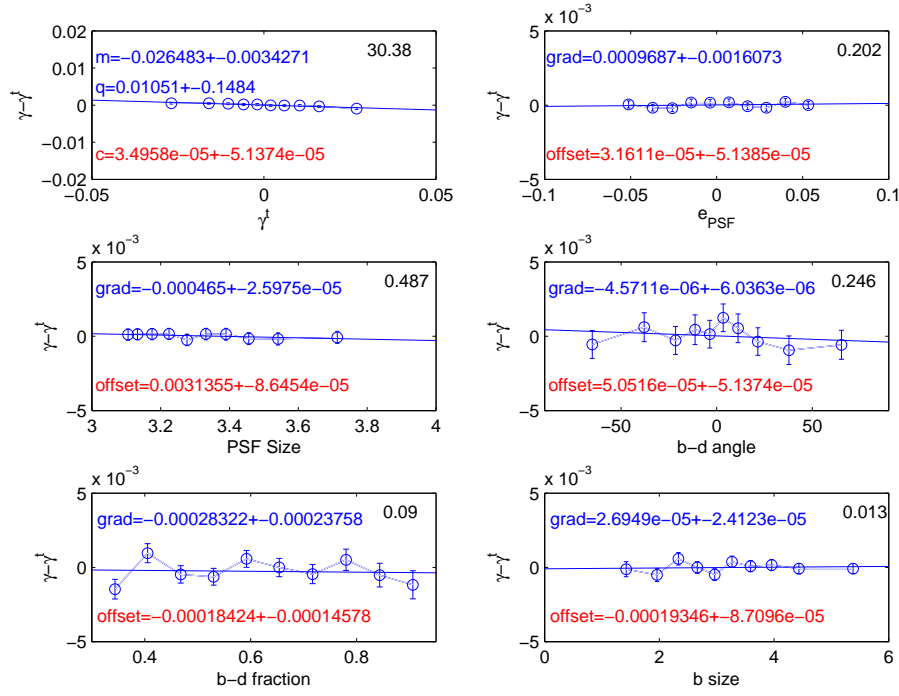


**Figure 17.** The measured minus true shear for the ‘ARES 50/50’ submission as a function of the true shear, PSF ellipticity, PSF FWHM, galaxy bulge-to-disk offset angle, galaxy bulge-to-disk fraction and galaxy bulge size. For each dependency we fit a linear function with a gradient and offset, for the top left hand panel this is the STEP  $m$  and  $c$  values, additionally for the shear dependency we include a quadratic term separately  $q$ . The top right hand corners show  $\Delta\chi^2 = \chi^2(\text{gradient, offset}) - \chi^2(\text{offset})$ .

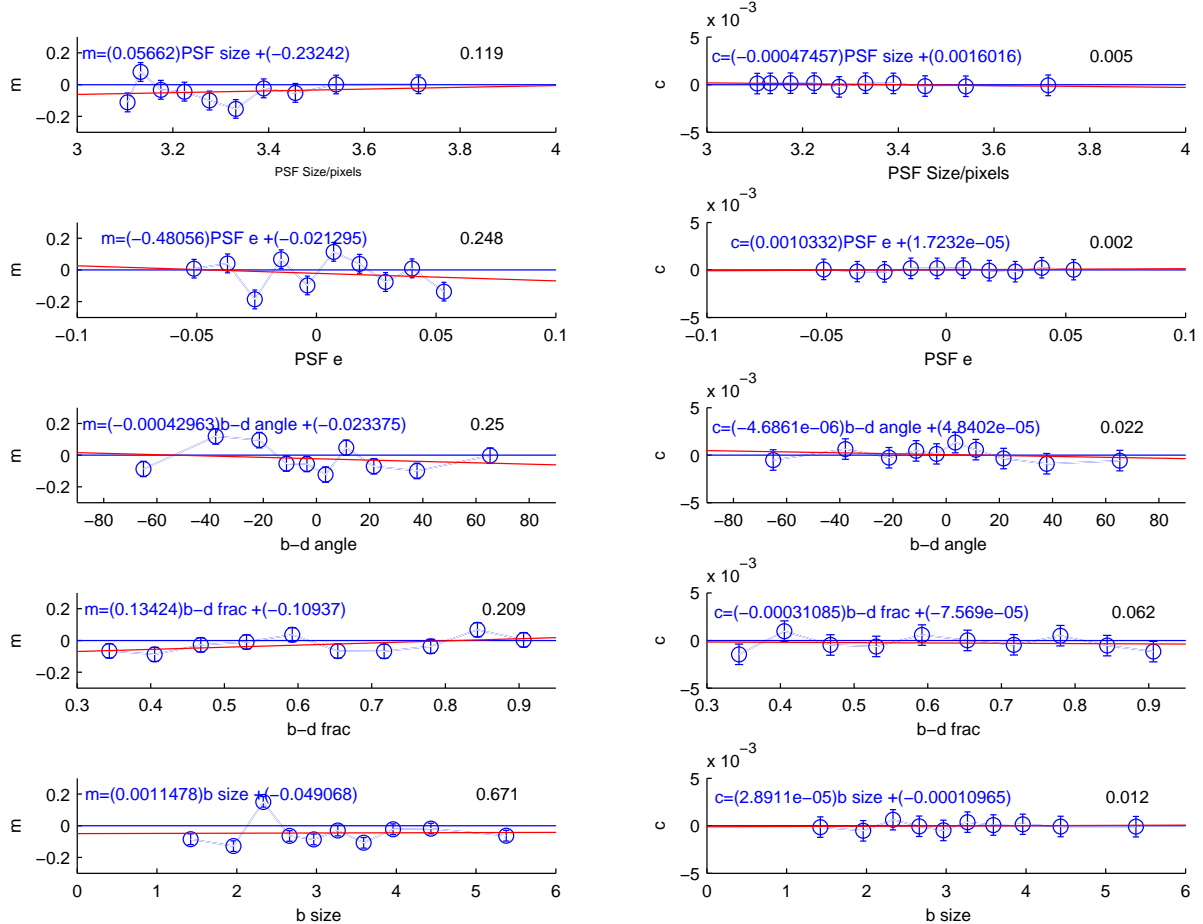


**Figure 18.** The STEP  $m$  and  $c$  values for the ‘ARES 50/50’ submission as a function of PSF FWHM and ellipticity, galaxy bulge-to-disk offset angle, galaxy bulge-to-disk fraction and galaxy bulge size. For each variable we plot the a linear relation to the behaviour of  $m$  and  $c$ . We do not explicitly quote errors on all parameters for clarity, the average errors on  $m$  and  $c$  are  $\simeq 0.005$  and  $5 \times 10^{-5}$  respectively. The top right hand corners show  $\Delta\chi^2 = \chi^2(\text{gradient, offset}) - \chi^2(\text{offset})$ .

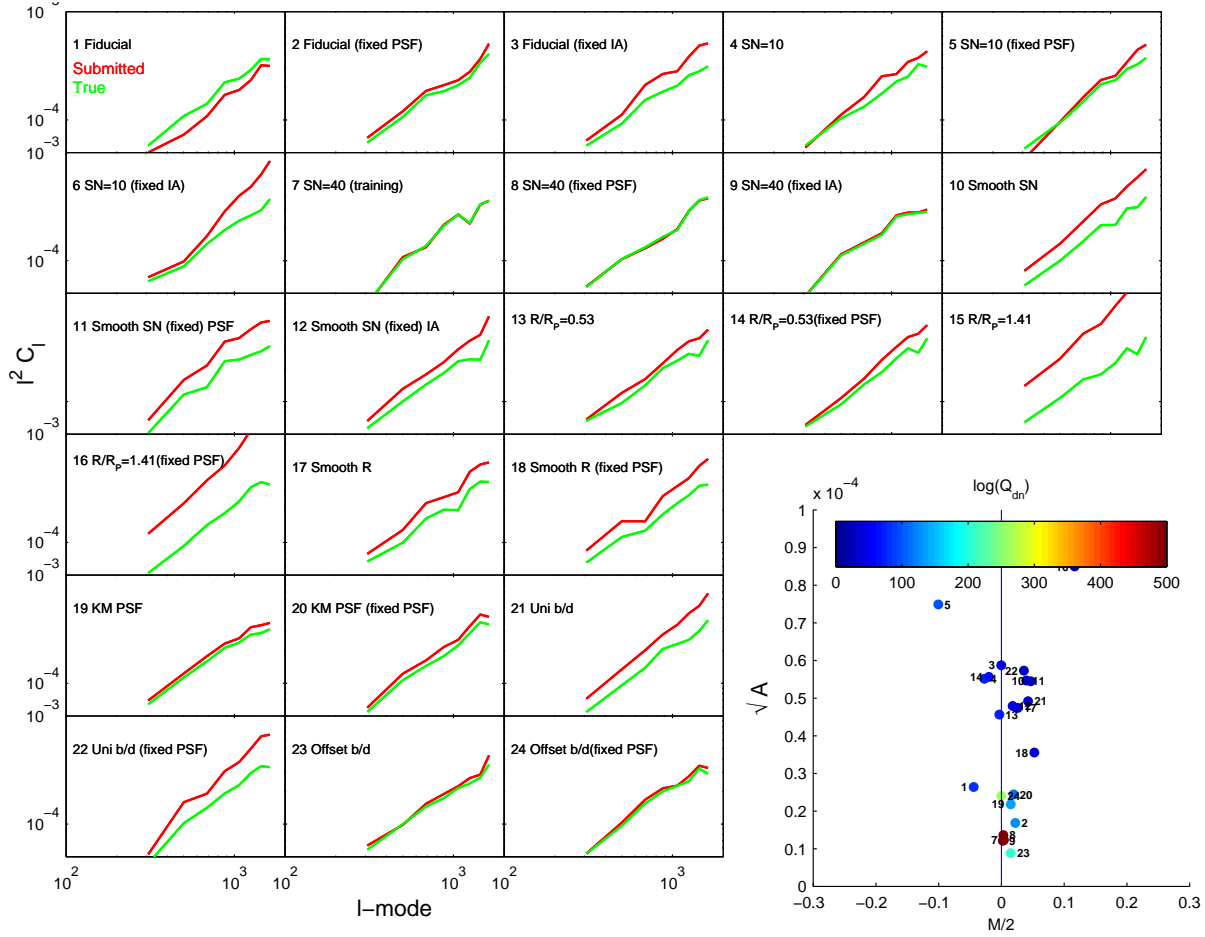


**Figure 19.** The true shear power (green) for each set and the shear power for the ‘cat2-unfold’ submission (red), we also show the ‘denoised’ power spectrum (blue) for each set (where this is indistinguishable from the raw submission a red line is only legible). The y-axes are  $C_\ell \ell^2$  and the x-axis is  $\ell$ . In the bottom righthand corner we show the  $M/2$ ,  $\sqrt{A}$  and the colour scale represents the logarithm of the quality factor. The small numbers next to each point label the set number.

## E2. cat-unfold: David Kirkby, Daniel Margala

See fit-unfold description.

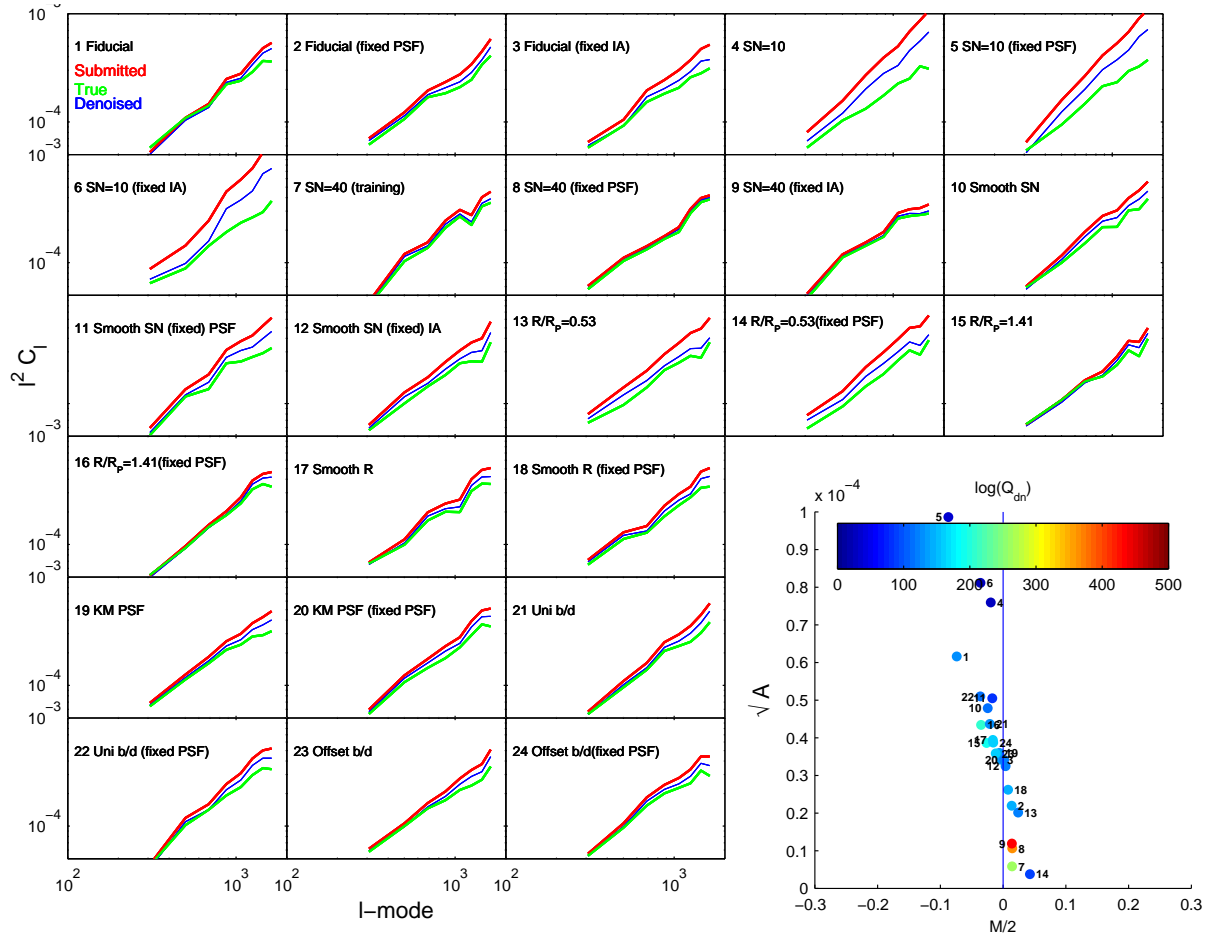


**Figure 20.** The true shear power (green) for each set and the shear power for the ‘DEIMOS C6’ submission (red), we also show the ‘denoised’ power spectrum (blue) for each set (where this is indistinguishable from the raw submission a red line is only legible). The y-axes are  $C_\ell \ell^2$  and the x-axis is  $\ell$ . In the bottom righthand corner we show the  $\mathcal{M}/2$ ,  $\sqrt{A}$  and the colour scale represents the logarithm of the quality factor. The small numbers next to each point label the set number.

### E3. DEIMOS : Peter Melchior, Massimo Viola, Julia Young, Kenneth Patton

DEIMOS (Melchior et al., 2011) measures the second-order moments of the light distribution using an elliptical Gaussian weight function, whose width is adjusted such as to maximise the S/N of the measurement. The centroid of the galaxy and ellipticity of the weight function is iteratively matched to the apparent (i.e. PSF-convolved) galaxy (the method has first been described by Bernstein & Jarvis, 2002). The application of the weight function to the image is then corrected by considering higher-order moments. These corrections become increasingly accurate with increasing width of the weight function, or the correction order. For GREAT10 we used correction order of 4 to 8, i.e. considering the effect of weighting on the moments of order 6 to 10. This correction scheme has been shown to introduce very small biases on the order of 1%, mostly for very small galaxies. After the deweighting, we deconvolve the galactic moments from the moments of the PSF, for which we have established an exact and analytic approach. The PSF has been measured with a weight function of the same width as the galaxy, but the ellipticity of the weight function was allowed to match the ellipticity of the PSF. From the deconvolved moments we determine the complex ellipticity  $\epsilon$ , which theoretically provides an unbiased estimator of the gravitational shear and thus does not need any susceptibility or responsivity corrections.

The only free parameter is the choice of the correction order, which we varied from 4 to 8 (e.g. “DEIMOS C6”), and the range of weight function widths. No model of either galaxy or PSF is employed. The pixel values are taken at center-pixel positions, an interpolation to sub-pixel resolution is not applied.

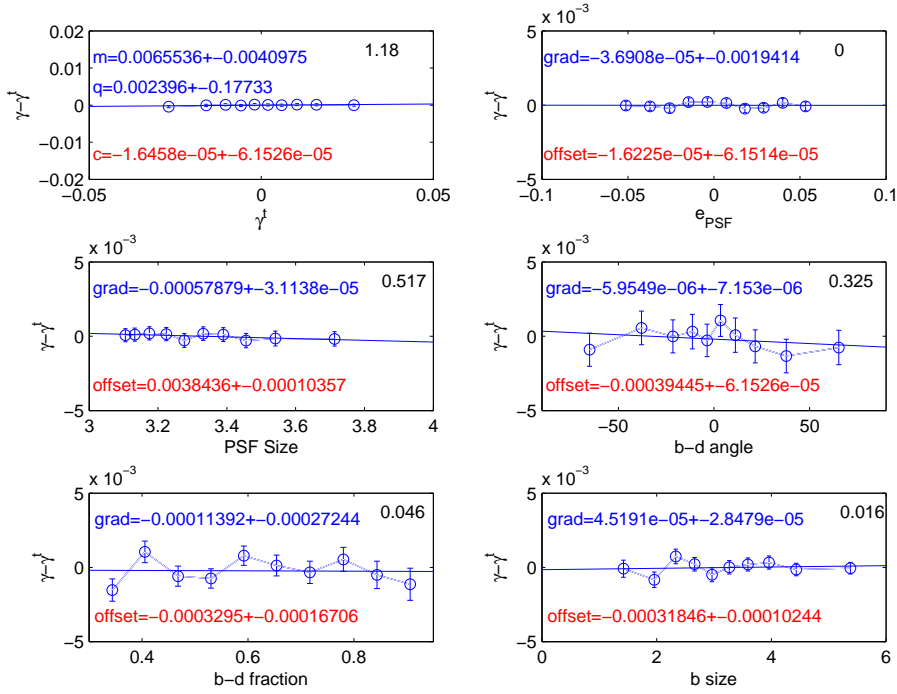


**Figure 21.** The measured minus true shear for the ‘DEIMOS C6’ submission as a function of the true shear, PSF ellipticity, PSF FWHM, galaxy bulge-to-disk offset angle, galaxy bulge-to-disk fraction and galaxy bulge size. For each dependency we fit a linear function with a gradient and offset, for the top left hand panel this is the STEP  $m$  and  $c$  values, additionally for the shear dependency we include a quadratic term separately  $q$ . The top right hand corners show  $\Delta\chi^2 = \chi^2(\text{gradient}, \text{offset}) - \chi^2(\text{offset})$ .

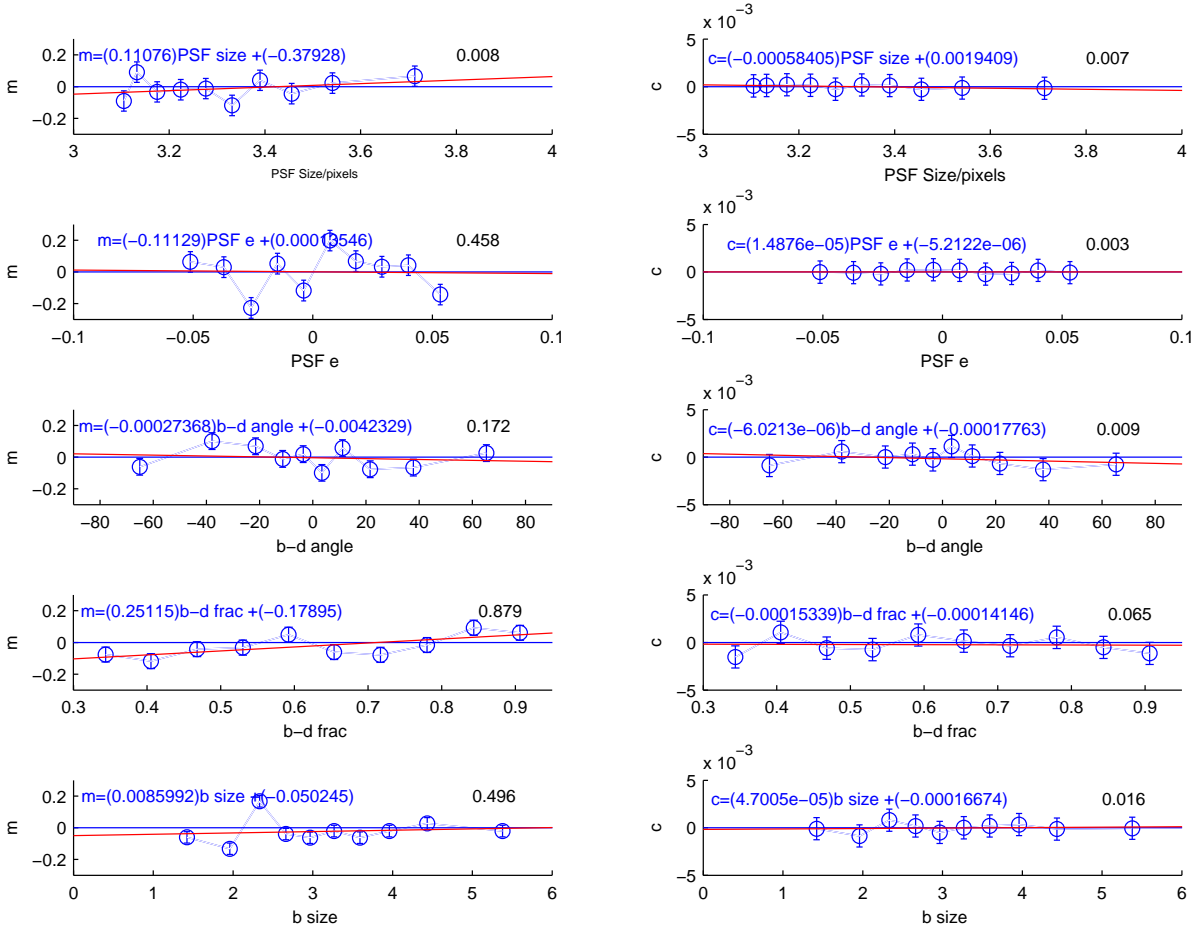


**Figure 22.** The STEP  $m$  and  $c$  values for the ‘DEIMOS C6’ submission as a function of PSF FWHM and ellipticity, galaxy bulge-to-disk offset angle, galaxy bulge-to-disk fraction and galaxy bulge size. For each variable we plot the a linear relation to the behaviour of  $m$  and  $c$ . We do not explicitly quote errors on all parameters for clarity, the average errors on  $m$  and  $c$  are  $\simeq 0.005$  and  $5 \times 10^{-5}$  respectively. The top right hand corners show  $\Delta\chi^2 = \chi^2(\text{gradient}, \text{offset}) - \chi^2(\text{offset})$ .



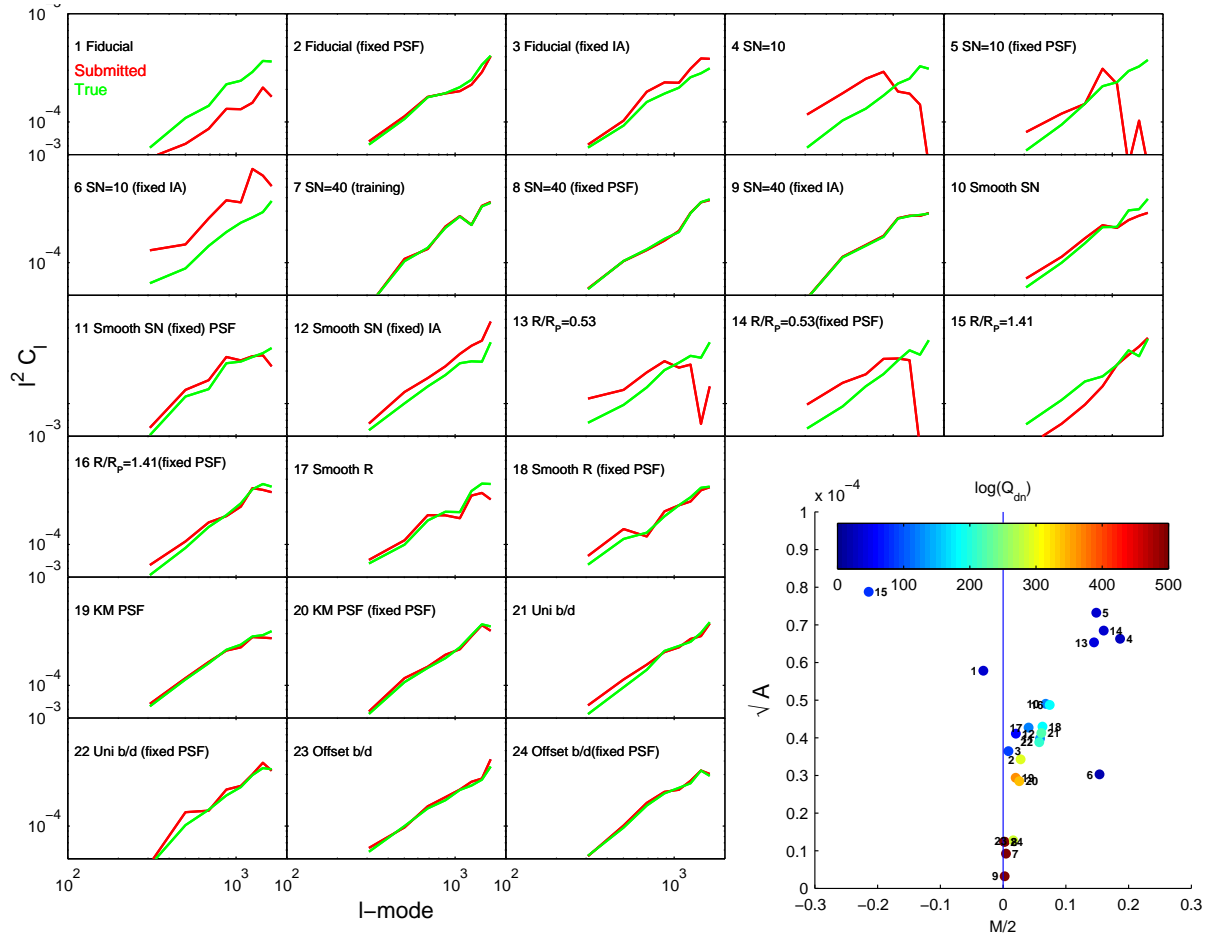


**Figure 23.** The true shear power (green) for each set and the shear power for the ‘fit2-unfold’ submission (red), we also show the ‘denoised’ power spectrum (blue) for each set (where this is indistinguishable from the raw submission a red line is only legible). The y-axes are  $C_\ell^2$  and the x-axis is  $\ell$ . In the bottom righthand corner we show the  $\mathcal{M}/2$ ,  $\sqrt{A}$  and the colour scale represents the logarithm of the quality factor. The small numbers next to each point label the set number.

#### E4. fit-unfold, cat-unfold, shapefit : David Kirkby, Daniel Margala

Each of these names refer to different submissions from the same underlying software. fit-unfold and cat-unfold were power spectrum submissions. The DeepZot analysis pipeline consists of four layers of software, implemented as C++ libraries, that were used for both the GREAT10 Galaxy Challenge and the MDM Challenge (Kitting et al. in prep). The first layer provides a uniform interface to the GREAT10 and MDM datasets. The next layer performs PSF and galaxy shape estimation using a maximum likelihood model-fitting method. A half-trace approximation KSB method is also implemented for comparison with earlier work and to provide a fast bootstrap of the model fit. The model-fitting code incorporates an optimised image synthesis engine and uses the MINUIT minimisation library to calculate full covariance matrices. The third layer provides supervised machine learning when a suitable training set is available, and is based on the TMVA package. The best results in the MDM Challenge were obtained with a 13-input neural network that derives ellipticity corrections from a combination of model-fitted parameters, covariance matrix elements, and KSB results. The final layer of the DeepZot software pipeline performs power-spectrum estimation and uses the model-fit errors to determine and subtract the variance due to shape measurement errors. The main computational bottleneck in the DeepZot pipeline is the model fit, that currently requires about 500ms per galaxy on a single Intel Xeon core for a typical fit to a 19-parameter galaxy model in which seven parameters are floating and a full covariance matrix is obtained.

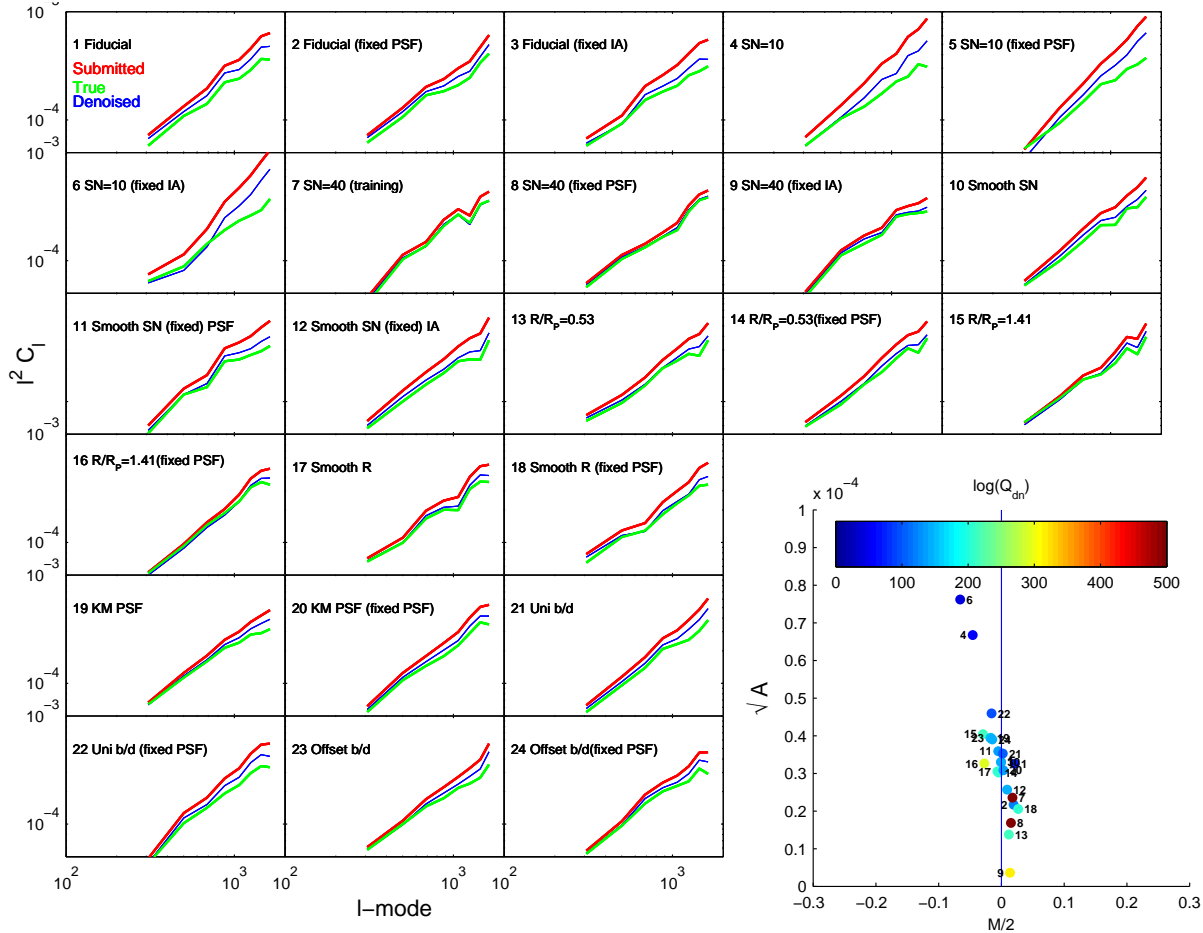


**Figure 24.** The true shear power (green) for each set and the shear power for the ‘gfit’ submission (red), we also show the ‘denoised’ power spectrum (blue) for each set (where this is indistinguishable from the raw submission a red line is only legible). The y-axes are  $C_\ell \ell^2$  and the x-axis is  $\ell$ . In the bottom righthand corner we show the  $M/2$ ,  $\sqrt{A}$  and the colour scale represents the logarithm of the quality factor. The small numbers next to each point label the set number.

### E5. gfit : Marc Gentile, Frederic Courbin, Guldariya Nurbaeva

The *gfit* shear measurement method is a simple forward model fitting method where the underlying galaxy is modelled using a 7-parameter Sérsic profile. The model parameters are the Sérsic index and radius ( $n, r_e$ ), the galaxy 2-component ellipticity ( $e_1, e_2$ ), the centroid ( $x_c, y_c$ ) and the flux intensity ( $I_0$ ) at  $r = 0$ . The galaxy and PSF centroids were estimated using **SExtractor** (Bertin & Arnouts, 1996).

For GREAT10, *gfit* used a different minimiser than that based on *Levenberg-Marquardt* previously used in GREAT08. The minimiser was developed at the Laboratory of Astrophysics of EPFL (LASTRO) with GREAT10 in mind. It has proven more robust and more accurate when fitting low SNR images.

The ‘gfit den cs’ version of *gfit* submitted in GREAT10 involved an experimental implementation of the new *DWT-Wiener* wavelet-based denoising method, also developed at LASTRO. DWT-Wiener proved very successful in all other methods we submitted in the Galaxy challenge (TVNN, MegaLUT). In the case of *gfit*, the  $Q$  factor was boosted by an estimated factor of 1.5. More details about the DWT-Wiener method can be found in Nurbaeva, Courbin et al., (2011).

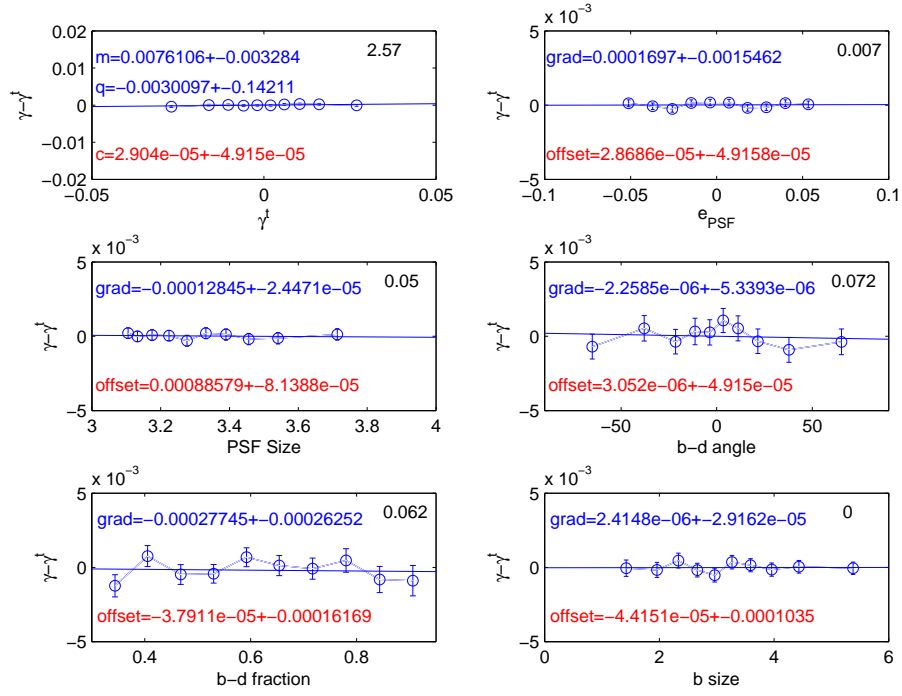


**Figure 25.** The measured minus true shear for the ‘gfit’ submission as a function of the true shear, PSF ellipticity, PSF FWHM, galaxy bulge-to-disk offset angle, galaxy bulge-to-disk fraction and galaxy bulge size. For each dependency we fit a linear function with a gradient and offset, for the top left hand panel this is the STEP  $m$  and  $c$  values, additionally for the shear dependency we include a quadratic term separately  $q$ . The top right hand corners show  $\Delta\chi^2 = \chi^2(\text{gradient}, \text{offset}) - \chi^2(\text{offset})$ .

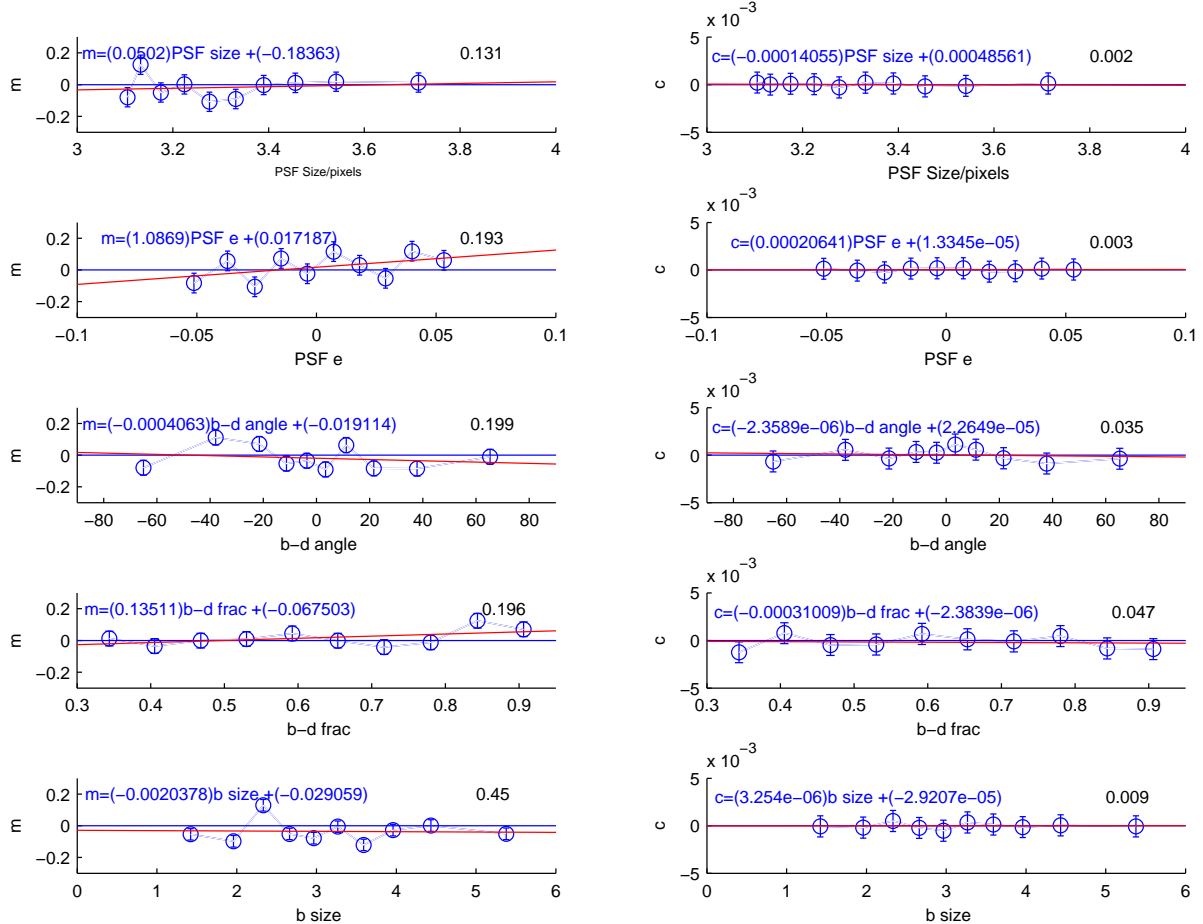


**Figure 26.** The STEP  $m$  and  $c$  values for the ‘gfit’ submission as a function of PSF FWHM and ellipticity, galaxy bulge-to-disk offset angle, galaxy bulge-to-disk fraction and galaxy bulge size. For each variable we plot the a linear relation to the behaviour of  $m$  and  $c$ . We do not explicitly quote errors on all parameters for clarity, the average errors on  $m$  and  $c$  are  $\simeq 0.005$  and  $5 \times 10^{-5}$  respectively. The top right hand corners show  $\Delta\chi^2 = \chi^2(\text{gradient}, \text{offset}) - \chi^2(\text{offset})$ .

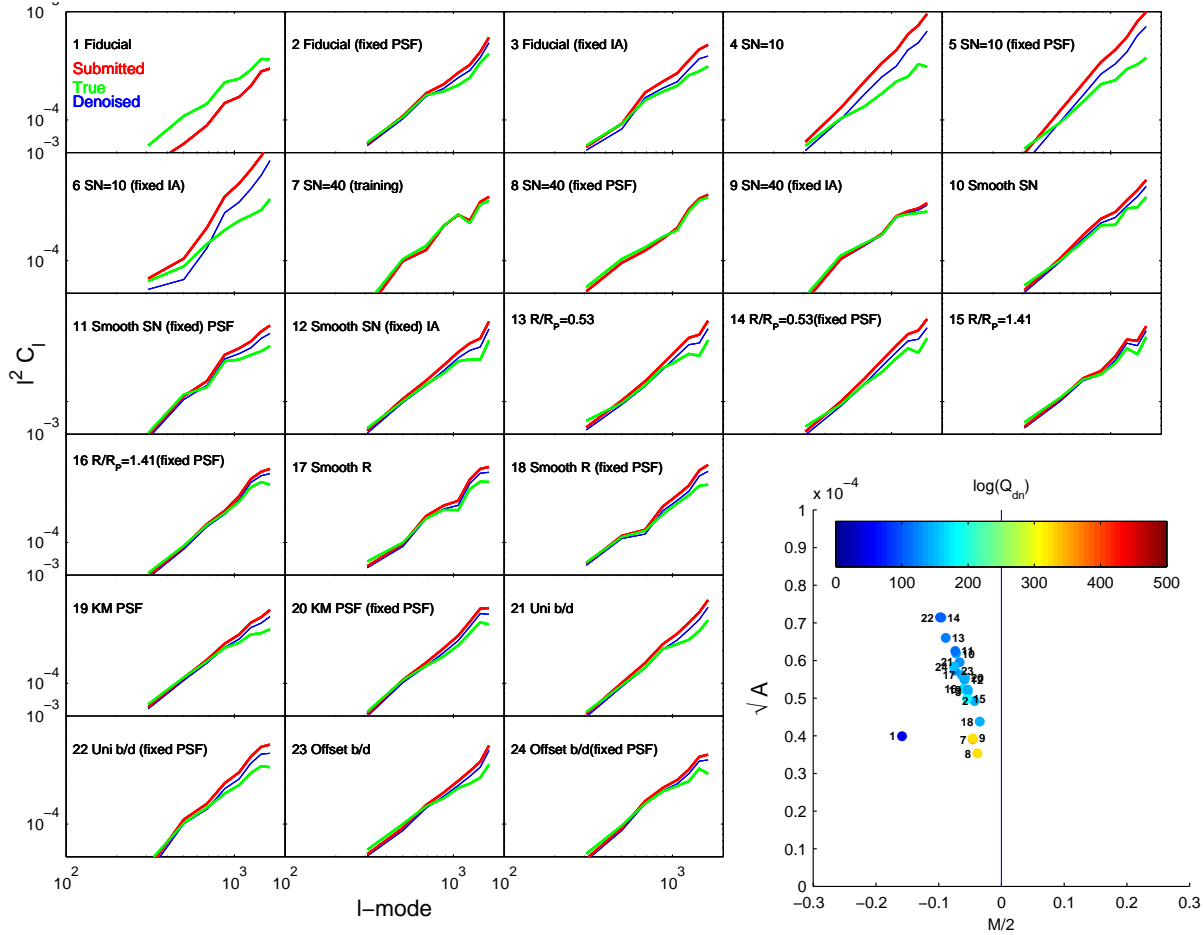


**Figure 27.** The true shear power (green) for each set and the shear power for the ‘im3shape NCB0’ submission (red), we also show the ‘denoised’ power spectrum (blue) for each set (where this is indistinguishable from the raw submission a red line is only legible). The y-axes are  $C_\ell \ell^2$  and the x-axis is  $\ell$ . In the bottom righthand corner we show the  $\mathcal{M}/2$ ,  $\sqrt{A}$  and the colour scale represents the logarithm of the quality factor. The small numbers next to each point label the set number.

#### E6. im3shape : Sarah Bridle, Tomasz Kacprzak, Barney Rowe, Lisa Voigt, Joe Zuntz

**im3shape** fitted a sum of co-elliptical and co-centered Sersic profiles. In this implementation two Sersic profiles were used with the Sersic indices fixed to be 1 (disk-like) and 4 (bulge-like) and a bulge to disk scale radius ratio set to 0.9. The functional form for the PSF was provided, and the convolution was performed on a grid three times the pixel resolution in each direction, with additional integration in the central pixels of the galaxy model image. The maximum likelihood point was used, with a  $\chi^2$  evaluated from the full  $48 \times 48$  postage stamp. The output ellipticity  $(a - b)/(a + b)$  was used as our shear estimate, but with a correction for noise bias for the submissions marked “NBC”. For the noise bias correction a noisy simulated image was produced of a fiducial galaxy using the machinery in the **im3shape** code. Simulations were also produced in which the ellipticity was increased by 0.1 in one or other direction. A straight line was fitted to the output shear estimates relative to the input ellipticity to measure multiplicative and additive errors and it was verified that the multiplicative and additive errors were zero in the absence of noise. For submissions marked “NBC0” two different kinds of noisy simulations were performed and used these to correct the shear estimates of the corresponding GREAT10 image sets for (i) Moffat PSF and fiducial GREAT10 SNR (ii) Moffat PSF and lowest GREAT10 SNR. For NBC1 the following combinations were used (i) Moffat PSF, fiducial GREAT10 SNR, PSF FWHM 3.3 pixels, bulge scale radius 4.3 pixels (ii) as previous but PSF FWHM 3.1 (iii) as previous but PSF FWHM 3.6 (iv) Moffat PSF, fiducial GREAT10 SNR, PSF FWHM 3.3 pixels, bulge scale radius 2.3 pixels (v) as previous but bulge scale radius 8 pixels (vi) Moffat PSF, low GREAT10 SNR, PSF FWHM 3.3 pixels, bulge scale radius 4.3 pixels (vii) as previous but PSF FWHM 3.1 (viii) as previous but PSF FWHM 3.6. The optimiser used to find the location of maximum likelihood in the model parameter space was “PRAXIS” (short for Principal AXIS) by Richard Brent, that is freely available from Netlib at <http://www.netlib.org/opt/>. The code is specifically written to make it easy to interchange optimisers and alternatives are also under investigation. For more information please refer to Zuntz et al. (in prep) for details about the **im3shape** code in general and Kacprzak et al. (in prep) for details of the noise bias calibration.

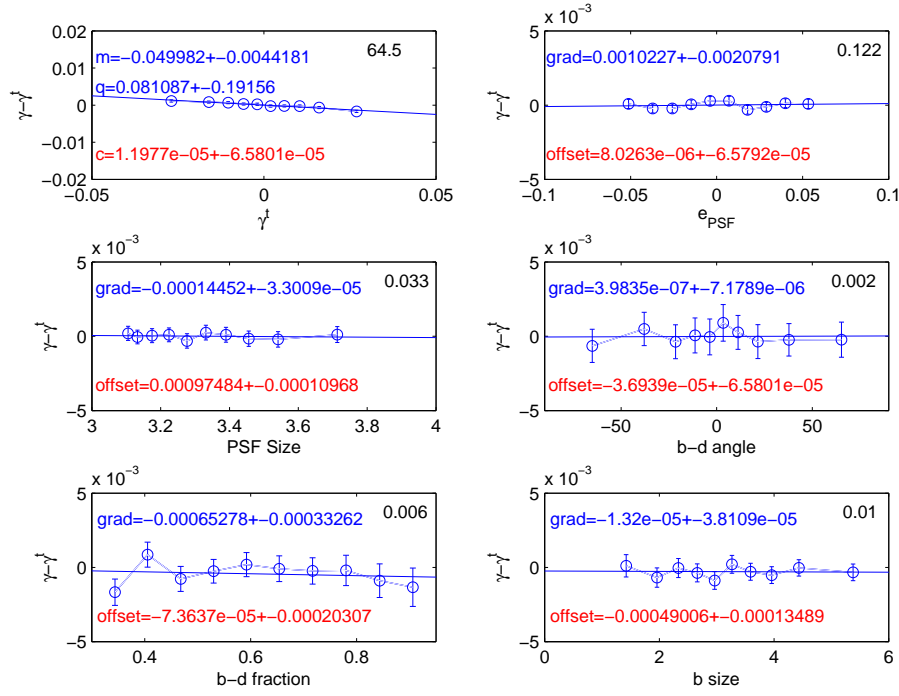


**Figure 28.** The measured minus true shear for the ‘im3shape NCB0’ submission as a function of the true shear, PSF ellipticity, PSF FWHM, galaxy bulge-to-disk offset angle, galaxy bulge-to-disk fraction and galaxy bulge size. For each dependency we fit a linear function with a gradient and offset, for the top left hand panel this is the STEP  $m$  and  $c$  values, additionally for the shear dependency we include a quadratic term separately  $q$ . The top right hand corners show  $\Delta\chi^2 = \chi^2(\text{gradient}, \text{offset}) - \chi^2(\text{offset})$ .

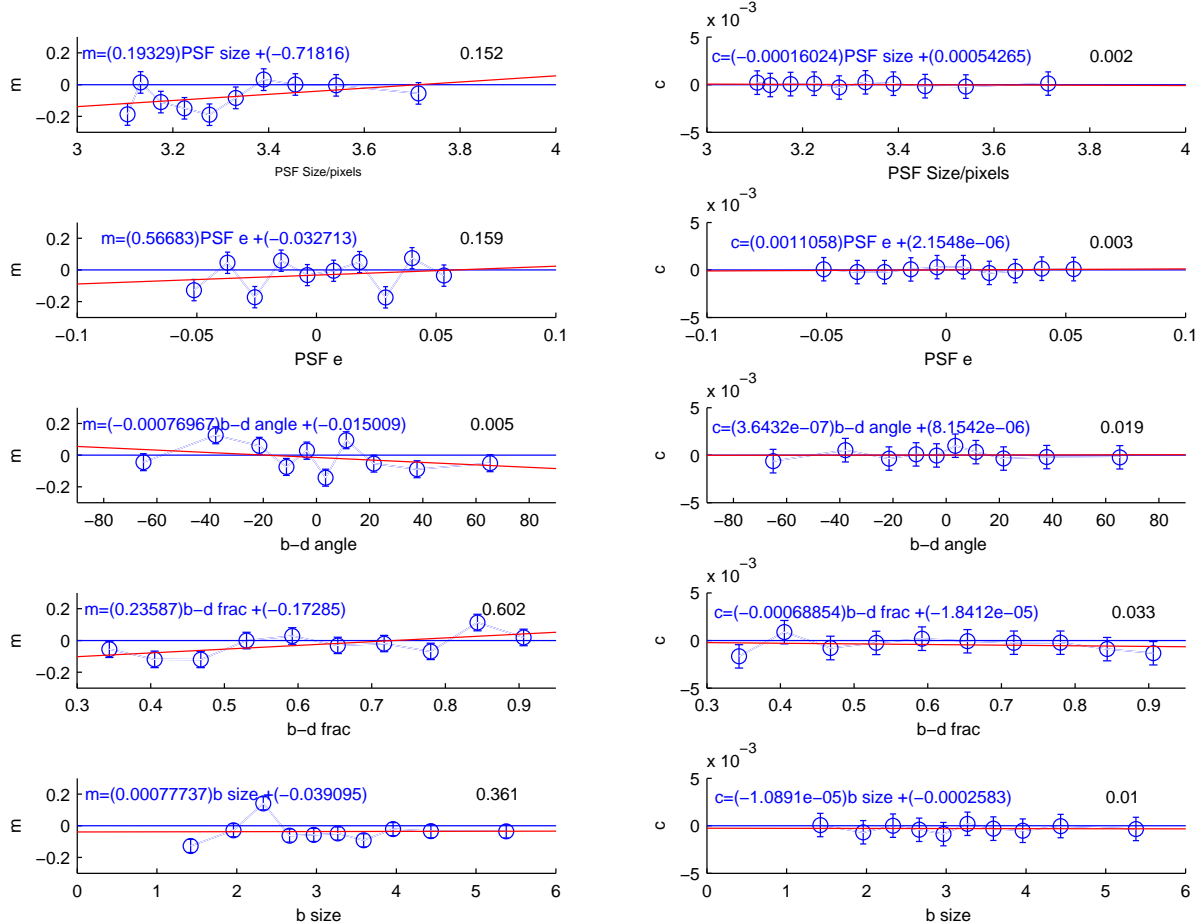


**Figure 29.** The STEP  $m$  and  $c$  values for the ‘im3shape NCB0’ submission as a function of PSF FWHM and ellipticity, galaxy bulge-to-disk offset angle, galaxy bulge-to-disk fraction and galaxy bulge size. For each variable we plot the a linear relation to the behaviour of  $m$  and  $c$ . We do not explicitly quote errors on all parameters for clarity, the average errors on  $m$  and  $c$  are  $\simeq 0.005$  and  $5 \times 10^{-5}$  respectively. The top right hand corners show  $\Delta\chi^2 = \chi^2(\text{gradient}, \text{offset}) - \chi^2(\text{offset})$ .

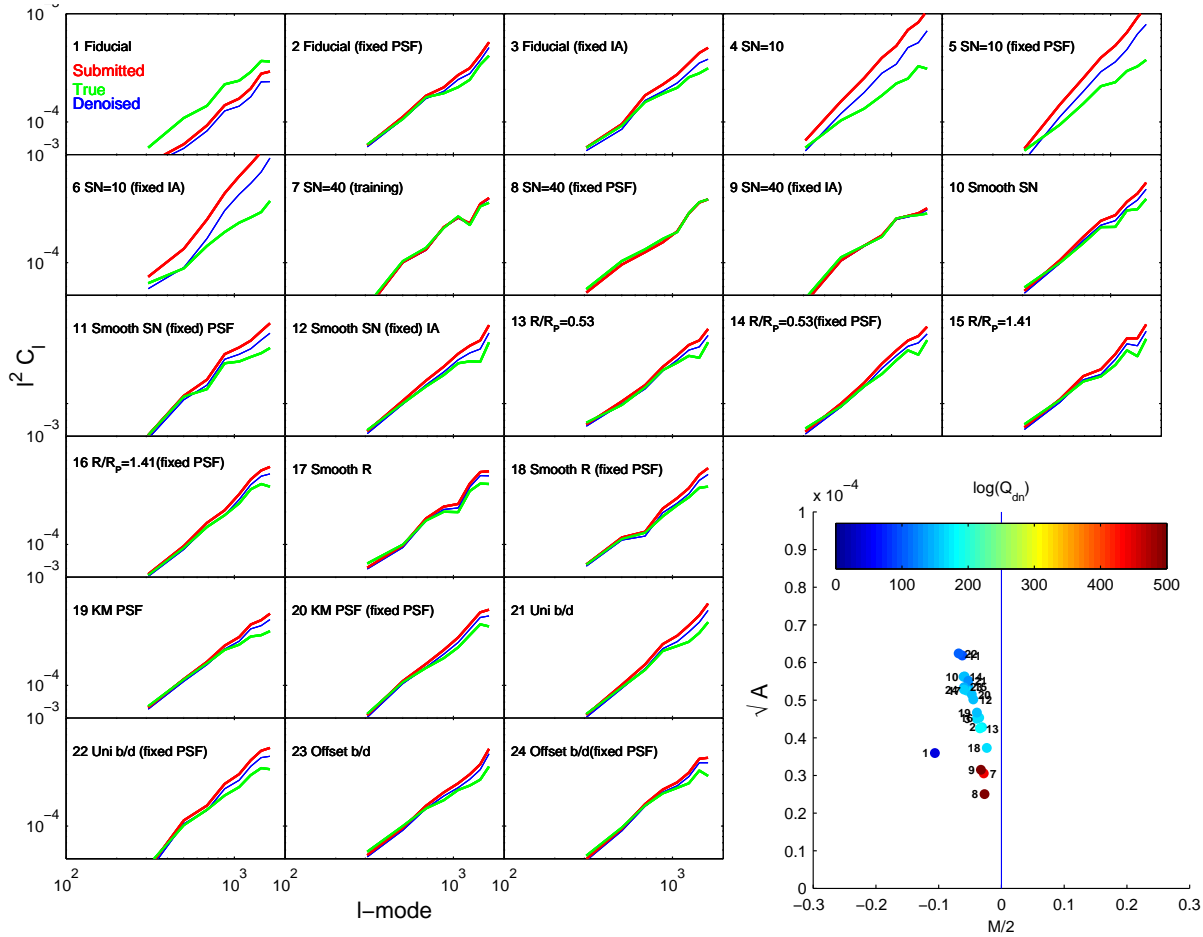


**Figure 30.** The true shear power (green) for each set and the shear power for the ‘KSB’ submission (red), we also show the ‘denoised’ power spectrum (blue) for each set (where this is indistinguishable from the raw submission a red line is only legible). The y-axes are  $C_\ell \ell^2$  and the x-axis is  $\ell$ . In the bottom righthand corner we show the  $\mathcal{M}/2$ ,  $\sqrt{A}$  and the colour scale represents the logarithm of the quality factor. The small numbers next to each point label the set number.

#### E7. KSB : Julia Young, Peter Melchior

The original KSB approach was implemented with the ‘trace-trick’, where the inversion of  $P^{sm}$  is achieved by replacing the entire  $2 \times 2$  matrix by  $1/2$  of its trace. This approach is employed in several studies, and it has recently recently been shown (Viola et al., 2011) that it provides the most unbiased shear estimates for a variety of observational condition.

To determine galaxy centroid and the width of the circular Gaussian weight function, the same iterative method employed in DEIMOS was used: determine the centroid such that the first moments vanish, and the size of the weight function such as to maximise S/N. For the final shear estimate, we did not apply additional fudge factors or responsivity corrections.

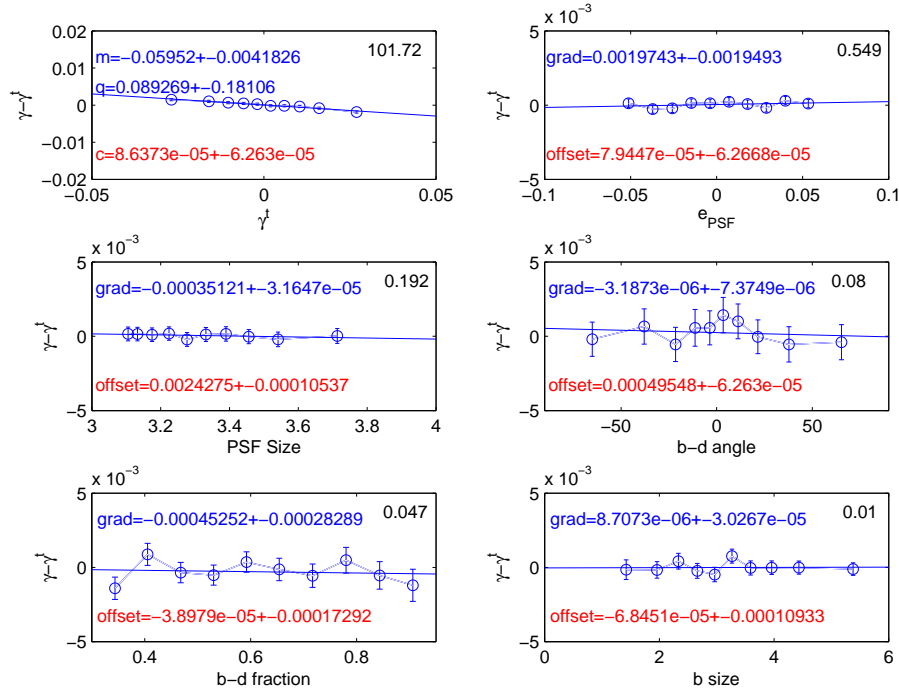


**Figure 31.** The measured minus true shear for the ‘KSB’ submission as a function of the true shear, PSF ellipticity, PSF FWHM, galaxy bulge-to-disk offset angle, galaxy bulge-to-disk fraction and galaxy bulge size. For each dependency we fit a linear function with a gradient and offset, for the top left hand panel this is the STEP  $m$  and  $c$  values, additionally for the shear dependency we include a quadratic term separately  $q$ . The top right hand corners show  $\Delta\chi^2 = \chi^2(\text{gradient}, \text{offset}) - \chi^2(\text{offset})$ .

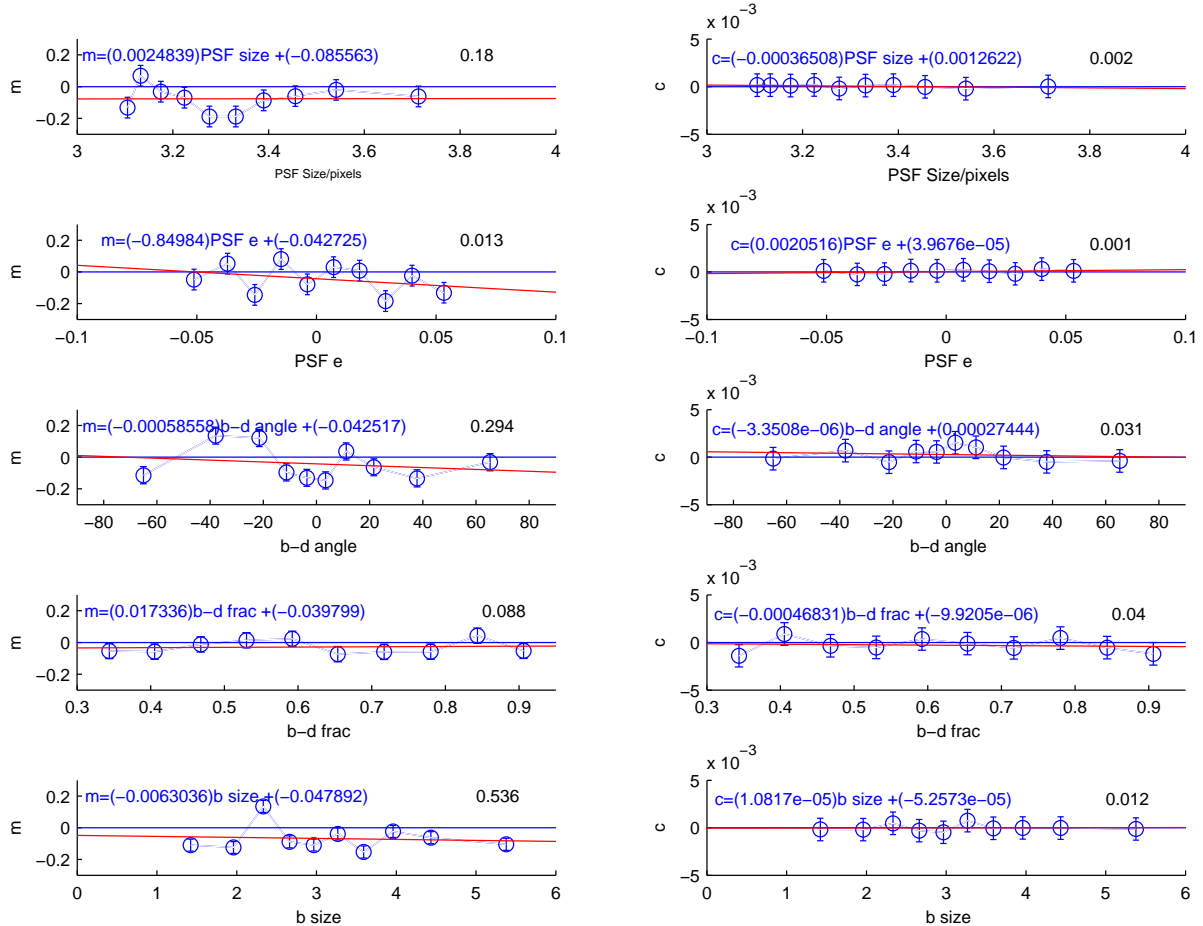


**Figure 32.** The STEP  $m$  and  $c$  values for the ‘KSB’ submission as a function of PSF FWHM and ellipticity, galaxy bulge-to-disk offset angle, galaxy bulge-to-disk fraction and galaxy bulge size. For each variable we plot the linear relation to the behaviour of  $m$  and  $c$ . We do not explicitly quote errors on all parameters for clarity, the average errors on  $m$  and  $c$  are  $\simeq 0.005$  and  $5 \times 10^{-5}$  respectively. The top right hand corners show  $\Delta\chi^2 = \chi^2(\text{gradient}, \text{offset}) - \chi^2(\text{offset})$ .

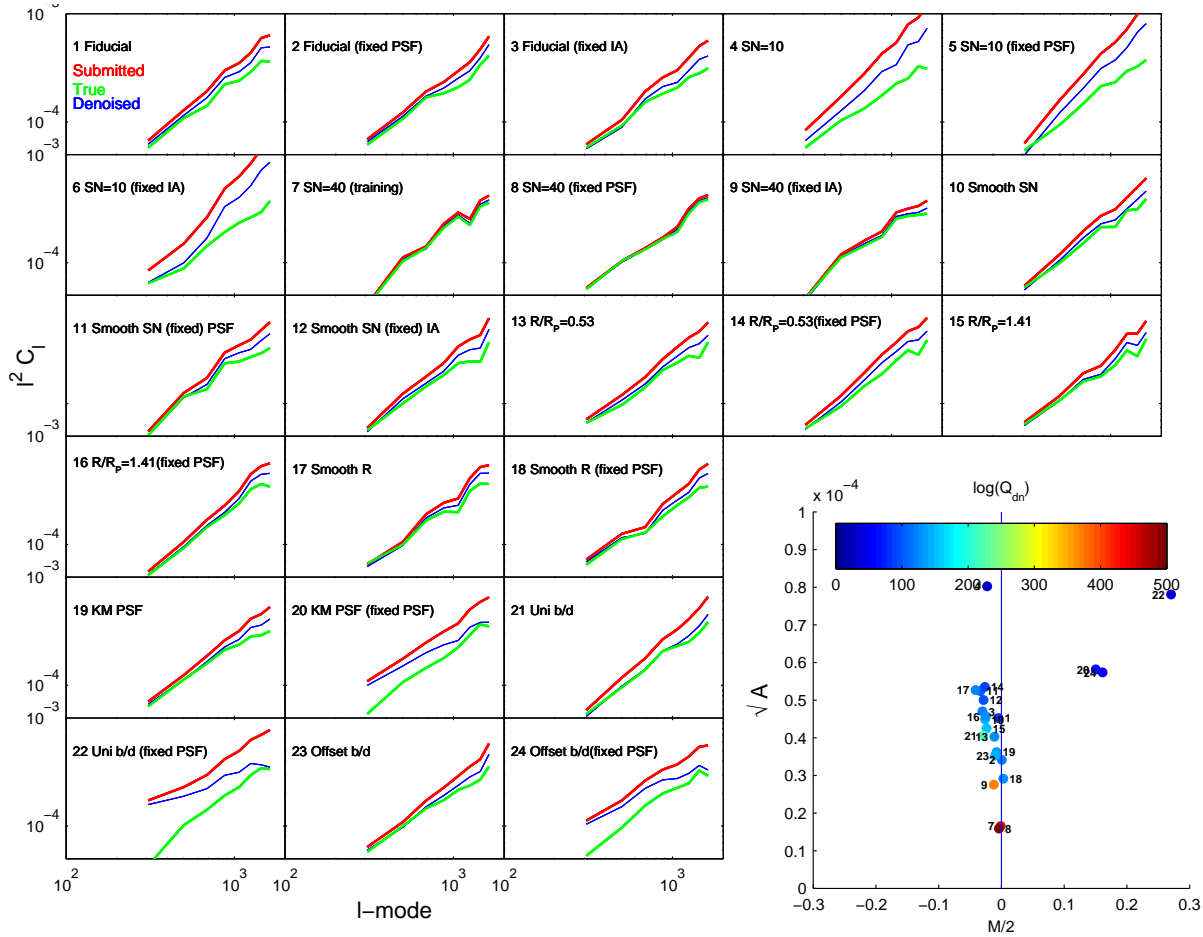


**Figure 33.** The true shear power (green) for each set and the shear power for the ‘KSB f90’ submission (red), we also show the ‘denoised’ power spectrum (blue) for each set (where this is indistinguishable from the raw submission a red line is only legible). The y-axes are  $C_\ell \ell^2$  and the x-axis is  $\ell$ . In the bottom righthand corner we show the  $\mathcal{M}/2$ ,  $\sqrt{A}$  and the colour scale represents the logarithm of the quality factor. The small numbers next to each point label the set number.

### E8. KSB f90 : Catherine Heymans

KSB f90 is a benchmark implementation of the longstanding KSB+ method (Kaiser, Squires & Broadhurst 1995, Luppino & Kaiser 1996 and Hoekstra et al 1998). This code is identical to that used in the ‘CH’ analysis of STEP1 and GREAT08 (Heymans et al 2006a, Bridle et al 2010) and can therefore be viewed as a benchmark to compare the different simulations. KSB f90 is publicly available and can be downloaded from <http://www.roe.ac.uk/~heyman/KSBf90>. The code has been used to analyse the GEMS and STAGES HST surveys (Heymans et al 2005, Heymans et al 2008). The accuracy of KSB f90 has a strong S/N dependence as shown in this paper yielding an incorrect redshift scaling of the lensing signal in real data. For this reason, whilst KSB f90 has been shown to perform well on average and for signal-to-noise > 20, author C. Heymans advises not to use this shape measurement method for low signal-to-noise data.



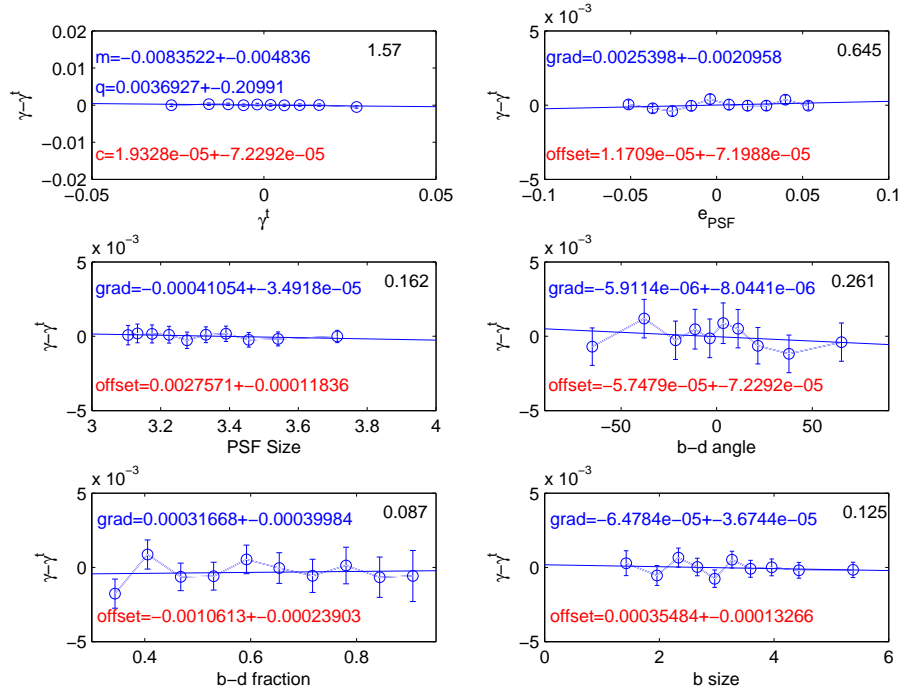


**Figure 34.** The measured minus true shear for the ‘KSB f90’ submission as a function of the true shear, PSF ellipticity, PSF FWHM, galaxy bulge-to-disk offset angle, galaxy bulge-to-disk fraction and galaxy bulge size. For each dependency we fit a linear function with a gradient and offset, for the top left hand panel this is the STEP  $m$  and  $c$  values, additionally for the shear dependency we include a quadratic term separately  $q$ . The top right hand corners show  $\Delta\chi^2 = \chi^2(\text{gradient}, \text{offset}) - \chi^2(\text{offset})$ .

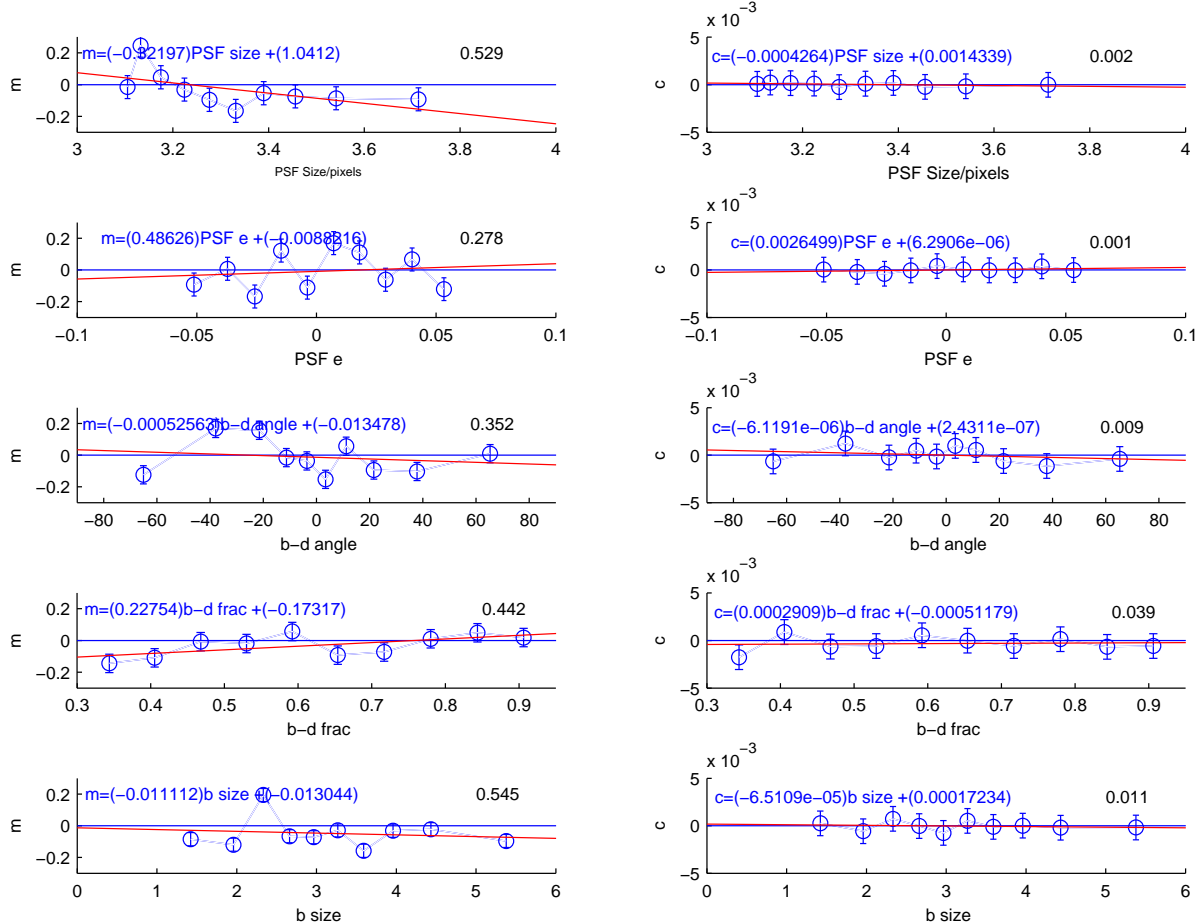


**Figure 35.** The STEP  $m$  and  $c$  values for the ‘KSB f90’ submission as a function of PSF FWHM and ellipticity, galaxy bulge-to-disk offset angle, galaxy bulge-to-disk fraction and galaxy bulge size. For each variable we plot the a linear relation to the behaviour of  $m$  and  $c$ . We do not explicitly quote errors on all parameters for clarity, the average errors on  $m$  and  $c$  are  $\simeq 0.005$  and  $5 \times 10^{-5}$  respectively. The top right hand corners show  $\Delta\chi^2 = \chi^2(\text{gradient}, \text{offset}) - \chi^2(\text{offset})$ .

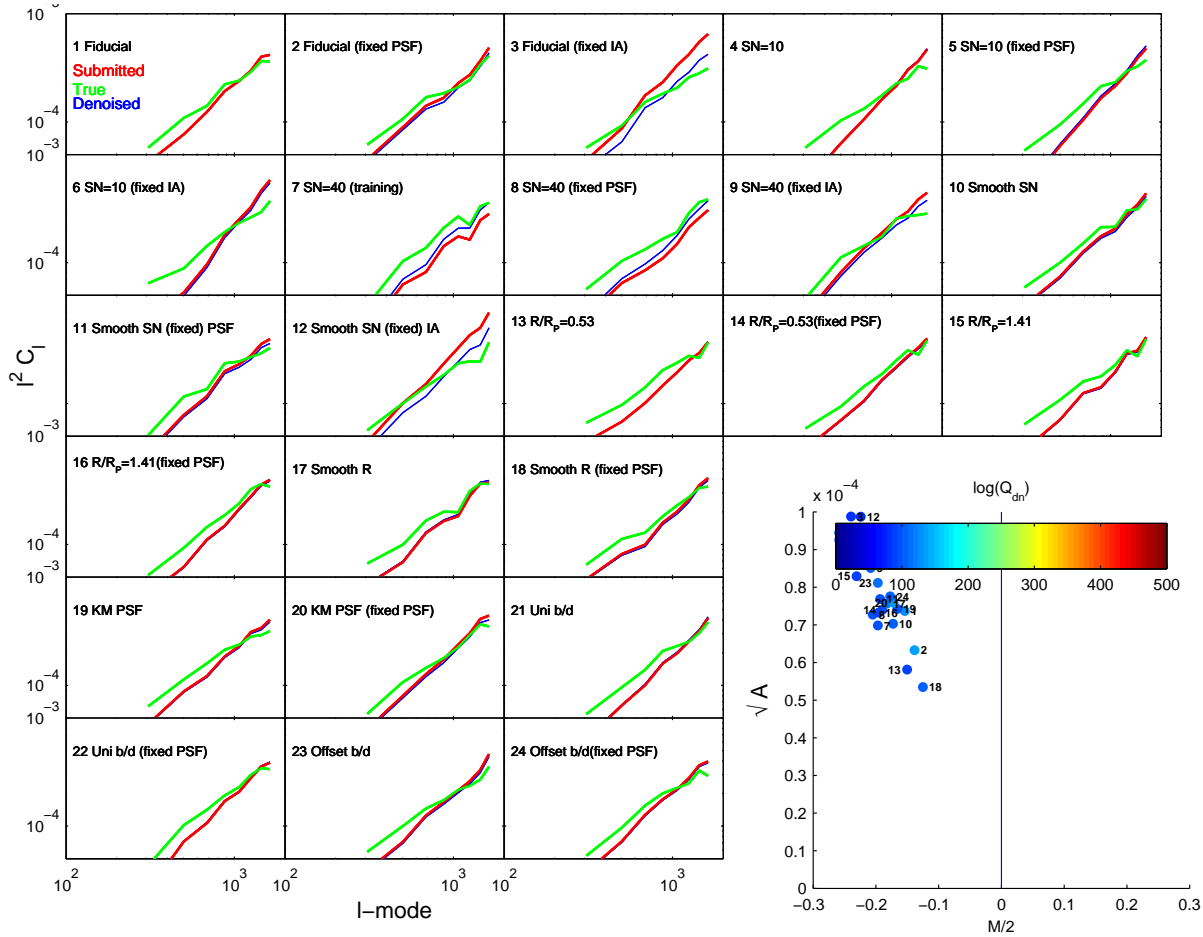


**Figure 36.** The true shear power (green) for each set and the shear power for the ‘MegaLUTsim2.1 b20’ submission (red), we also show the ‘denoised’ power spectrum (blue) for each set (where this is indistinguishable from the raw submission a red line is only legible). The y-axes are  $C_\ell^2$  and the x-axis is  $\ell$ . In the bottom righthand corner we show the  $\mathcal{M}/2$ ,  $\sqrt{A}$  and the colour scale represents the logarithm of the quality factor. The small numbers next to each point label the set number.

### E9. MegaLUT : Malte Tewes, Nicolas Cantale, Frederic Courbin

MegaLUT is a fast empirical method to correct ellipticity measurements of galaxies for the distortions by the PSF. It uses a straightforward classification scheme, namely a lookup table (LUT), built by supervised learning. In the scope of our submissions to GREAT10, the successive steps of MegaLUT can be summarised as follows: 1. Simulate a large number of realistic galaxy and PSF stamps and store the sheared galaxy ellipticities prior to the PSF convolution. This leads to a learning sample of images. 2. Run a shape measurement algorithm on the galaxies and PSFs of this learning sample and create a lookup table that connects the measured galaxy and PSF shapes to the known galaxy ellipticities stored in the first step. 3. For a given galaxy/PSF pair in the GREAT10 data, run the same shape measurement algorithms as in step 2. Query the lookup table to identify the galaxy/PSF pairs of the learning sample that have similar measured shapes. The galaxy ellipticities of these selected pairs, *as stored at step 1*, yield our estimate of the galaxy ellipticity prior to the convolution by the PSF. The complex problem of PSF correction is therefore reduced to a simple and fast array indexing operation.

For the final submission ‘MegaLUTsim2.1 b20’, we denoised the galaxy and PSF images with wavelet filtering, and built simple threshold masks. The shapes were then measured using second order moments of the masked light distributions. The lookup table was generated from 2.1 million simulated galaxy/PSF pairs.

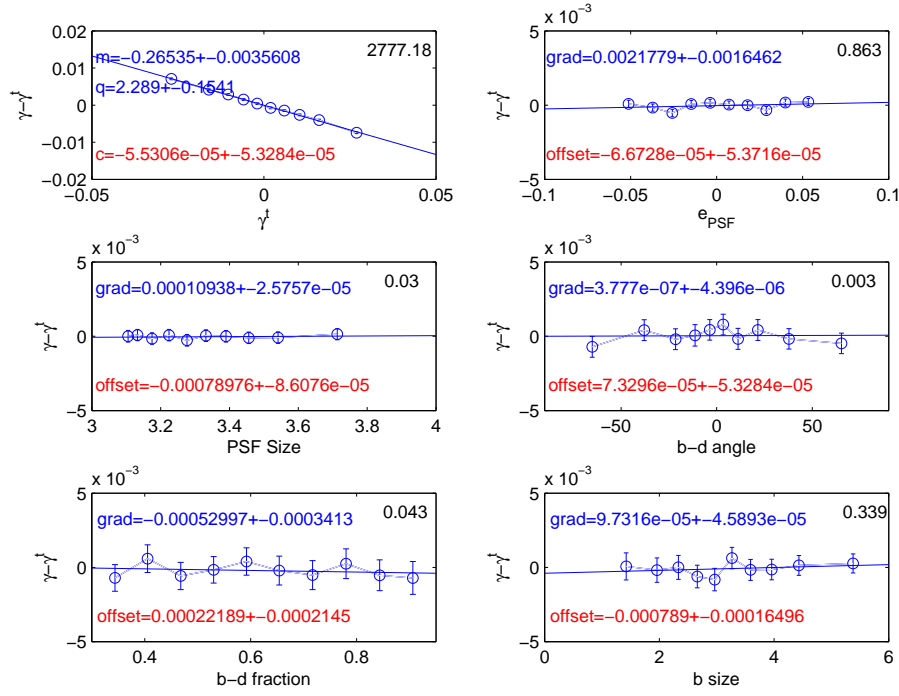


**Figure 37.** The measured minus true shear for the ‘MegaLUTsim2.1 b20’ submission as a function of the true shear, PSF ellipticity, PSF FWHM, galaxy bulge-to-disk offset angle, galaxy bulge-to-disk fraction and galaxy bulge size. For each dependency we fit a linear function with a gradient and offset, for the top left hand panel this is the STEP  $m$  and  $c$  values, additionally for the shear dependency we include a quadratic term separately  $q$ . The top right hand corners show  $\Delta\chi^2 = \chi^2(\text{gradient, offset}) - \chi^2(\text{offset})$ .

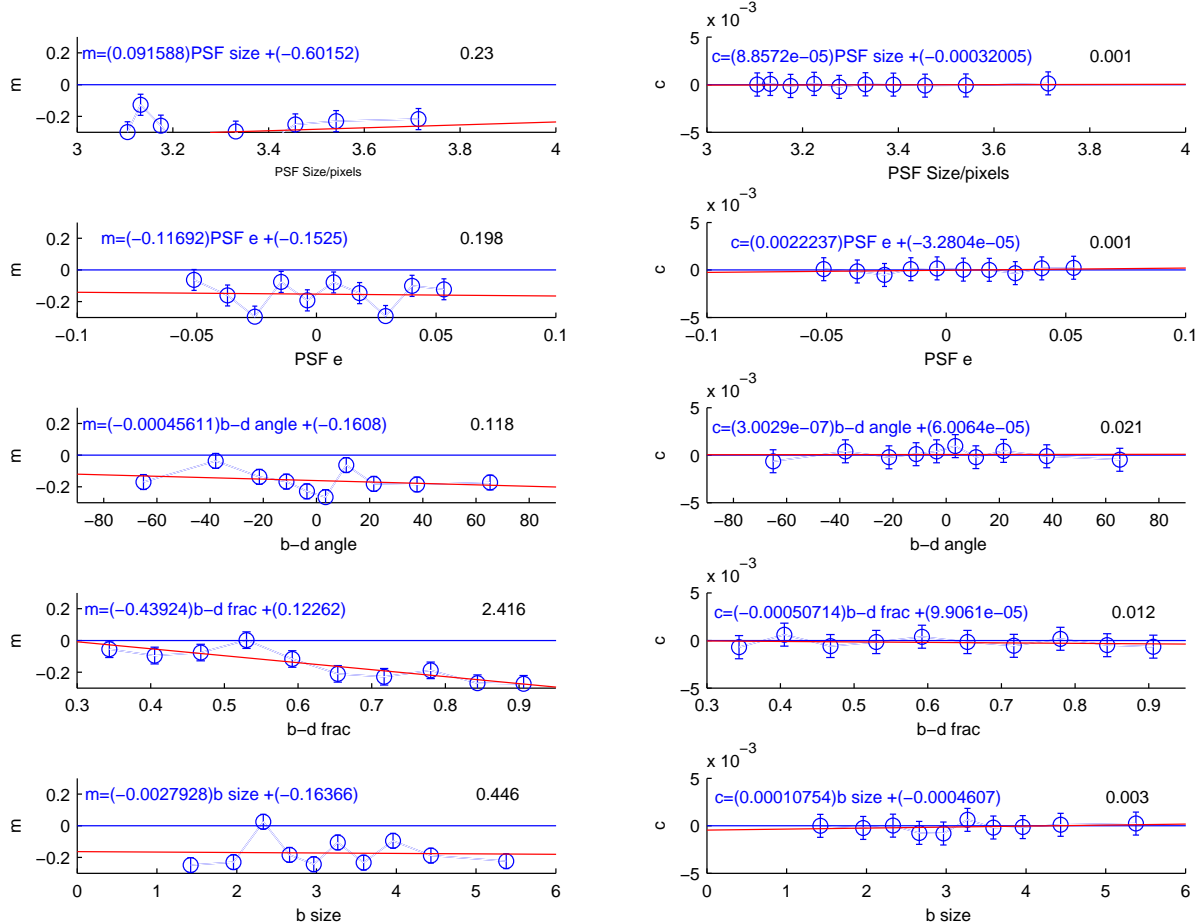


**Figure 38.** The STEP  $m$  and  $c$  values for the ‘MegaLUTsim2.1 b20’ submission as a function of PSF FWHM and ellipticity, galaxy bulge-to-disk offset angle, galaxy bulge-to-disk fraction and galaxy bulge size. For each variable we plot the a linear relation to the behaviour of  $m$  and  $c$ . We do not explicitly quote errors on all parameters for clarity, the average errors on  $m$  and  $c$  are  $\simeq 0.005$  and  $5 \times 10^{-5}$  respectively. The top right hand corners show  $\Delta\chi^2 = \chi^2(\text{gradient, offset}) - \chi^2(\text{offset})$ .

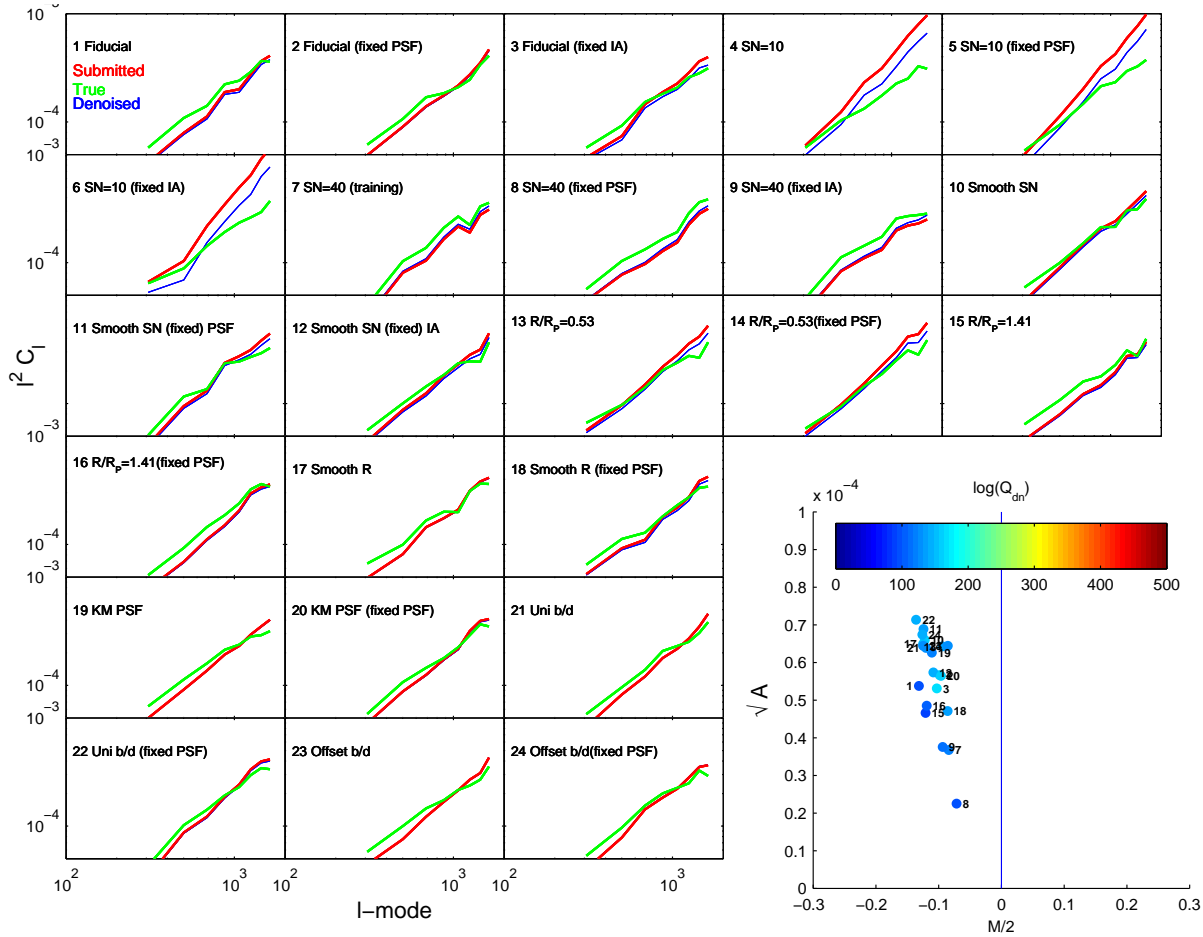


**Figure 39.** The true shear power (green) for each set and the shear power for the ‘method 4’ submission (red), we also show the ‘denoised’ power spectrum (blue) for each set (where this is indistinguishable from the raw submission a red line is only legible). The y-axes are  $C_\ell^2$  and the x-axis is  $\ell$ . In the bottom righthand corner we show the  $\mathcal{M}/2$ ,  $\sqrt{A}$  and the colour scale represents the logarithm of the quality factor. The small numbers next to each point label the set number.

#### E10. method4,5,7 : Micheal Hirsch, Stefan Harmeling

In a series of submissions named method0x with  $x \in \{1, \dots, 7\}$  the effect of taking higher order pixel correlations on the accuracy of shear measurement was tested. In method01 the shear was measured by subtracting the quadrupole moments of the auto-correlated images of the galaxy and corresponding PSF images. The assumption of uncorrelated noise is confirmed by the fact that the auto-correlation is highly peaked at zero shift. To get rid of this peak which impedes accurate moment estimation, a rough estimate of the noise variance was obtained by computing the variance of pixels with negative intensity values only (assuming Gaussian noise with zero mean) which was then subtracted from the central pixel. As in any other KSB-type method, noise affects moment estimation and has to be accounted for by some weighting scheme. To this end both galaxy and star images were modulated by a Gaussian with fixed variance and zero centroid. By noticing that a pixel-wise modulation corresponds to a convolution in Fourier space, a correction for the induced error due to the modulation could be removed by subtracting the measured quadrupole moment and the fixed variance of the Gaussian distribution used for weighting in the Fourier domain. In method04, we went one step further by computing the auto-correlation of the auto-correlated galaxy or star image, otherwise pursuing the the same approach as described above. By this the images are even further smoothed and are still centered such that inaccuracies in centroid estimation are not an issue in our approach. All other methods are variants of the above where the empirical moment estimation with a Gaussian weighting scheme was replaced by a model fitting approach (method02), introduced an additional denoising step (method05), did empirical moment estimation without additional weighting (method03) and accounted for the PSF by a Wiener deconvolution of the galaxy images before moment estimation (method07).

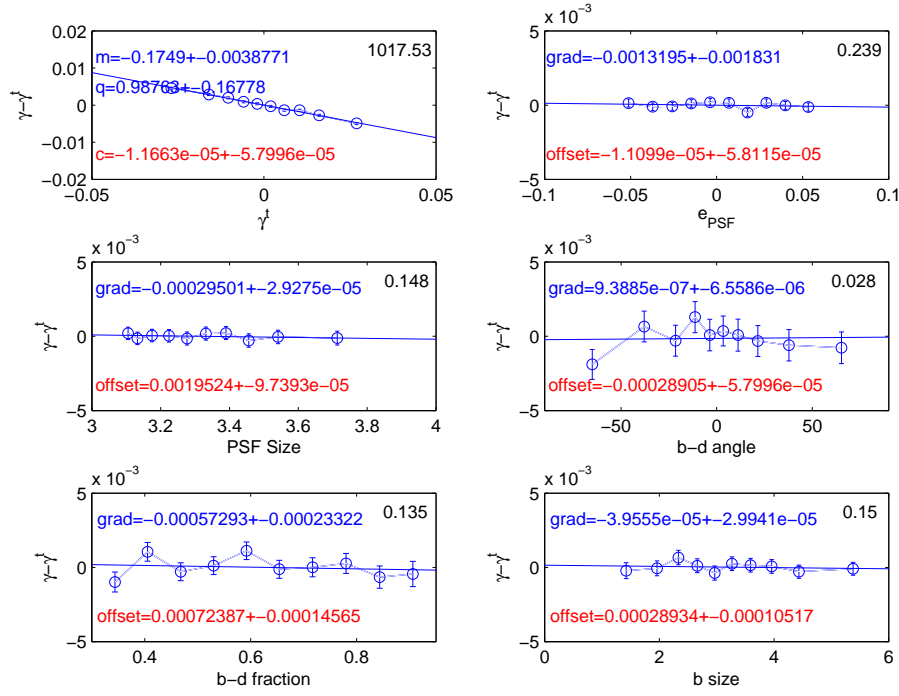


**Figure 40.** The measured minus true shear for the ‘method 4’ submission as a function of the true shear, PSF ellipticity, PSF FWHM, galaxy bulge-to-disk offset angle, galaxy bulge-to-disk fraction and galaxy bulge size. For each dependency we fit a linear function with a gradient and offset, for the top left hand panel this is the STEP  $m$  and  $c$  values, additionally for the shear dependency we include a quadratic term separately  $q$ . The top right hand corners show  $\Delta\chi^2 = \chi^2(\text{gradient, offset}) - \chi^2(\text{offset})$ .

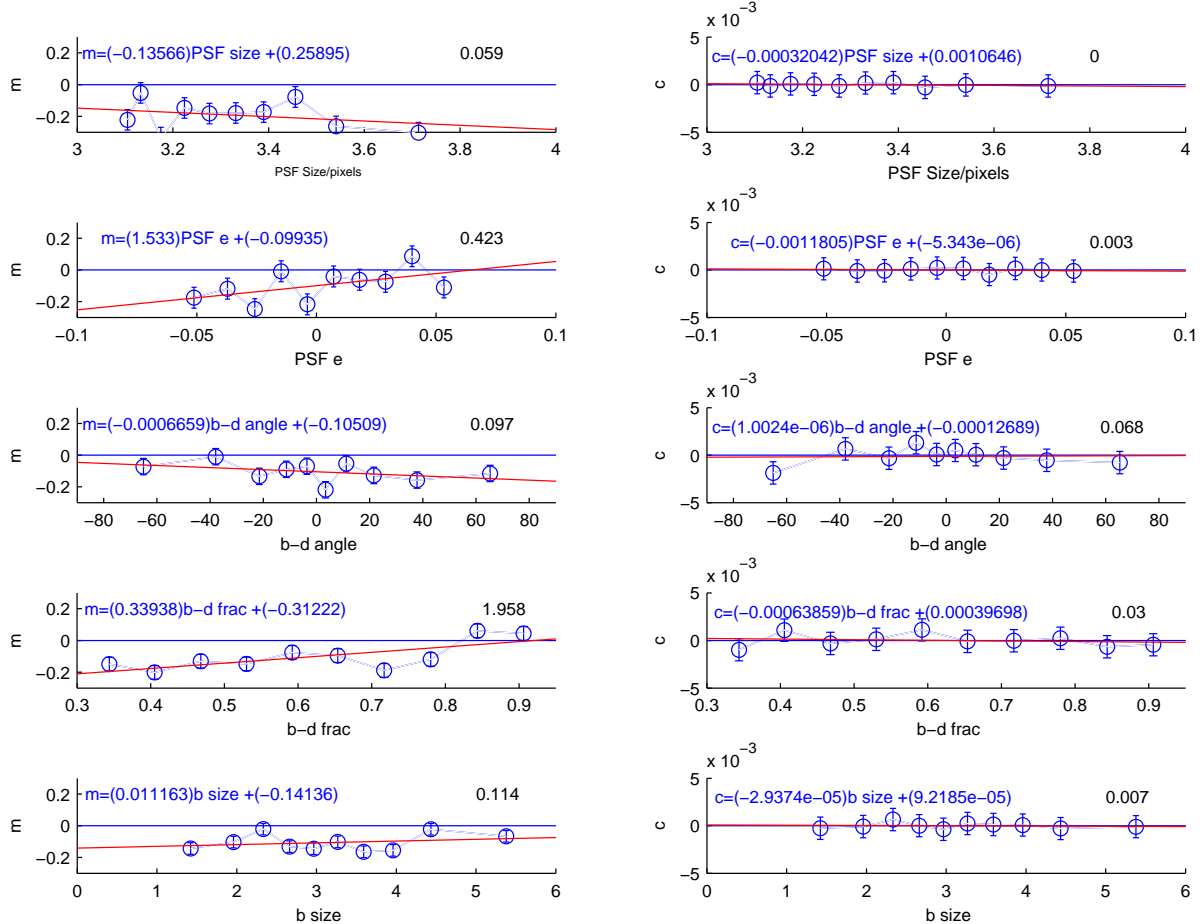


**Figure 41.** The STEP  $m$  and  $c$  values for the ‘method 4’ submission as a function of PSF FWHM and ellipticity, galaxy bulge-to-disk offset angle, galaxy bulge-to-disk fraction and galaxy bulge size. For each variable we plot the a linear relation to the behaviour of  $m$  and  $c$ . We do not explicitly quote errors on all parameters for clarity, the average errors on  $m$  and  $c$  are  $\simeq 0.005$  and  $5 \times 10^{-5}$  respectively. The top right hand corners show  $\Delta\chi^2 = \chi^2(\text{gradient, offset}) - \chi^2(\text{offset})$ .

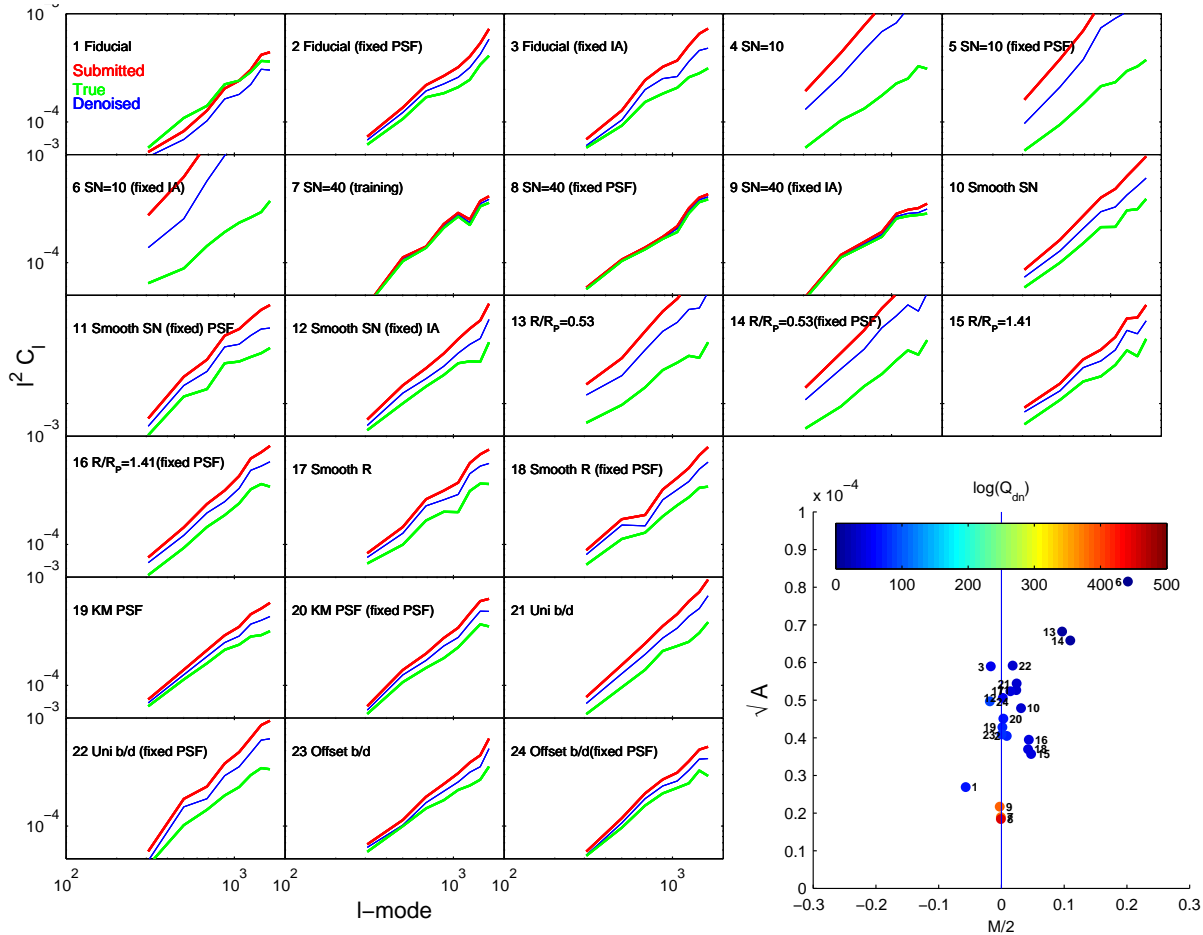


**Figure 42.** The true shear power (green) for each set and the shear power for the ‘shapefit’ submission (red), we also show the ‘denoised’ power spectrum (blue) for each set (where this is indistinguishable from the raw submission a red line is only legible). The y-axes are  $C_\ell \ell^2$  and the x-axis is  $\ell$ . In the bottom righthand corner we show the  $\mathcal{M}/2$ ,  $\sqrt{A}$  and the colour scale represents the logarithm of the quality factor. The small numbers next to each point label the set number.

#### E11. shapefit: David Kirkby, Daniel Margala

See fit-unfold description.

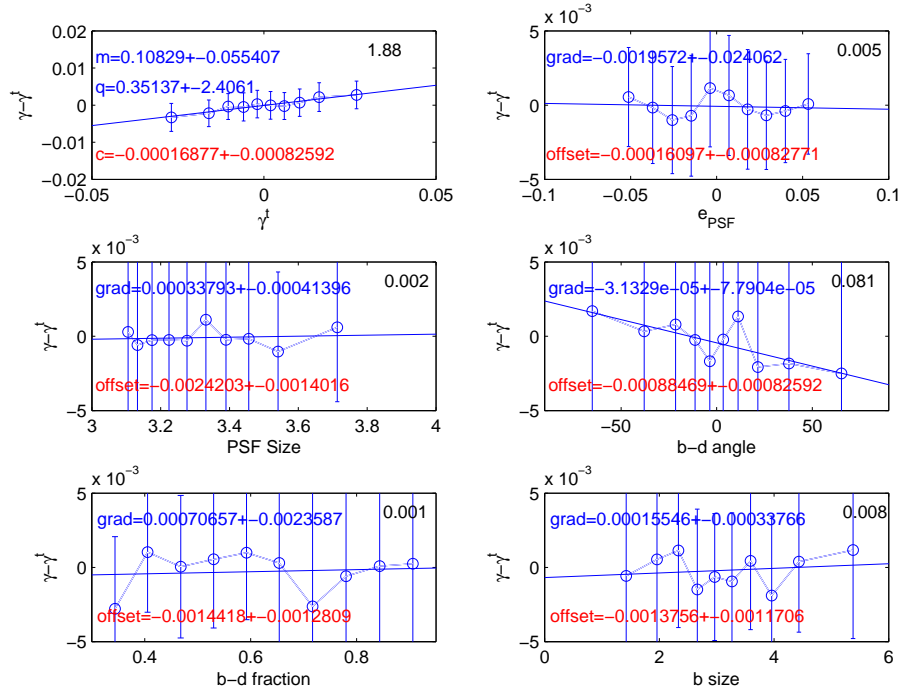


**Figure 43.** The measured minus true shear for the ‘shapefit’ submission as a function of the true shear, PSF ellipticity, PSF FWHM, galaxy bulge-to-disk offset angle, galaxy bulge-to-disk fraction and galaxy bulge size. For each dependency we fit a linear function with a gradient and offset, for the top left hand panel this is the STEP  $m$  and  $c$  values, additionally for the shear dependency we include a quadratic term separately  $q$ . The top right hand corners show  $\Delta\chi^2 = \chi^2(\text{gradient, offset}) - \chi^2(\text{offset})$ .

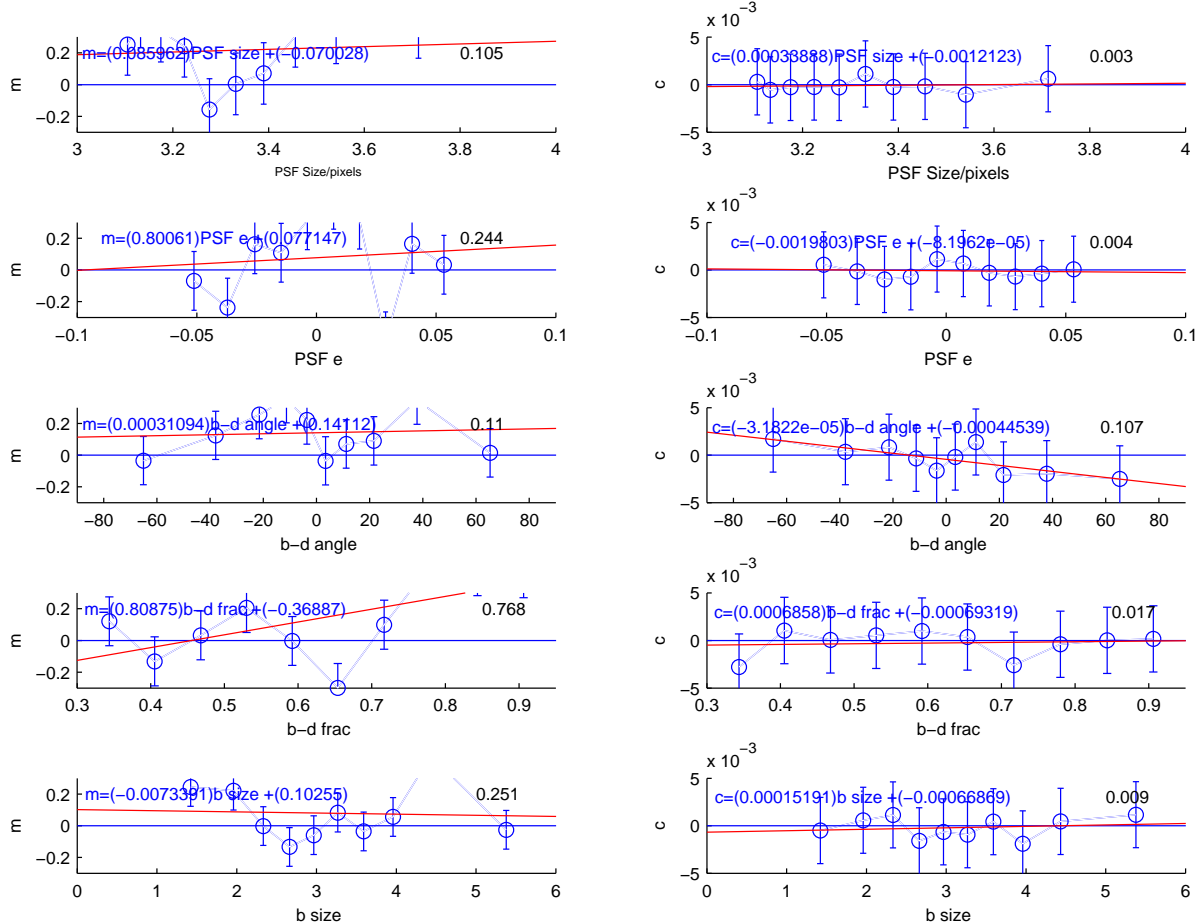


**Figure 44.** The STEP  $m$  and  $c$  values for the ‘shapefit’ submission as a function of PSF FWHM and ellipticity, galaxy bulge-to-disk offset angle, galaxy bulge-to-disk fraction and galaxy bulge size. For each variable we plot the a linear relation to the behaviour of  $m$  and  $c$ . We do not explicitly quote errors on all parameters for clarity, the average errors on  $m$  and  $c$  are  $\simeq 0.005$  and  $5 \times 10^{-5}$  respectively. The top right hand corners show  $\Delta\chi^2 = \chi^2(\text{gradient, offset}) - \chi^2(\text{offset})$ .

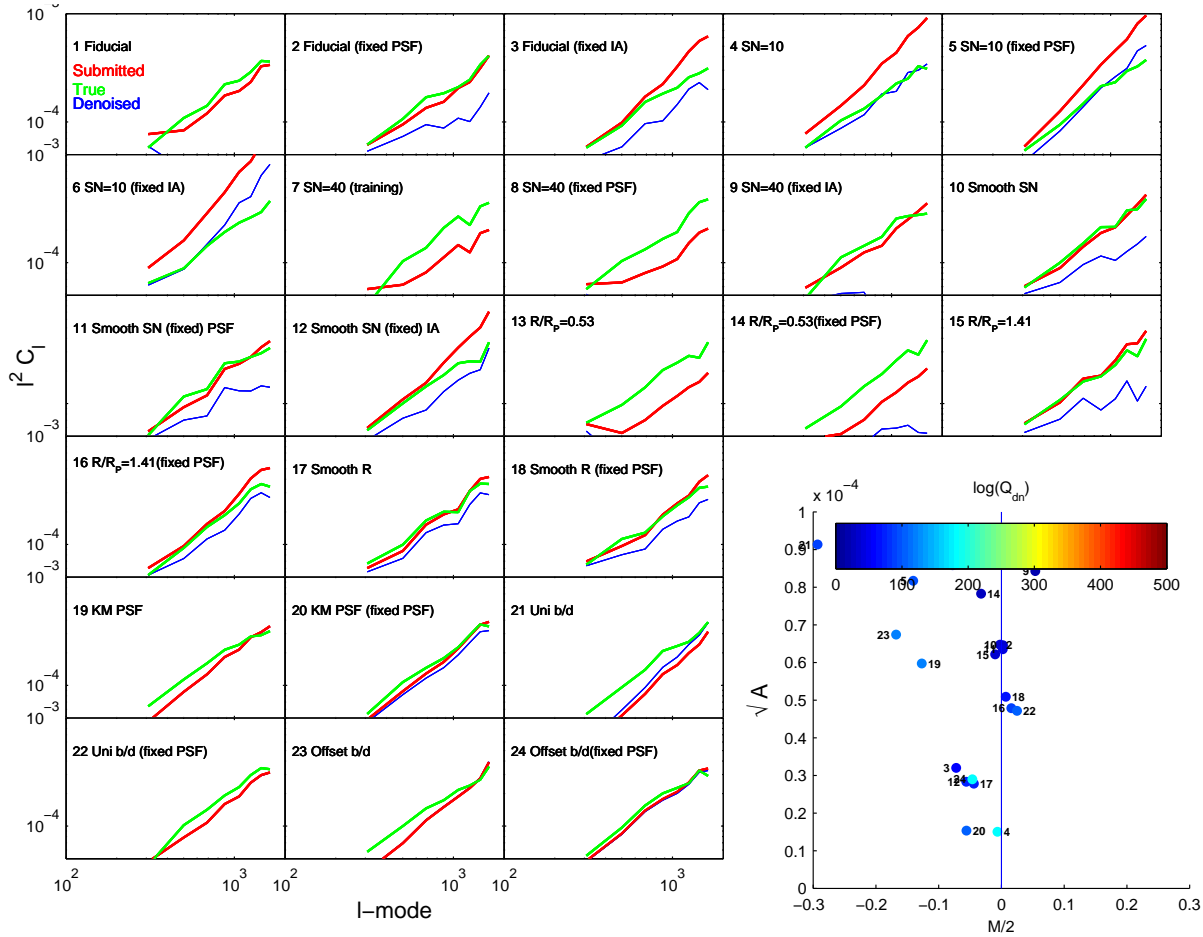


**Figure 45.** The true shear power (green) for each set and the shear power for the ‘NN23’ submission (red), we also show the ‘denoised’ power spectrum (blue) for each set (where this is indistinguishable from the raw submission a red line is only legible). The y-axes are  $C_\ell \ell^2$  and the x-axis is  $\ell$ . In the bottom righthand corner we show the  $M/2$ ,  $\sqrt{A}$  and the colour scale represents the logarithm of the quality factor. The small numbers next to each point label the set number.

## E12. TVNN: Guldariya Nurbaeva, Frederic Courbin, Malte Tewes, Marc Gentile

The methods NN23 func, NN19 and NN21, submitted to GREAT10, were variants of the Total Variation Neural Network (TVNN) method, that is a deconvolution technique based on the combination of a Hopfield neural network (Hopfield, 1982) with the Total Variation model proposed by Rudin, Osher and Fatemi (Rudin, 1992). In the Total Variation model, the noise in the image is assumed to follow a Gaussian distribution.

The deconvolution process is carried out by minimising the energy function of the Hopfield Neural Network. This energy function is composed of the PSF, expressed as a Toeplitz matrix, and of a regularisation term to minimise the noise. The latter is a Sobel high-pass operator. The deconvolution itself is done in an iterative way where at each step, the neurons of the network are updated so as to minimise the energy function.

Galaxy ellipticities are then estimated from quadrupole moments computed on the 2D auto-correlation function (ACF) of the deconvolved image. The advantages of using the ACF are 1- high signal-to-noise shape measurement, 2- invariance of the ellipticity measurement with respect to data (Waerbeke, 1997; Miralda-Escude, 1991)

In our submissions, the number after the acronym NN stands for the size of the input data stamps, i.e., NN23 considers images with 23 pixels on a side. This is the first time full-deconvolution of the data is used to carry out shape measurements.



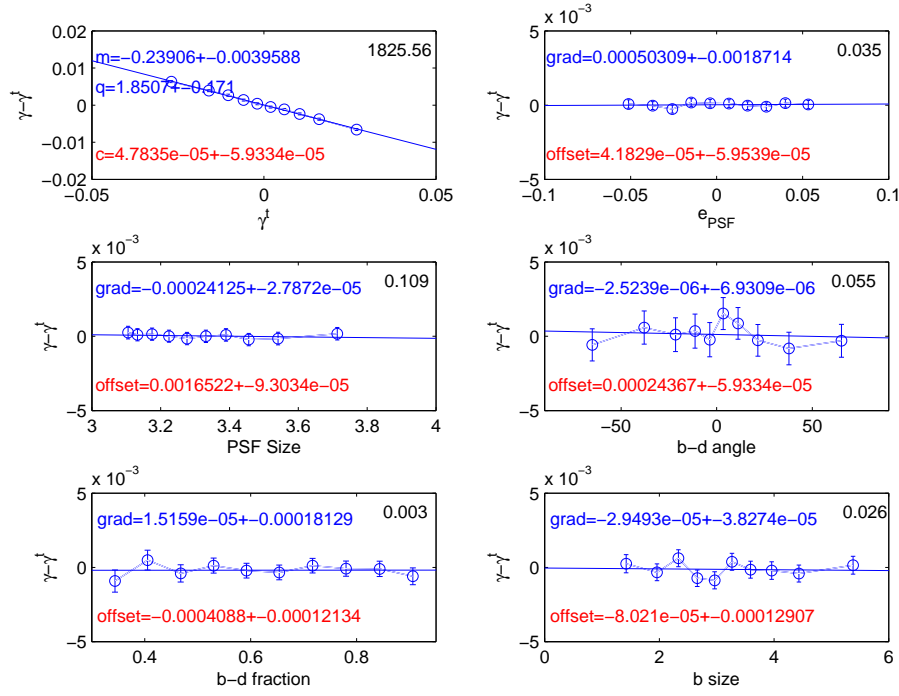


**Figure 46.** The measured minus true shear for the ‘NN23’ submission as a function of the true shear, PSF ellipticity, PSF FWHM, galaxy bulge-to-disk offset angle, galaxy bulge-to-disk fraction and galaxy bulge size. For each dependency we fit a linear function with a gradient and offset, for the top left hand panel this is the STEP  $m$  and  $c$  values, additionally for the shear dependency we include a quadratic term separately  $q$ . The top right hand corners show  $\Delta\chi^2 = \chi^2(\text{gradient}, \text{offset}) - \chi^2(\text{offset})$ .

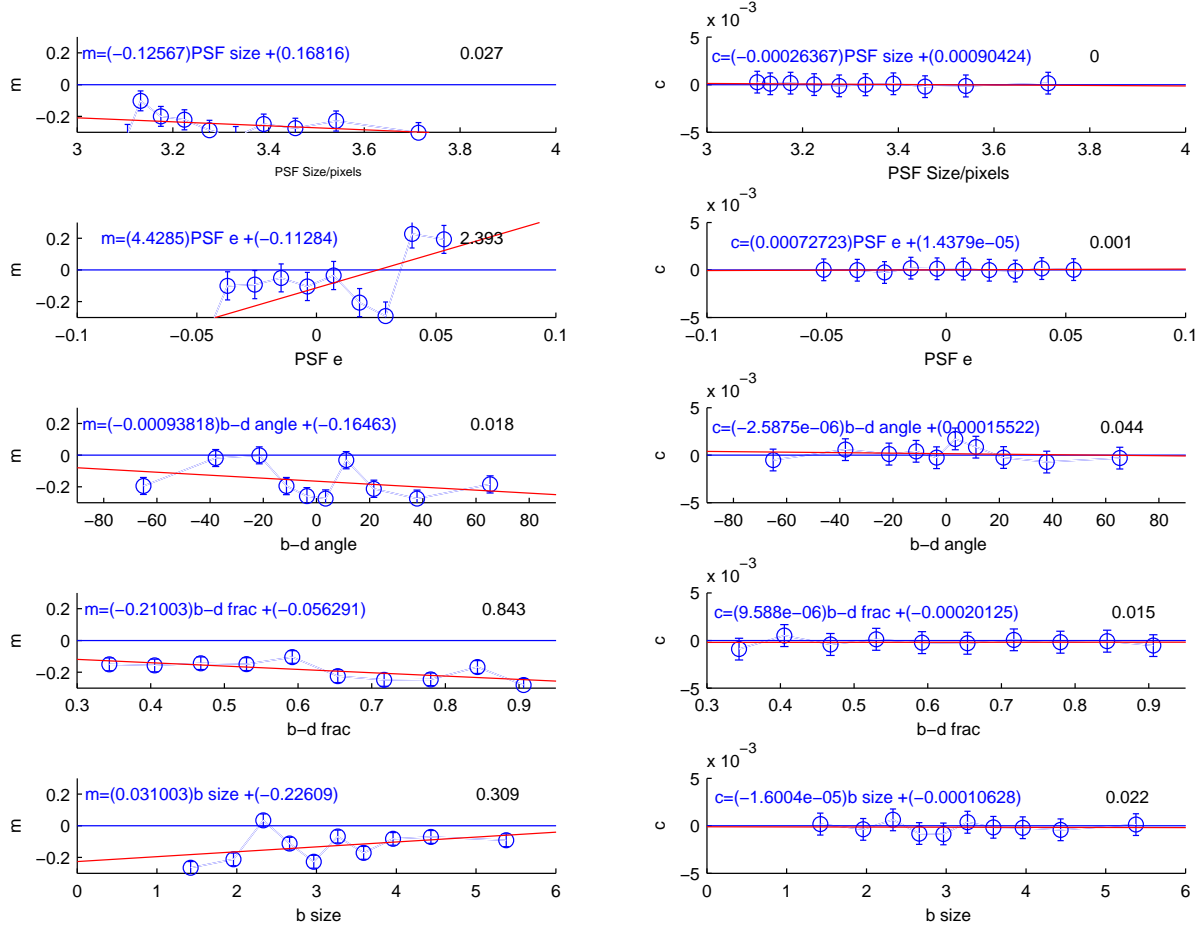


**Figure 47.** The STEP  $m$  and  $c$  values for the ‘NN23’ submission as a function of PSF FWHM and ellipticity, galaxy bulge-to-disk offset angle, galaxy bulge-to-disk fraction and galaxy bulge size. For each variable we plot the a linear relation to the behaviour of  $m$  and  $c$ . We do not explicitly quote errors on all parameters for clarity, the average errors on  $m$  and  $c$  are  $\simeq 0.005$  and  $5 \times 10^{-5}$  respectively. The top right hand corners show  $\Delta\chi^2 = \chi^2(\text{gradient}, \text{offset}) - \chi^2(\text{offset})$ .

**APPENDIX F: SIMULATIONS**

Inevitably, with a simulation the size of the GREAT10 Galaxy Challenge, there were several points in which the data or interpretation of the data/competition instructions were inadvertently misinterpreted by participants. We list these here:

- (i) Approximately 1% of the data were found to contain image glitches and were replaced during the challenge as a patch to the data.
- (ii) The functional PSFs used a convention in  $(x, y)$  coordinate and ellipticity for which some methods had to make the following transformations  $e_2 \rightarrow -e_2$ ,  $x \rightarrow y$  and  $y \rightarrow x$ ,  $r_{\text{PSF}} \rightarrow r_{\text{PSF}}/(1 + e_1^2 + e_2^2)$ . This convention warning was listed in the header of every functional PSF description during the challenge.
- (iii) An additional two sets contained “pseudo-Airy” PSFs using the functional form of Kuijken (2006). However there was a misinterpretation by some participants between the functional PSF description and the PSF FITS images generated using the photon-shooting method used in the GREAT10 code. This arose because in the photon-shooting method photons at large  $r$  are generated using a uniform distribution from 0 to 1 and then their values replaced by a reciprocal; but the PDF of such a process yields a variation of  $1/r^2$  not  $1/r$ , that when modulated by the function gives  $1/r^4$  (not  $1/r^3$ , given in equation 21, Kuijken, 2006; the same equation that was provided to participants). This was identified during the challenge and all participants were informed, and the code used to produce the PSFs made public<sup>8</sup> on 7<sup>th</sup> February 2011 (7 months before the challenge deadline), however we have not included the results from these sets in this paper because several submissions were affected.

Each of these issues were addressed during the challenge, however the nature of the participation rate (see Section 5, all submissions were made in the final 3 weeks) meant that some methods did not have time to create alternative submissions before the official challenge closed. The challenge was extended by one week, into a post-challenge submission period, but those methods submitted during this time could not officially ‘win’ the competition, in the event none of these additional submissions improved on the winning score

When using the GREAT08/GREAT10 code we note a number of issues that should be taken into account in its description in Bridle et al., (2010). The signal to noise used in Bridle et al., (2010) is approximately half the standard definition used in this article. Equation (A8) makes the area of the galaxy invariant under the primary ellipticity transformation (but not under the cosmological shear transformation), whereas equation (A9) does not make the PSF area invariant under the ellipticity transformation. Also the sense of the transformation in these equations of  $g$  for galaxies and  $e$  for PSFs is different; the PSF shear is in the opposite direction to the cosmic shear. Finally, we also note that there were two typos in Appendix A of Bridle et al., (2010). These were 1) in equation (A5) the left top corner of the matrix should be  $r/\sqrt{q}$  and 2) equation (A8) should be the transpose of which it reads.

<sup>8</sup> <http://great.roe.ac.uk/data/code/sm/>